INFRARED SENSING SYSTEMS USING CARBON NANOTUBE BASED PHOTODETECTORS

By

Hongzhi Chen

A DISSERTATION

Submitted to Michigan State University in partial fulfillment of the requirements for the degree of

DOCTOR OF PHILOSOPHY

Electrical Engineering

2012

ABSTRACT

INFRARED SENSING SYSTEMS USING CARBON NANOTUBE BASED PHOTODETECTORS

$\mathbf{B}\mathbf{y}$

Hongzhi Chen

Infrared (IR) sensing systems have versatile applications; however, low performance and high cost of the conventional photodetectors have prevented their widespread utilization in various fields. Carbon nanotube (CNT), a promising nano-material with excellent electrical and optical properties, has potential to develop high performance IR detectors compared to their conventional counterparts. However, there are three major difficulties that impede the application of CNT based photodetectors for imaging systems. Firstly, there are challenges in design, fabrication, and testing of CNT photodetectors because of their nano-scale size and unique geometry. Secondly, the small diameter of the CNTs results in low fill-factor (absorption area). Thirdly, it is difficult to fabricate large scale of photodetector array for high resolution focal plane due to the limitations on the efficiency and cost of the manufacturing. The issues related to the design and fabrication of CNT based photodetectors were addressed by configuring the device in field effect transistors with different metal and gate structures. In addition, the theoretical foundations as well as the implementation schemes for the development of nano-structure lens to improve absorption efficiency of IR detectors were developed. The topics include the optical antennas that confine light into a sub-wavelength volume, as well as photonic crystals to increase the effective absorption area. Furthermore, a novel CNT based IR sensing system was developed. The experimental results showed that the new IR sensing system can achieve the superb performance enabled by CNT based photodetectors, and, at same time, to obtain high resolution and efficient imaging.

To my parents, my wife Chenyi Wang, and to my son, for their love and support

ACKNOWLEDGMENTS

I would like to express my most sincere appreciation to my advisor, Dr. Ning Xi, for his expert guidance, generous encouragement and support for my research.

In addition, I would like to thank all my PhD committees: Dr. Timothy Grotjohn, Dr. Fathi Salem, Dr. Tim Hogan, Dr. Stuart Tessmer. They offered me timely help and unfailing support that improve the technical soundness and the presentation of this dissertation.

Furthermore, I would like to express my gratitude to all my colleagues, especially to Dr. Jiangbo Zhang, Dr. King Wai Chiu Lai, Bo Song, Liangliang Chen, Ruiguo Yang, Jianguo Zhao, and Yunyi Jia, for their support in the experiments and discussion.

Last but not the least, I want to thank my parents and my wife, Chenyi Wang. They have always been my cheerleaders and supporters. This dissertation would not have been possible without their years of encouragement and continuous support. With love and gratitude, I dedicate this dissertation to them.

TABLE OF CONTENTS

List of	Tables vii
List of	Figures viii
Chapte	${ m er} { m 1} { m Introduction} $
1.1	Overview
1.2	Background and Literature Review
	1.2.1 Blackbody Radiation
	1.2.2 Infrared Detectors
	1.2.3 Image Acquisition in Scanning and Staring Configuration
	1.2.4 Advantages of One Dimensional Semiconductors as Sensing Element . 9
	1.2.4.1 Reduced Light Reflection and Transmission 10
	1.2.4.2 Bandgap Engineering
	1.2.4.3 Multiple Electron and Hole Pairs Generation
	1.2.4.4 Reduced Scattering
	1.2.4.5 Higher Defect Tolerance
	1.2.5 Carbon Nanotube Based Photodetectors
1.3	Objectives and Challenges
1.4	Organization of the Study
Chapte	er 2 Carbon Nanotube Schottky Photodiodes
2.1	Design of the CNT Schottky Photodiode
2.2	Symmetric Schottky Photodiodes
$\frac{2.2}{2.3}$	Asymmetric Schottky Photodiodes
2.4	Chapter Summary
Chapte	er 3 Carbon Nanotube Field Effect Transistor based Photodetectors 42
3.1	Back-gate Au-CNT-Au Transistor
$\frac{3.1}{3.2}$	Back-gate Ag-CNT-Ag Transistor
$\frac{3.2}{3.3}$	Back-Gate Au-CNT-Ag Transistor
3.3	Middle-Gate Transistor
$\frac{3.4}{3.5}$	Multi-Gate Transistor
3.6	
3.0	v e
3.7	Chapter Summary
Chapte	er 4 Spectral Responses of CNT Photodetectors
4.1	Spectral Response of SWCNT based Photodetectors

4.2	Electrical Breakdown Control	88
4.3	Spectral Response of MWCNT based Photodetectors	92
4.4	Chapter Summary	95
Chapte	er 5 Plasmonic Lens using Optical Antenna	97
5.1	Introduction of Optical Antenna	97
5.2	Design of Bowtie Antennas	101
	5.2.1 Insulator Thickness Dependent E-field Enhancement	102
	5.2.2 Tip Angle Dependent E-field Enhancement Spectra	106
5.3	Fabrication and Experimental Results	109
	5.3.1 Fabrication Process	109
	5.3.2 Experimental Results	111
5.4	Chapter Summary	116
Chapte	er 6 Photonic Crystal Cavity	117
6.1	Introduction of Photonic Crystal Cavity	117
6.2	Design and Fabrication	119
6.3	Experimental Results	121
6.4	Chapter Summary	127
Chapte	er 7 Infrared Sensing Systems Using a Single Nano-photodetector	128
7.1	Compressive Sensing Theory	129
7.2	Sensing System Architecture	133
7.3	Experimental Results	137
	7.3.1 Dynamic Observation	140
	7.3.2 Zooming	142
7.4	Chapter Summary	143
Chapte	er 8 Conclusions and Future Work	146
8.1	Conclusion	146
8.2	Future Research	148
Riblio	vranhv	151

LIST OF TABLES

Table 1.1	Performance Comparison of Photon and Thermal Detectors	7
Table 2.1	Performance of Four Detectors with Different Metals	35
Table 4.1	Dark Current and Noise at Different Gate Voltages	84

LIST OF FIGURES

Figure 1.1	Energy distribution of a blackbody at three temperatures. The dot line indicates the Wien's law. (For interpretation of the references to color in this and all other figures, the reader is referred to the electronic version of this dissertation.)	4
Figure 1.2	The classification of IR detectors	6
Figure 1.3	Staring configuration with a 2D focal plane array	8
Figure 1.4	(a) Raster scanning system. (b) Parallel scanning system	9
Figure 1.5	Two-diameter Ge nanowire array for maximized absorption. (a) The structure of the two-diameter nanowire array (called double nanopillar (DNPL)). (b) Average absorption efficiency over λ =300-900 nm for single-diameter nanowire arrays as a function of diameter along with that of the double-diameter nanowire array. [3]	11
Figure 1.6	The structure of a CNT thin film photodetector	15
Figure 1.7	The structure of a silicon-CNT heterojunction photodetector with nanoporous anodic aluminum oxide (AAO) template to separate the vertical CNT array	17
Figure 1.8	The structure of a single CNT based p-n junction photodiode	18
Figure 1.9	The structure of a single-CNT-based Schottky photodiode	20
Figure 2.1	(a) Energy alignment of Au and CNT. (b) Band diagram of a symmetric CNT photodetector	25
Figure 2.2	(a) Energy alignment of metals with high/low workfunctions and CNT. (b) Band diagram of the asymmetric CNT photodetector	27
Figure 2.3	An AFM image of a symmetric CNT detector with Au electrodes	28

Figure 2.4	(a)I-V characteristics of CNT Schottky diodes with four different metals (Pd, Au, Cu and Al). (b)The I-V characteristics shown in logarithm scale	30
Figure 2.5	I-V characteristics of a Au-CNT-Au diode at different temperatures.	31
Figure 2.6	The IR responses of a Au-CNT-Au Schottky photodiode by radiating on (a) left electrode, (b) right electrode	32
Figure 2.7	The IR responses of two CNT Schottky photodiodes with metal structures of (a) Pd-CNT-Pd, (b) Au-CNT-Au	33
Figure 2.8	The IR responses of two CNT Schottky photodiodes with metal structures of (a) Cu-CNT-Cu, (b) Al-CNT-Al	34
Figure 2.9	The IR responses of CNT Schottky photodiodes with bias (a) Cu-CNT-Cu, (b) Au-CNT-Au	37
Figure 2.10	(a-c) Fabrication process of the Au-CNT-Au and Al-CNT-Au photodiodes using a single CNT. (d) Their I-V characteristics	39
Figure 2.11	Photo-response of the Au-CNT-Au and Al-CNT-Au photodiodes using a single CNT	40
Figure 3.1	An AFM image of the structure of CNTFET with a silicon back-gate.	45
Figure 3.2	Structure of the back-gate Au-CNT-Au CNTFET	47
Figure 3.3	(a) The I-V characteristics of the CNTFET. (b) Transfer characteristics of the CNTFET at Vds=50 mV	48
Figure 3.4	(a) Transfer characteristics of the Au-CNT-Au CNTFET with IR source off (IR=0) and on (IR=50mW) at zero bias. (b) The relationship between gate voltage and photocurrent and corresponding band diagrams at negative and positive gate voltages	49
Figure 3.5	The energy levels of Au and CNT	50
Figure 3.6	The bias-dependent measurement of the Au-CNT-Au CNTFET with IR=0 and IR=50 mW at (a) Vg=-0.5V and (b)Vg=2V	52
Figure 3.7	The energy levels of Ag and CNT	53

Figure 3.8	(a) I-V characteristics of the CNTFET. (b) Transfer characteristics of the CNTFET at Vds=50 mV	54
Figure 3.9	(a) The relation between gate voltage and photocurrent of the Ag-CNT-Ag CNTFET. (b) Bias dependent measurement with IR at four different output powers at Vg=3 V	56
Figure 3.10	Structure of the back-gate Au-CNT-Ag CNTFET	57
Figure 3.11	(a) Transfer characteristic of the asymmetric CNTFET with and without IR illumination. (b) Temporal photo-response with three different gate voltages at IR=50 mW	58
Figure 3.12	Bias dependent measurement with IR at four different output powers at Vg=5 V	59
Figure 3.13	(a) Structure of the middle-gate CNTFET. (b) AFM image of the middle-gate CNTFET. (c) Band diagram of the working status of the middle-gate CNTFET	61
Figure 3.14	(a) I-V characteristics of the middle-gate CNTFET at three Vg in log-scale. (b) Transfer characteristics of the CNTFET with Vds=10 mV	62
Figure 3.15	(a) Transfer characteristics of the middle-gate CNTFET with IR on and Off at zero bias. (b) Temporal photo-response measurement by switching IR on and off at 0.2 HZ	64
Figure 3.16	Bias dependent measurement with IR at two output powers at Vg=2 V	65
Figure 3.17	AFM image of the multi-gate asymmetric CNTFET with a back-gate and three pairs of side-gates that can locally modulate source (Gate1), SWCNT channel (Gate2), and drain (Gate3)	67
Figure 3.18	The I-V characteristics of the CNTFET with symmetric (Au-CNT-Au) and asymmetric (Al-CNT-Au) metal structures. The insets shows the cross-section of the CNTFET	69

Figure 3.19	Transfer characteristics versus the back-gate bias at zero bias of the symmetric CNTFET with absence and presence of IR laser illumination (wavelength of 830 nm and output power of 50 mW) by sweeping the gate bias from -3 V to 3V. Two band diagrams show the Schottky barriers at negative and positive gate biases	71
Figure 3.20	Transfer characteristics at zero bias of the asymmetric CNTFETs with absence and presence of IR illumination. The inset shows the transfer characteristics in logarithm scale. The band diagram shows the energy alignment of the device.	72
Figure 3.21	Photocurrent transfer characteristics of the asymmetric CNTFET at zero drain to source bias. The band diagrams show the barrier width (w) at negative and positive gate biases	73
Figure 3.22	Temporal photocurrent measurement of the asymmetric CNTFET with three different gate biases (-3V, -1V, and 0V) by switching IR OFF and ON at 0.2 Hz	74
Figure 3.23	(a) Photocurrent transfer characteristics by applying gate biases to back-gate (Vgs), source (Vg1), SWCNT channel (Vg2), and drain (Vg3). (b)A 3D geometry of the multi-gate CNTFET and the charge distribution of the SWCNT, showing the charge tail on the SWCNT.	77
Figure 3.24	Asymmetric CNTFET with a simplified gate structure	78
Figure 3.25	The image of a 3x3 detector array and the AFM image of the Pixel9.	79
Figure 3.26	The images obtained from the detector array, and color lightness shows the magnitude of photocurrent. The laser spot center is on (a)Pixel5, (b)Pixel1	80
Figure 4.1	The blackbody testing system	83
Figure 4.2	(a) The I-V characteristics of the transistor with Vg from -3V to 3V.(b) The relationship between Vg and current, showing conductivity decreases with increasing positive gate voltages.(c) The temporal dark current measurement with three different gate voltages.	85
Figure 4.3	The temporal IR response by radiating blackbody source to the detector at 0.5 Hz with (a) Vg=0 V, (b) 1 V, (c) 2 V and (d) 3 V	86

Figure 4.4	The spectral response of the SWCNT based photodetector	87
Figure 4.5	Breakdown (BD) control curve	90
Figure 4.6	The I-V characteristics of the device before and after BD	91
Figure 4.7	(a) Illustration showing a single MWCNT connected to three gold microelectrodes. The I-V characteristics of the MWCNT at different segments: (b) Segment AB, (c) segment BC, and (d) segment AC.	
Figure 4.8	The I-V characteristics of a MWCNT photodetector before and after consecutive breakdowns (BD)	94
Figure 4.9	The spectral response of the MWCNT based photodetector	96
Figure 5.1	(a) A 3D geometry shows the relative position between the CNT based photodetector and the bowtie antenna. The incident light with electric field polarized in the x direction propagates in the z direction. (b) Top view of the device, and parameters of the bowtie antenna: L=400 nm is the length of the antenna, g=30 nm is the gap of two pieces of the antenna, w=30 nm is the apex width, and is the tip angle. (c) Side view of the device, showing the CNT based photodetector and bowtie antenna sandwiching the Si_3N_4 layer that has a thickness of t	103
Figure 5.2	(a) The E-field distribution of the resonance frequency (845 nm) of the bowtie antenna with θ =60 degrees, and t=10 nm. The x-y axis show the coordinate for simulation. (b) The t dependent peak field intensity Max($\mid E\mid^2$), blue curve is the simulation values, and red curve is the exponential fit. The inset shows field intensity enhancement $\mid E\mid^2$ at wavelength of 830 nm	105
Figure 5.3	E-field intensity enhancement $ E ^2$ spectra of bowtie antennas with tip angles ranging from 0 degrees to 120 degrees. The inset shows a scanning electron microscopy (SEM) image of a bowtie antenna, denoting the tip angle θ	107
Figure 5.4	(a-e) Fabrication process of integrating a bowtie antenna to a CNT based photodetector. The inset of (c) is an AFM image of a SWCNT bridging a Ti and an Au electrode. (f) A 3D AFM image of the device	.112
Figure 5.5	Photo-responses of the CNT based photodetector without and with bowtie antenna by switching IR laser on and off at 0.2 Hz	113

Figure 5.6	I-V characteristics of the CNT photodetector without and with the bowtie antenna	
Figure 6.1	(a) AFM image of a parylene photonic crystal with a HfO ₂ defect on the top of a CNT detector. (b) Cross section of the device. (c) The working principle of the photonic cyrstal cavity by confining the light radiating on photonic crystal into the defect	120
Figure 6.2	(a) The simulation geometry of the photonic cavity with parylene slab and a HfO_2 defect. (b) Electric field distribution of a 1064 nm IR light in the photonic cavity, most of the electric field is confined within the point defect	122
Figure 6.3	Fabrication process of the testing device (a) CNT Schottky photodiode, (b) CNT photodetector with a HfO_2 defect,(c) Photodetector with photonic crystal and a HfO_2 defect	123
Figure 6.4	Experimental setup to obtain scanning photocurrent images	125
Figure 6.5	Scanning photocurrent images of the CNT photodetectors without and with photonic crystal cavity. The insets are the AFM images of detectors without and with photonic crystal cavity.	126
Figure 7.1	(a) Scanning electron microcopy (SEM) image of an array of micromirros in the DMD. (b) Three status of the micro-mirrors: "on", "off", and power-off states	134
Figure 7.2	The setup of compressive sensing based imaging system using a CNT detector with photonic cavity and DMD	136
Figure 7.3	(a) The position and orientation of the rectangular light bar on the DMD. (b) The image of 50×50 pixels recovered by our imaging system, highlighted by a red rectangle	139
Figure 7.4	Six images of a laser spot captured by our imaging system, showing the movement of the spot.(a) The infrared image shows the initial position of the laser spot. (b)-(e) The laser spot moved downwards towards the bottom of the image. (f) The laser spot moved upwards after it approached the bottom of the DMD	141
Figure 7.5	$\times 1$, $\times 2$, $\times 8$, $\times 12$ magnification IR images captured by our imaging system, and their corresponding sections of DMD used to capture the images were highlighted by blue rectangles	144

Chapter 1

Introduction

1.1 Overview

Infrared (IR) sensing systems, including IR cameras and IR detection systems, were widely employed in various areas, including military, manufacturing quality control, medical diagnosis, weather forecasting, environmental monitoring, and so on. The core component of IR sensing systems is the photodetector, which detects heat distribution, rather than visible light, according to the blackbody radiation theory. IR spectrum, especially middle-wave IR (MWIR), is of particular importance, since electromagnetic emission from humans and the atmosphere are within this spectrum.

The photodetectors mainly determine the performance of IR cameras. There are two categories of traditional photodetectors, including thermal detectors and photon detectors. Both detectors have their own limitations: thermal detectors have slow response and low detectivity; while photon detectors have narrow and selective spectral detection, and need to operate at cryogenic temperature. Therefore, an IR sensing system with fast response, low detectivity, multi-spectral detection, and room temperature operating is demanding.

With the development of nano-technologies, one-dimensional (1D) materials, including nanowires and nanotubes, emerged as important components in photonics and optoelectronics. Compared to traditional semiconductors, 1D materials possess a number of unique properties arose from their geometries, making them potential candidates to outperform

traditional photodetectors. In particular, carbon nanotubes (CNTs) are of great interest for exploring as functional elements for 1D photodetectors due to their perfect nano-hollow cylinder structure. Assembling a CNT thin film has been demonstrated, but the interaction between CNTs in thin film resulted in the loss of their unique optical properties. Therefore, one single CNT is more favorable to fabricate high performance photodetectors.

However, there is no reliable manufacturing technique to fabricate large scale CNT based photodetectors, preventing the integration of CNT photodetectors into traditional sensing systems, particularly the focal plane array imaging system. An alternative sensing platform is required to utilize small number or even a single CNT photodetector. Aiming to taking advantages of the outstanding optoelectronic properties of CNTs, we developed an IR sensing system that integrated a CNT photodetector into a novel camera structure that can use a few or even a single photodetector. The sensing system can achieve the superb performance enabled by CNT based IR detectors, and, at same time, to obtain high resolution and efficient imaging.

1.2 Background and Literature Review

1.2.1 Blackbody Radiation

All matter emits electromagnetic (EM) waves at temperature above absolute zero (0 K). This is known as thermal radiation. Thermal radiation is also called IR radiation, which covers a wide EM spectrum ranged from 0.77 μm to 1000 μm .

Blackbody is an idealized entity that absorbs all radiation falling on it, but reflects none. Blackbody radiation is the emission of a blackbody at unity efficiency. Therefore, blackbody emission has a temperature-dependent characteristic frequency distribution when it is at a uniform temperature. Blackbody radiation provides a convenient theoretical model to predict emitting properties of objects.

The Planck's law describes blackbody's energy distribution of different wavelengths at a given temperature:

$$W_{\lambda} = \frac{2\pi hc^2}{\lambda^5 (e^{\frac{hc}{\lambda kT}} - 1)} \tag{1.1}$$

h is the Planck constant, c is the speed of light, λ is the wavelength, k is the Boltzmann constant, and T is the absolute temperature of the blackbody.

The Wien's displacement law predicts the wavelength (λ_{max}) that delivers the highest intensity of radiation at a given temperature:

$$\lambda_{max} = \frac{b}{T} \tag{1.2}$$

b is the Wien's displacement constant with a value of 2.898×10^{-3} m·K. The λ_{max} decreases with increasing temperature.

The Stefan's law estimates the total energy radiated in an given area per unit time at a certain temperature:

$$W = \sigma A T^4 \tag{1.3}$$

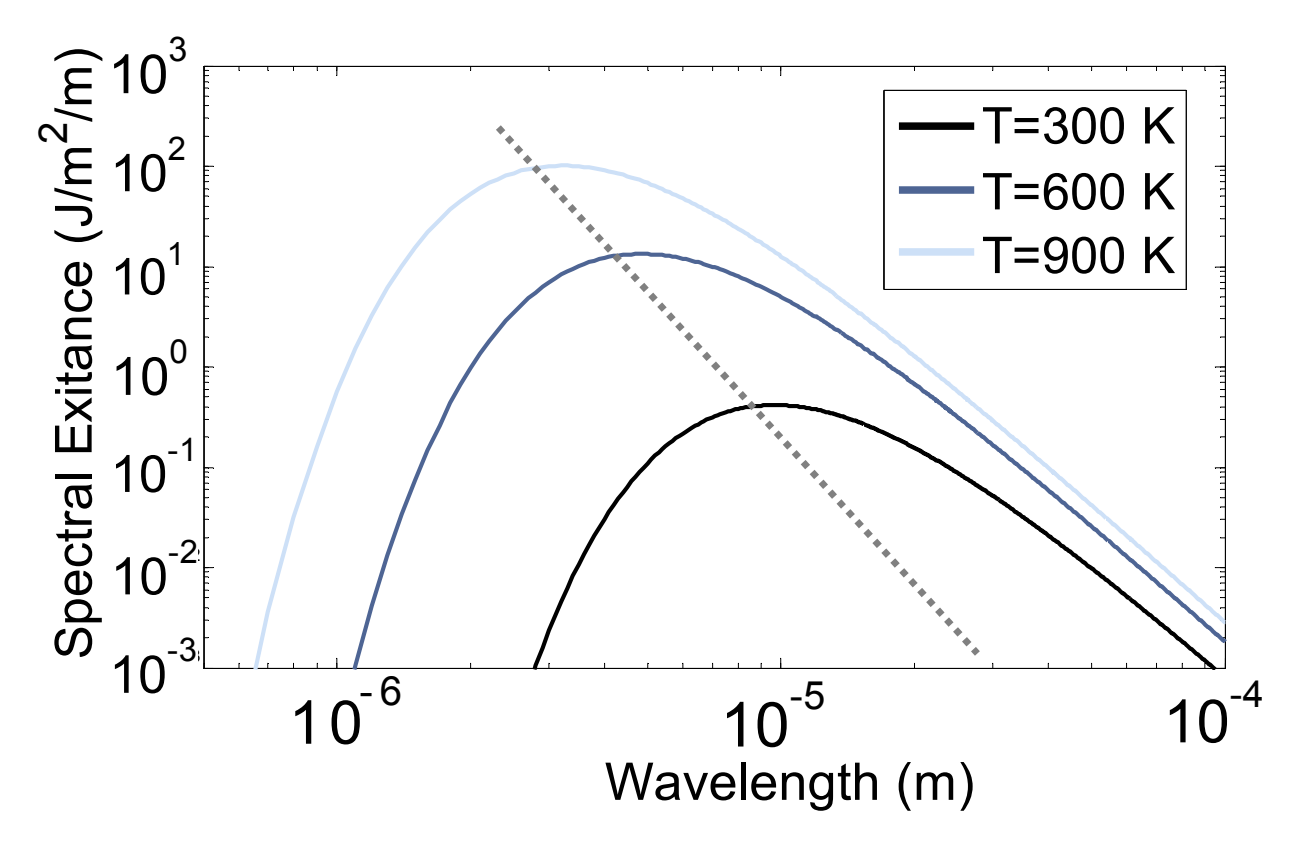


Figure 1.1: Energy distribution of a blackbody at three temperatures. The dot line indicates the Wien's law. (For interpretation of the references to color in this and all other figures, the reader is referred to the electronic version of this dissertation.)

 σ is the Stefan's constant with a value of $5.67 \times 10^{-3} \ Jm^{-2}K^{-4}$, A is the surface area of the body. Total radiation energy is proportional to T^4 , thus a minor increase of blackbody temperature will involve a relative major change of the total energy.

Figure 1.1 shows the blackbody radiation at three temperatures according to the Planck's law. The dot line reflects the Wien's law. The peak radiation wavelength at 300 K is at 10 μm , which cannot be seen by human eyes. The peak radiation wavelength blueshift with increasing temperature, gradually approaching visible light. The radiation of a real object can be calculated according to these three laws, adjusted by the emissivity ε . ε is the ratio of energy radiated by a real object to that of the blackbody radiation.

1.2.2 Infrared Detectors

The core component of the IR sensing systems is the IR detector. IR detectors are photodetectors that convert electromagnetic signals within IR spectrum into other forms of signals (current or voltage) for detection and quantification.

The IR detectors can be mainly categorized into two classes: thermal detectors and photon detectors. Photon detectors generate electrical outputs through the direct interaction between photons and electrons, photo-exciting bound electrons of semiconductors from valence band to conduction band. Thermal detectors change the temperature of photosensitive materials by absorbing incident radiation, resulting in some physical properties change that converts into electrical outputs.

Depending on the working principles, photon and thermal detectors can be sub-divided into different types, as shown in Figure 1.2. Three main types of photon detectors are photovoltaic, photoconductive, and photoemissive detectors. Photovoltaic detectors utilize their internal built-in potential to separate photo-excited electron and hole pairs in order to generate current or voltage for detection, for example the p-n junction. Photoconductive detectors detect the change of conductivity caused by the increase of photo-excited electrical carriers, and external bias are required to operate. Photoemissive detectors collect electrons escaped from a photosensitive surface, which absorbs IR radiation and delivers enough kinetic energy for electron escaping.

Three main types of thermal detectors are thermistors, pyroelectric detectors, and thermovoltaic detectors. Thermistors sense the conductivity change of the functional element due to the change of temperature upon the absorption of IR photons, and bolometer is one of thermistors. Pyroelectric detectors measure the electric field generated by the temperature-

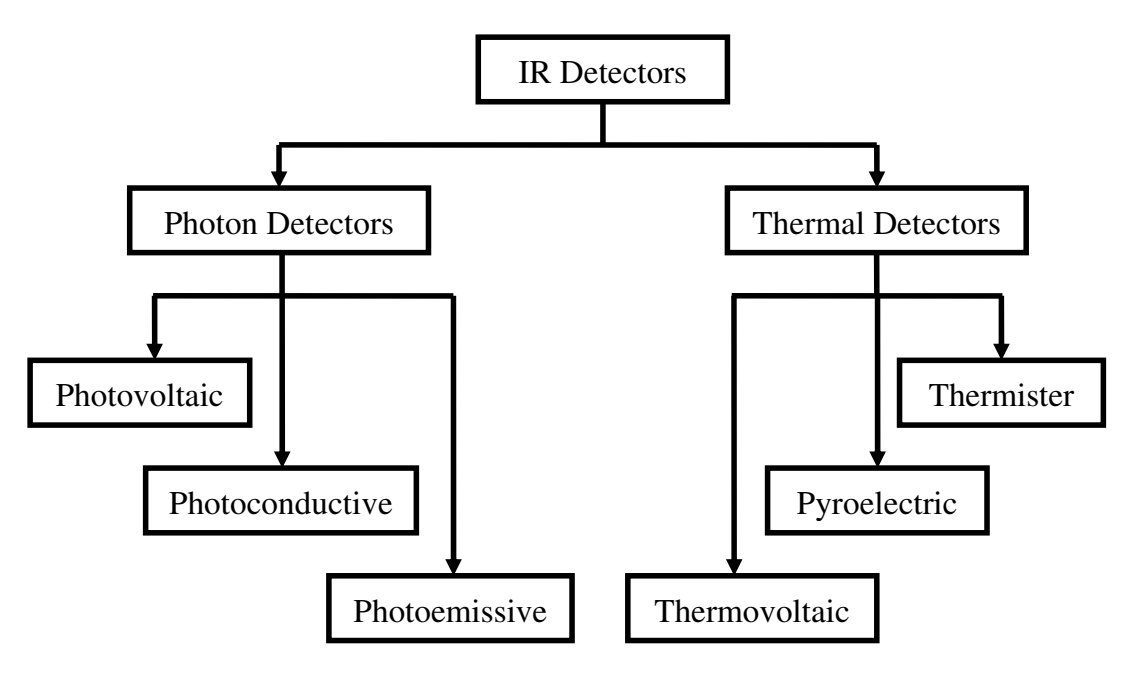


Figure 1.2: The classification of IR detectors.

dependent dipole moment change of the responsive elements. Thermovoltaic detectors are also called thermocouples or thermopiles. Upon IR illumination, the temperature change of the junction of two dissimilar metal produces a voltage for detection due to the difference of Seebeck coefficients of two metals.

Table 1.1 compares the performance of photon and thermal detectors. Thermal detectors require heating the detection element in order to detect IR signals, therefore they have an inherently slow response and relatively low detectivity compared to photon detectors. However, thermal detectors can be operated at room temperature and have a wide spectral response, while photon detectors have narrow and selective spectral response depending on their bandgap energies and most of them need to be operated in cryogenic temperature. As a result, the manufacturing of photon detectors are more expensive than thermal detectors.

Our research will focus on developing an IR sensing system using CNT based photon detectors, because photon detectors using nano-materials may address the problems of the

Table 1.1: Performance Comparison of Photon and Thermal Detectors

	Photon Detectors	Thermal Detectors
Speed	Fast	Slow
Operation Temperature	Cryogenic Cooled	Room Temperature
Detectivity	High	Low
Spectral Response	Narrow	Wide
Cost	Expensive	Economical

narrow spectral response and requirement of cryogenic cooling.

1.2.3 Image Acquisition in Scanning and Staring Configuration

In IR sensing systems, in particular IR cameras, the photodetectors must be distributed over the focal plane (image plane) in order to capture the spatial IR images. The photodetector distribution across the entire image can be accomplished by systems in scanning or staring configurations [1]. Scanning configuration scans the image across a single photodetector or a linear detector array. Staring configuration has a two-dimensional (2D) photodetector array distributing in the focal plane (focal plane array), as shown in Figure 1.3.

Scanning configuration can be sub-divided into raster and parallel scanning systems. In the raster scanning system, a scanner moves the scene over a single or a few fixed photodetectors in the focal plane, as shown in Figure 1.4(a). The photodetectors are aligned horizontally and scanned sequentially in a 2D raster pattern to form an image. The parallel scan system comprises a linear photodetector array that is perpendicular to the scanning direction, as shown in Figure 1.4(b). It should be noted that the linear photodetector array can have more than one columns of photodetectors. Figure 1.4(b) only shows one column of photodetectors for making the schematic clearer. The scanner horizontally scans one line

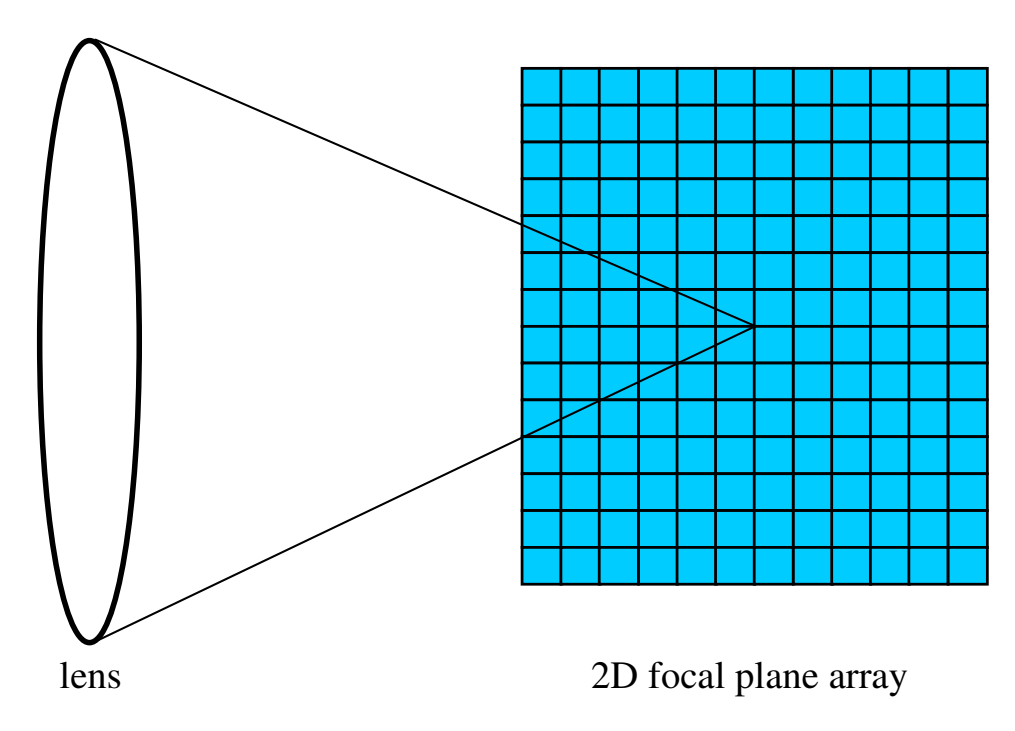


Figure 1.3: Staring configuration with a 2D focal plane array.

across the linear array, and then a slight tilt of the scanner in the vertical direction is applied and the image is scanned across the photodetector array in the opposite direction to cover the image plane in order to obtain a complete image. There are a wide variety of scanners to implement the scanning, and a mechanical mirror is the most efficient and well developed one.

Imaging systems with the staring configuration can result in enhanced performance and lighter system. The scanning system can be used in applications where large array of photodetectors are very expensive or difficult to manufacture.

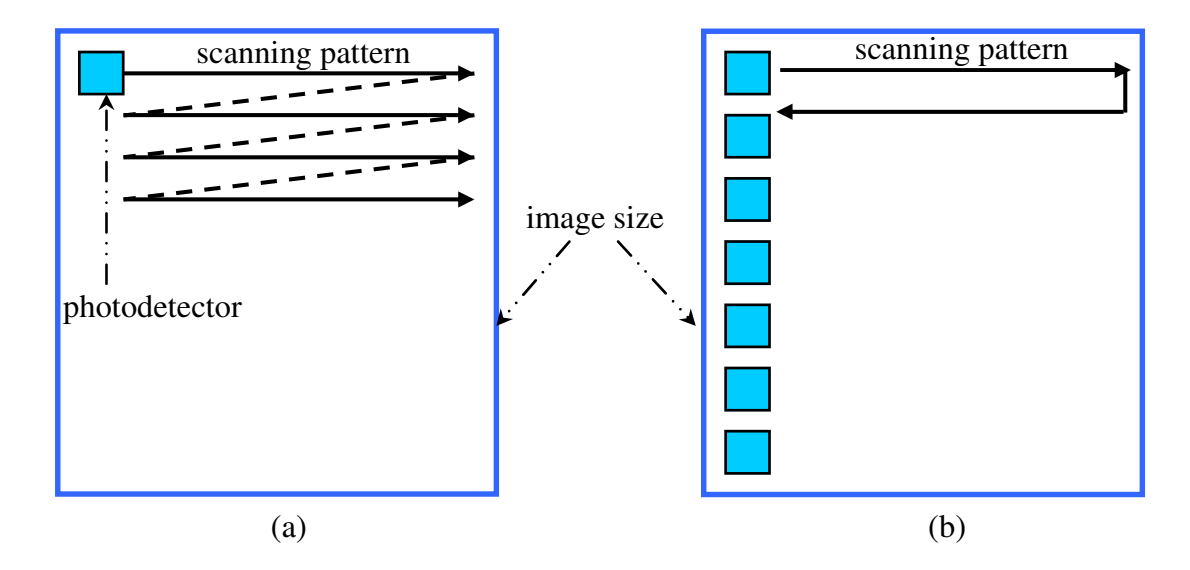


Figure 1.4: (a) Raster scanning system. (b) Parallel scanning system.

1.2.4 Advantages of One Dimensional Semiconductors as Sensing Element

Nanowires and nanotubes are 1D materials, since electrons in these nano-size cylinders was freely to move in axial direction, while electrons are quantum confined in radial directions when their diameters are smaller than Bohr radii. 1D semiconductors were proposed to be the functional element of high performance photodetectors and solar cells, since they have some unique properties stemming from their geometry and quantum confinement [2].

It should be noted that our goal is developing an IR sensing system with high performance photon detectors. In photon detectors, there are many sources of losses in the process of converting IR signals into electrical signals: (1) photons are reflected and transmitted instead of being absorbed; (2) photons with energy that is lower and higher than bandgap energy causes some energy losses; (3) photo-excited electron and hole pairs recombine; (4) the electrical carriers were scattered during transportation. These losses can be reduced by using 1D semiconductors as the sensing element. The potential efficiency benefits mainly come from

higher efficiency in photon absorption and trapping; improvement in photo-generated carrier separation, transportation and collection; lowering the purity standard needed to obtain high efficiencies; enhancing the defect tolerance.

1.2.4.1 Reduced Light Reflection and Transmission

It was reported that both light transmission and reflection were reduced by using Ge nanowires compared to Ge thin film. As a result, the absorption was highly improved [3]. A double diameter platform was designed to optimize absorption, with small diameter tip and large diameter base, as shown in Figure 1.5(a). Small diameter tips were used to minimize reflectance, while large diameter bases were utilized to suppress transmittance.

The broad band absorption enhancement for the double-diameter nanowire array (double nanopillar (DNPL)) is depicted in Figure 1.5(b). For single-diameter nanowire array, a strong diameter dependency is observed, with a peak absorption 94% when diameter =80 nm. Double-diameter nanowire array with D1= 60 nm and D2=130 nm exhibits absorption of 99%, clearly demonstrating the advantage of this novel structure. Notably, both single-diameter and double-diameter nanowire array drastically outperform a 2 μ m-thick planar Ge thin film (TF) absorption 53%.

1.2.4.2 Bandgap Engineering

When the diameter of a 1D semiconductor is smaller than its Bohr radii, bandgap energy is inversely proportional to its diameter due to the quantum confinement. In other words, the band gap energy of 1D materials can be modulated by controlling their diameters rather than using different semiconductors.

When an electron approaches a hole, they may form a Wannier exciton, approximately

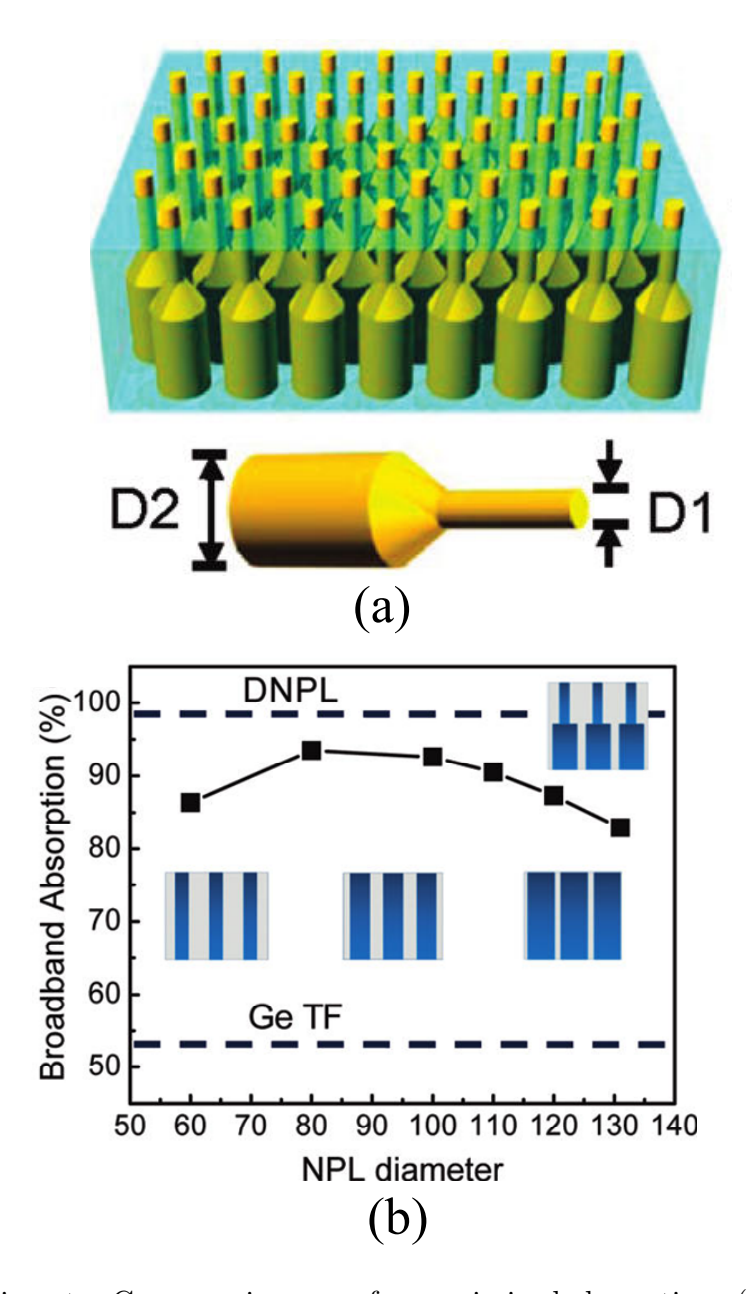


Figure 1.5: Two-diameter Ge nanowire array for maximized absorption. (a) The structure of the two-diameter nanowire array (called double nanopillar (DNPL)). (b) Average absorption efficiency over λ =300-900 nm for single-diameter nanowire arrays as a function of diameter along with that of the double-diameter nanowire array. [3]

described by a hydrogenic Hamiltonian [4]:

$$H = -\frac{\hbar}{2m_h^*} \nabla_h^2 - \frac{\hbar}{2m_e^*} \nabla_e^2 - \frac{q^2}{\varepsilon \mid r_e - r_h \mid}$$
 (1.4)

 \hbar is the Planck constant. m_h^* and m_e^* are the effective masses of hole and electron. ε is the dielectric constant. By solving the equation using this model, the relation of the diameter of the 1D semiconductors and band gap energy can be expressed as [5]:

$$Eg_n = Eg_p + \frac{\hbar^2 \pi^2}{2d^2} \left(\frac{1}{m_h^*} + \frac{1}{m_e^*}\right) - \frac{1.8q^2}{\varepsilon d}$$
 (1.5)

 Eg_p is the bandgap energy of planar material. Eg_n is the bandgap energy of the quantum confined semiconductor. d is the diameter of the 1D semiconductor. The bandgap of a semiconducting CNT is give by the equation [6–9]

$$Eg_c = \frac{4\hbar v_f}{3d_{CNT}} \tag{1.6}$$

where v_f is the fermi velocity, and \hbar is the Dirac constant. It shows that bandgap energy is inversely proportional to the diameter.

One type of CNT has a multi-wall structure, comprising of multiple hollow cylinders with

different diameters, called multi-wall CNT (MWCNT). The diameter of a MWCNT can be easily tailored by electrical breakdown. It has been demonstrated that the peak responsivity of the MWCNT photodetectors can be tuned to the desired wavelength by controlling the diameter of MWCNTs through electrical breakdown [10].

1.2.4.3 Multiple Electron and Hole Pairs Generation

Absorption of a single photon typically creates only one electron and hole pair, resulting in energy loss because excess energy from photons with energies greater than the semiconductor bandgap is loss through phonon emission. However, absorption of a single photon with high energy can potentially create more than one pair of electron and hole, since the excess energy of a hot electron can excite other electron across their bandgaps.

The creation of multiple electron and hole pairs via absorption of a single photon is a well-known phenomenon in planar semiconductors [11]. However, the efficiencies are insignificant for bulk materials. It has been proposed that generation of multiple electron and hole pairs is more efficient in quantum confined materials due to the well-separated discrete energy bands in the quantum confined materials that should slow phonon-assisted carrier cooling (phonon bottleneck). This makes multiple electron and hole pairs generation more competitive with other relaxation pathways.

An efficient multiple electron and hole pair generation process was observed in a CNT p-n junction photodiode [12]. In the CNT p-n junction, a single photon with energy larger than E_{22} (energy of two times of band gap energy) is converted into multiple electron and hole pairs, leading to enhanced photocurrent and increased efficiency. This process could potentially result in higher photon-to-current conversion efficiencies.

1.2.4.4 Reduced Scattering

Once the photo-excited carriers were separated by built-in potential in the depletion regions, they need to transport to the electrodes in order to be collected, and thus contribute to photocurrent generation. The efficiency of photodetectors was reduced by the scattering of carriers during the transportation to the electrodes. The efficiency can be increased if the carrier scattering reduced.

It was demonstrated that scattering was reduced in a 1D material based device: ballistic transport (no scattering) was observed in a CNT based field effect transistor (FET) at room temperature [13]. Contacting semiconducting CNT by Pd greatly reduced or eliminated the barriers for transport through the valence band of nanotubes. The 'ON' states of FET can behave like ohmic contacted ballistic metallic tubes, exhibiting room temperature conductance near the ballistic transport limit of $4q^2/h$ and high current-carrying capability.

1.2.4.5 Higher Defect Tolerance

Another advantage of the 1D photodetectors is the suppressed sensitivity to defects. Simulation results predicted that 1D materials with radial p-n junctions show only a slight efficiency degradation with decreasing lifetime until the minority carrier diffusion length approaches the nanowire radius, whereas planar p-n junction shows severe degradation once the diffusion length drops below the film thickness [14].

1.2.5 Carbon Nanotube Based Photodetectors

The basic theory of planar semiconductors cannot directly apply to the 1D structures due to the quantum effects [15], thus the behavior of CNT based photodetectors may be different

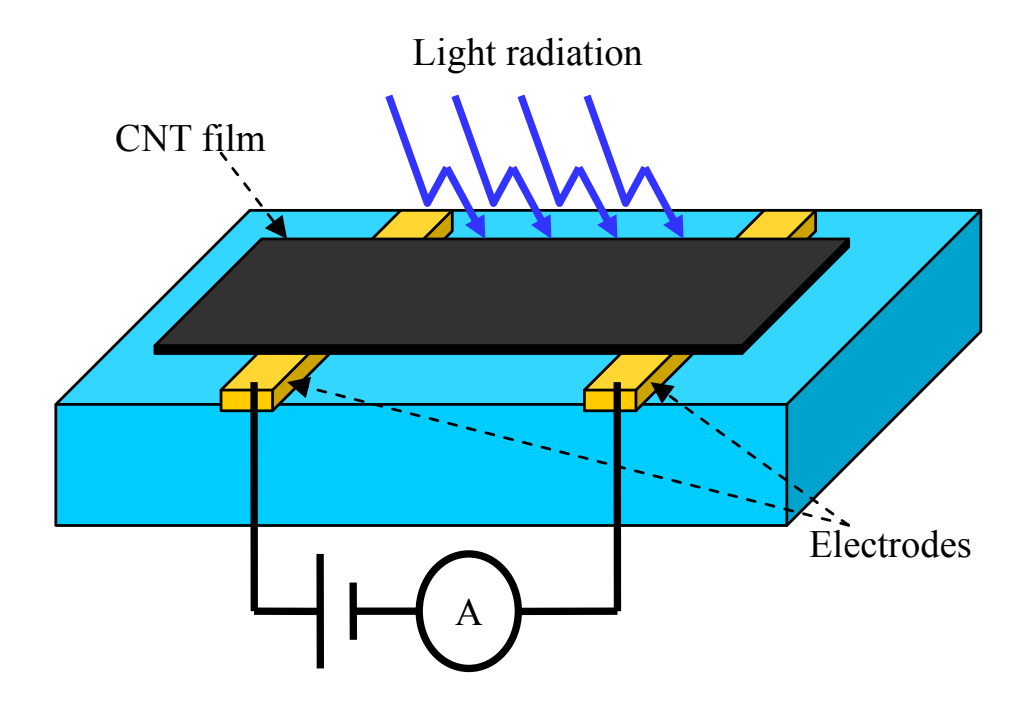


Figure 1.6: The structure of a CNT thin film photodetector.

from traditional photon detectors. The photoconductivity of CNTs has been extensively studied, and photodetectors with a number of different structures were reported. A review of different photodetectors will be given as follow.

By depositing CNT thin film between two pre-patterned electrodes with insulating gap, infrared detection was first realized by observing the conductance change with infrared radiation on the device [16], as shown in Figure 1.6. However, not only the mixture of metallic and semiconductor CNTs in the film severely degraded the response of the thin film photodiode, but also the adsorbed oxygen in the film decreased the photo-sensitivity. In order to improve the performance of the thin film detector, CNT was embedded into the polycarbonate nanocomposite [17]. This insulating polymer matrix dramatically enhanced the photo-response, since the nano-composite changed the detection mechanism from a thermal effect into a photo effect.

Instead of connecting CNT film to the metal electrodes, detectors can also be fabricated by stacking CNT film onto the bulk silicon substrate [18]. In this structure, the contact between CNTs and silicon form heterojunctions, which are responsible for the photocurrent generation. Nano-optoelectronic devices using films or sheets will lose some particular properties and advantages due to the interaction between nanotubes. By growing CNTs on a nanoporous anodic aluminum oxide (AAO) template, the interaction of CNTs can be eliminated [19], as shown in Figure 1.7. This synthesis method will form a periodic dense array of CNTs that are parallel to each other and perpendicular to the silicon substrate. In this heterojunction system, several mechanisms may contribute to the photo-response. It is very difficult to fully understand its underlying operation mechanism, since the two materials are very dissimilar in bandgap, workfunction, and dimensionality, and the synthesized CNTs may have varied properties.

A single CNT is a perfect 1D system, therefore photodetectors using a single CNT is more favorable, and easier controlled for manufacturing. Studying the single-CNT-based photodetectors can help us understand the real operation principle of the 1D detectors, which will lead to the fabrication of photodetectors with optimized performance.

Photoconductivity of a single-CNT-based p-n junction photodiode was observed by fabricating two split gates underneath both ends of a semiconductor CNT [20], as illustrated in Figure 1.8. By applying opposite gate voltages with high amplitude to the split gates, the CNT at both ends will be electrostatically doped into p and n type semiconductor, resulting in the formation of a p-n junction in the CNT. The fabrication begins with a thick thermal oxide grown on a heavily doped Si wafer. Split gates were formed using Mo. Using the split gate metal as an etch mask, part of oxide was dry etched. Next, a thin layer of silicon oxide was deposited, forming the gate dielectric for the split gate. The source and drain contacts

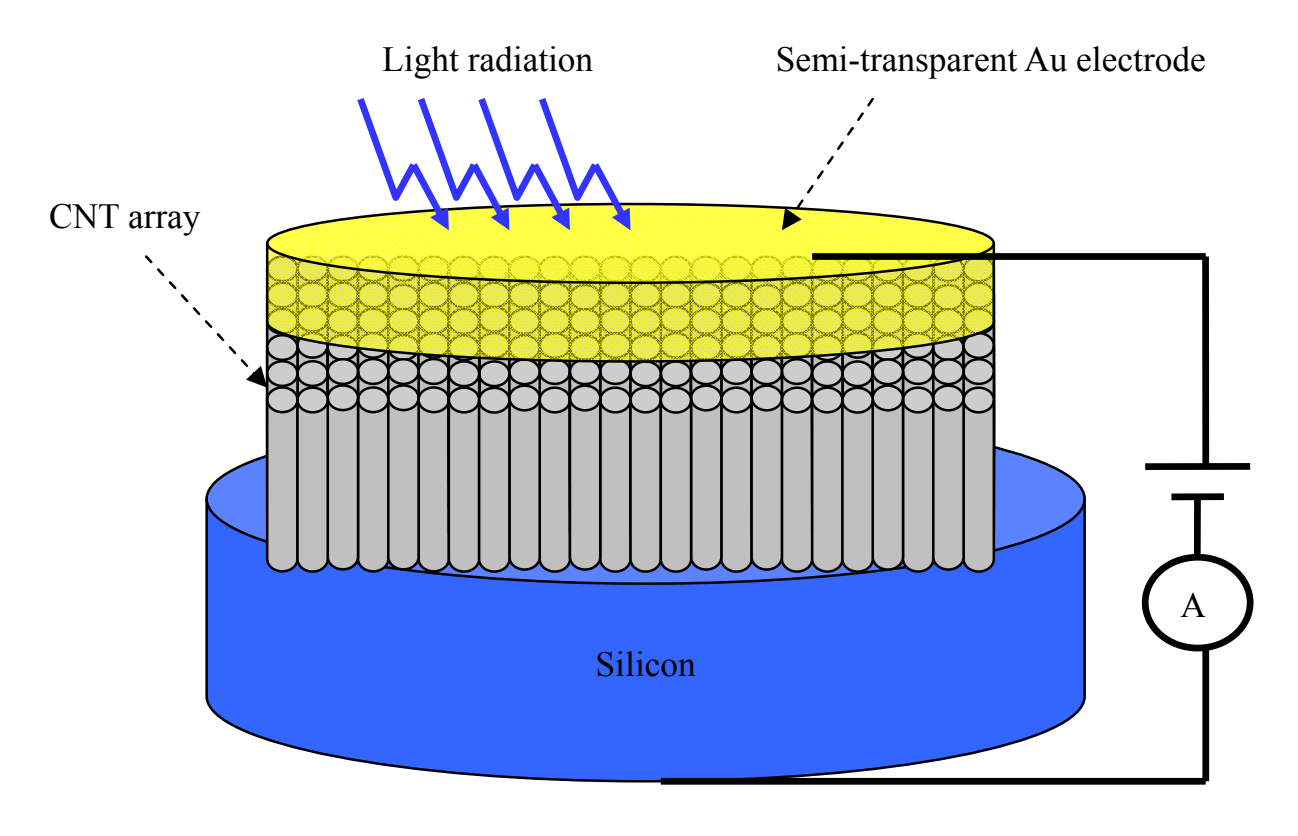


Figure 1.7: The structure of a silicon-CNT heterojunction photodetector with nanoporous anodic aluminum oxide (AAO) template to separate the vertical CNT array.

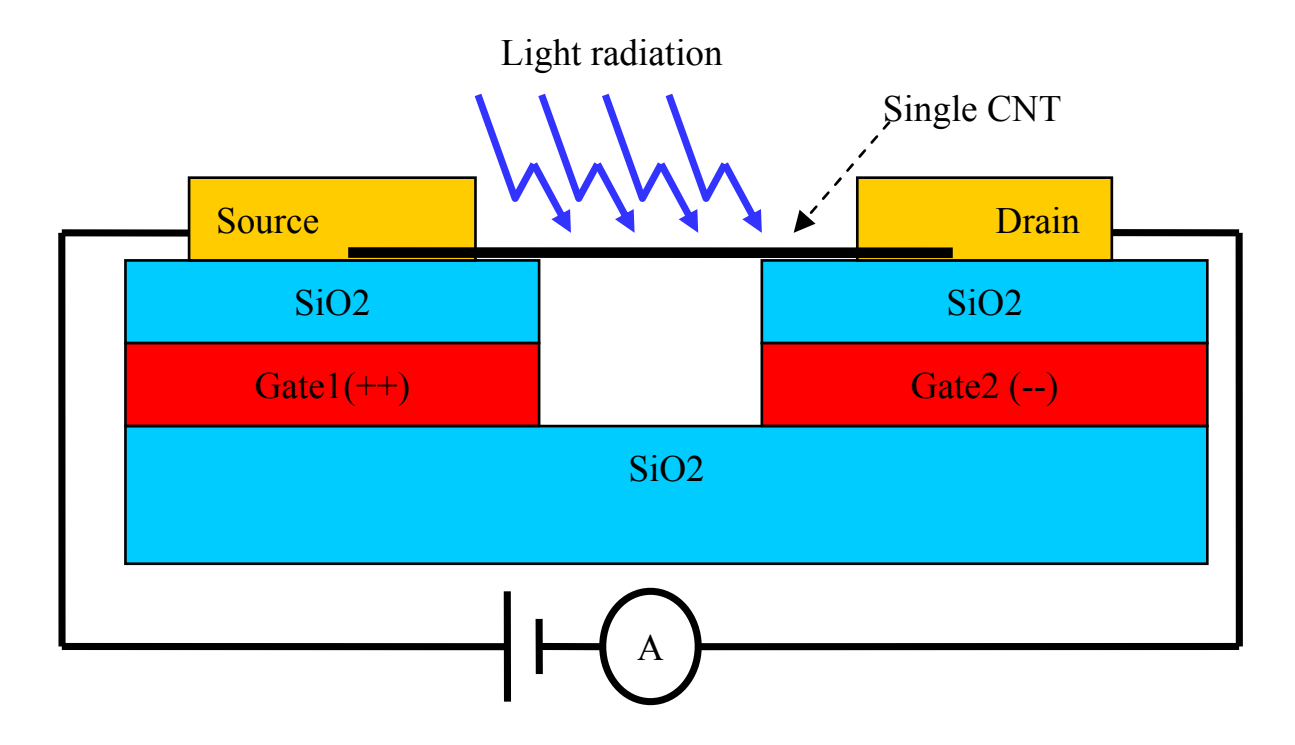


Figure 1.8: The structure of a single CNT based p-n junction photodiode.

were then lithographically defined. Finally, CNTs were grown on top of the source and drain metals. In the center of the device, where the built-in field is greatest, photo-generated electron and hole pairs were separated, causing currents to flow. This photodiode provided some insights to the CNT detector, and showing some promising results [20].

However, the fabrication process of the device is too complicated, which will hinder its applications in wide realm. Therefore, a CNT detector with simpler structure is needed. CNT Schottky photodiode emerged as an alternative.

When metal and CNT come into contact, a Schottky barrier may be formed depending on the Fermi energy alignment. The Schottky barrier determines the electrical and optical properties of the CNT devices. However, the importance of the Schottky barrier was neglected at early stage of developing CNT based devices, when researches attributed the electrical properties of the device to the intrinsic properties of the CNT [21] rather than the contacts. With the development of CNT field effect transistors (CNTFETs), increasing evidence suggested that the Schottky barrier played a key role in determining the characteristics of the nano-devices [22].

It was demonstrated that Schottky diodes between an individual SWCNT and metals were responsible for the photocurrent generation under continuous infrared illumination [23]. Figure 1.9 shows the structure of Schottky photodiode that has a much simpler configuration than the p-n junction photodiode.

The main reason of generating photocurrent in the CNT Schottky barrier photodiode is the depletion regions of the barrier. Photons with energy higher than the band gap of CNT can produce electron and hole pairs or excitons in the entire CNT, whereas the current flow is only distributed to the depletion region, since the built-in potential in the depletion region (and within diffusion length) can separate the photo-generated electron and hole pairs, and thus produce photocurrent, while the electron and hole pairs outside the depletion region will recombine shortly.

The Schottky photodiodes have shown superb performance and the simplest structure. However, there was no systematic study about optimizing the design of CNT based Schottky photodiodes. The performance of CNT based photodetectors is extremely important to the IR sensing systems. We will focus on investigating the Schottky barrier based photodetectors of single CNTs, and optimizing the structure of the photodetectors.

1.3 Objectives and Challenges

The objective of this research is to develop a high performance IR sensing system that utilizes a CNT based photodetector as its core component. The system development involves

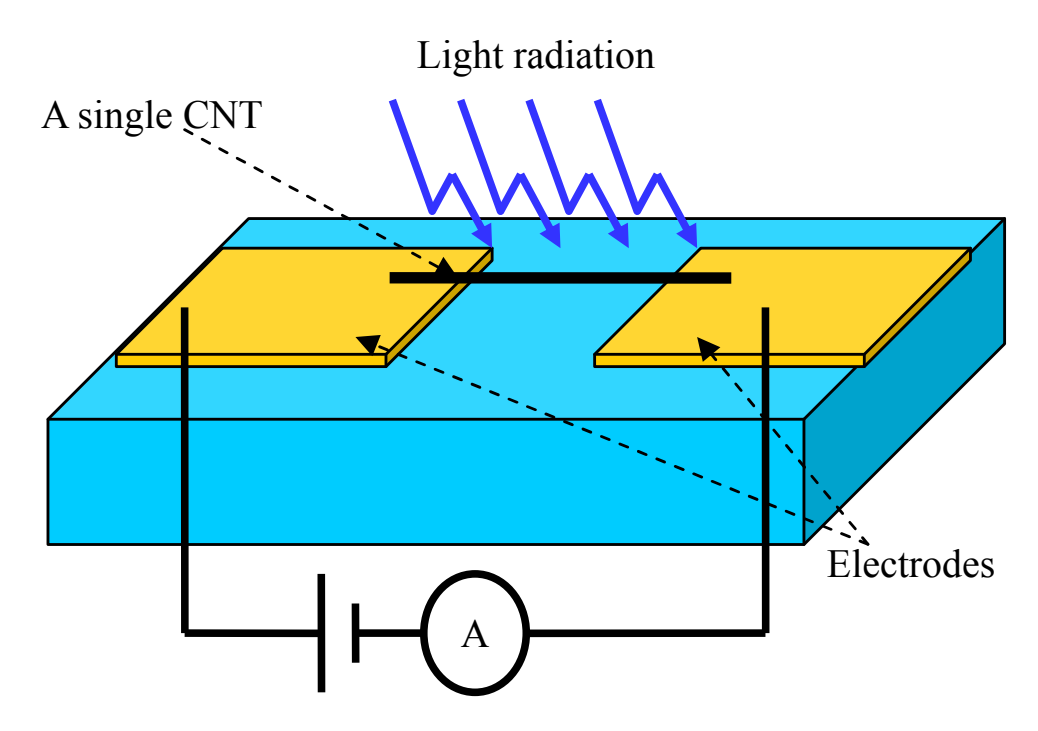


Figure 1.9: The structure of a single-CNT-based Schottky photodiode.

three main parts: (1) develop a CNT based photodetector with high performance and simple fabrication process; (2) explore nano-structured light confinement components that integrate with CNT based photodetectors, due to the sub-wavelength size of the photodetectors; (3) develop a novel sensing system structure that can use a few or even a single phodetector. In order to accomplish this work, not only the theoretical designs of photodetectors, light confinement components, and camera structure were involved, but also fabrication and experimental testing were performed.

The main challenges involved in this research include:

• Design and fabrication of high performance photodetectors using a single CNT. Due to nanometer-scale diameter of the CNTs, reliable and high-yield manufacturing was difficult to accomplish in order to fabricate CNT based photodetectors. In addition, the optimized photodetector design may be different from conventional devices due to the unique quantum confined geometry of CNTs.

- CNTs with appropriate bandgap energies for MWIR detection. There was not a reliable synthesis technique that can grow CNTs with uniform electrical and optical properties.

 In particular, it is difficult to control the bandgap energy of CNT to detect MWIR.
- Light confinement to the CNT based photodetectors with sub-wavelength size. A single CNT has a diameter of as small as sub-nanometer, while detection wavelength is much larger than the diameter of the CNT, resulting in small fill factor (absorption area). Traditional lens cannot address this problem due to the light diffraction. It is a challenge to develop a light confinement component that can trap light onto the CNT based photodetectors.
- Proper sensing system architecture to integrate with CNT based photodetectors. It is difficult to fabricate large focal plane array of CNT based photodetectors. Conventional camera structure addressed this problem using scanning configuration to scan each pixel per cycle, making the sensing system slow and inefficient.

1.4 Organization of the Study

Design, fabrication and testing of CNT Schottky photodiodes are presented in Chapter2 to investigate the importance of metal structure. It is followed by developing CNT field effect transistor (CNTFET) based photodetectors in Chapter3 to study the dependence of photoresponses on electrostatic doping. In Chapter4, spectral responses of SWCNT and MWCNT based photodetectors are compared, and breakdown process is introduced to engineer the bandgap energy of MWCNT. In Chapter5, bowtie antenna is described to improve the fill

factor of the CNT photodetectors. In Chapter6, photonic crystal cavity was utilized to further increase the fill factor of the CNT photodetectors. Chapter7 introduces the novel sensing system architecture that enables capture high resolution images using even a single photodetector. Chapter8 presents the conclusions and future works.

Chapter 2

Carbon Nanotube Schottky

Photodiodes

Understanding the 1D Schottky barrier within CNT is important. The traditional Schottky barrier theory for planar contact between metal and bulk semiconductor is well established, and can lead to optimized photodiode design. However, the conventional understanding of the Schottky barrier cannot be applied to 1D Schottky barriers between metal and nanotubes, since the planar contacts are dominated by the metal-induced gap states (MIGS), whereas the MIGS induced Fermi level pining is trivial for the 1D structure [15] due to quantum confinement. Therefore the physics and fundamentals of 1D Schottky barriers within a CNT need to be reexamined. In the following sections, I will introduce the design, fabrication, testing and analysis of the CNT Schottky photodiodes so as to understand their working principle.

2.1 Design of the CNT Schottky Photodiode

After photons were absorbed by semiconductor CNTs, photo-generated electrons will be separated by the electric field within the Schottky barrier, and need to tunnel though the barrier before contributing to the photocurrent. The Schottky barrier width determined the effective absorption area, while the built-in potential within the barrier determined the

speed of separated carriers, and both barrier width and height defined the carrier tunneling probability. The basic structure of a CNT Schottky photodiode is shown in Figure 1.9, in which a single semiconductor CNT bridge two metal electrodes to form the Schottky barriers.

Figure 2.1(a) shows the energy alignment between a metal (take Au as example) and a CNT. The CNT was reported as a p-type material in the air with Fermi energy of around 5 eV [24] due to oxygen doping or some accidental doping during the synthesis [25]. The workfunction (Fermi energy) of Au is also close to 5 eV, and it can be slightly smaller or higher than 5 eV due to the environmental differences [26] (in the Figure 2.1(a), the Fermi energy of Au is slightly smaller than CNT). The majority carriers of the semiconductor CNT are holes, therefore the energy difference between the Au workfunction to the CNT valence band (Ev) is indicated as the barrier height. When CNT connect two Au electrodes at both ends, denoted as symmetric photodetector, two symmetric Schottky barriers will be formed at the contacts, as shown in Figure 2.1(b).

This structure results a photodiode that consists of two Schottky barriers inversely connecting to each other. When the photons with energy higher than the CNT bandgap strike the CNT, electron and hole pairs will be generated and separated in the depletion region, as indicated in Figure 2.1(b). Hence, the total photocurrent under zero bias is calculated by $I_{photo} = I_{left} + I_{right} = i_{b1} - i_{b2}$. These symmetric barriers significantly reduce the sensitivity of the photodetector, since the separated carriers need to tunnel through another barrier before being collected. What is more, this structure detects the signal intensity difference between two contacts, resulting in poor performance.

Asymmetric photodetectors, using metals with high/low workfunctions to connect two ends of a single CNT, can be used to improve the performance of the detectors. The energy alignment and resulting band diagram are shown in Figure 2.2. On the left contact, the

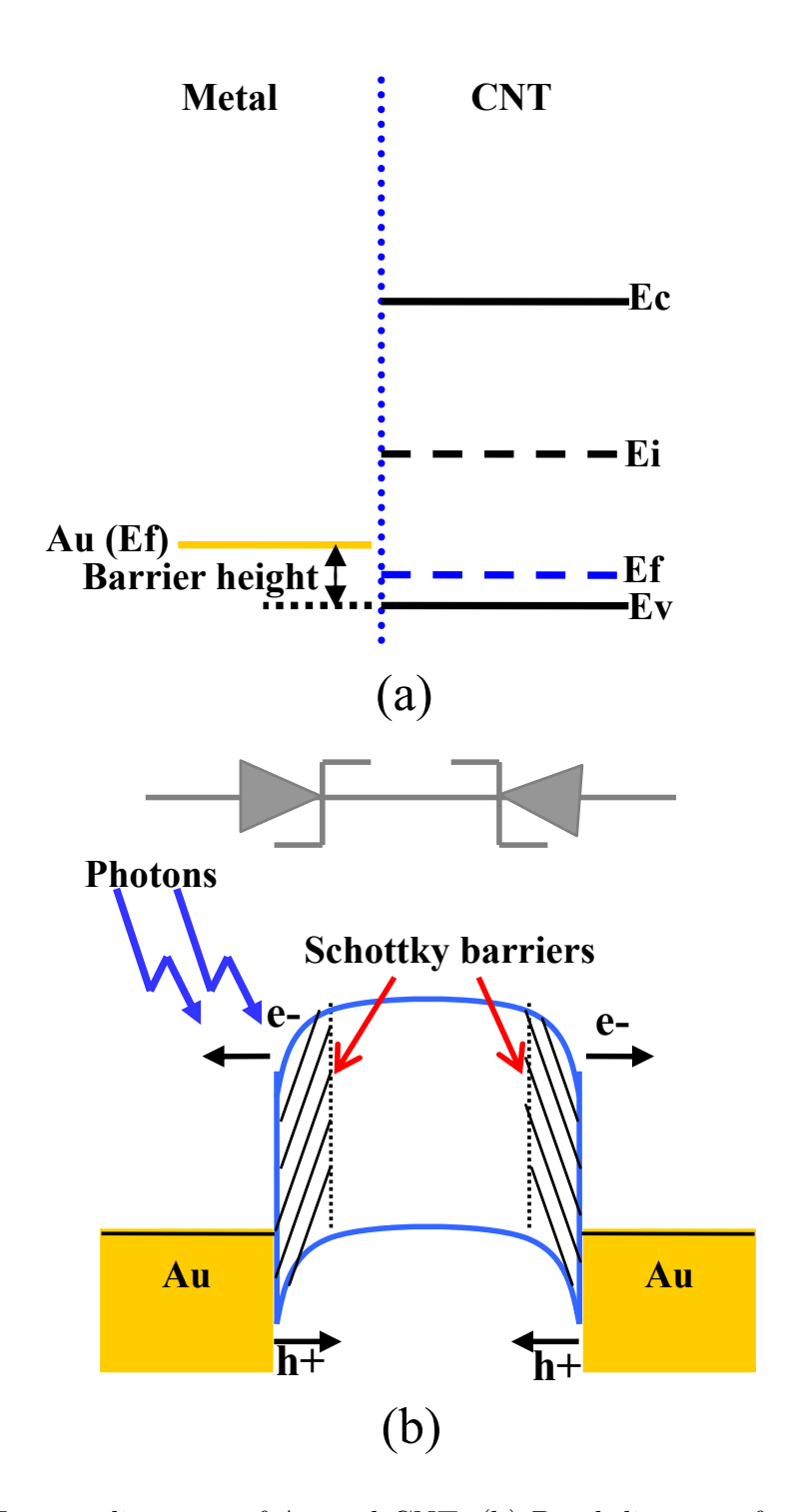


Figure 2.1: (a) Energy alignment of Au and CNT. (b) Band diagram of a symmetric CNT photodetector.

metal has a workfunction that is smaller than the CNT and forms a Schottky barrier, while on the right contact, the metal workfunction is higher than the CNT and forms an ohmic contact. The electrical and optical properties of this device will be determined by one Schottky barrier. Thus the total photocurrent will only depend on one Schottky barrier rather than the difference between the photocurrent of two barriers as in the symmetric structure. Moreover, by transferring one of the Schottky barriers into ohmic contact, the photo-generated electron holes at the Schottky barrier will be able to transport through the contact easily. As a result, the photo-response of the CNT photodetector is expected to be highly enhanced in the asymmetric structure.

2.2 Symmetric Schottky Photodiodes

An AFM image of a symmetric CNT Schottky photodiode with Au electrodes is shown in Figure 2.3. An individual single wall CNT (SWCNT) connects two Au electrodes on top of a quartz substrate. The fabrication process begins with making two Au electrodes with an insulating gap of approximately 1 μm by photolithography, thermal evaporation, and lift-off. After that, a droplet of SWCNT suspension (ethanol) was dropped to the gap between electrodes that connects to the dielectrophoresis (DEP) deposition system [27]. An individual SWCNT was deposited between the electrodes by optimizing the suspension concentration, and assisted by the atomic force microscope (AFM) manipulation system [28] [29] [30]. A more detailed fabrication process was discussed in [31] and [32].

The properties of the Schottky barriers are determined by the energy alignment between the metals and SWCNT; thus Schottky photodiodes made of different metals were investigated to understand the importance of the metal workfunctions.

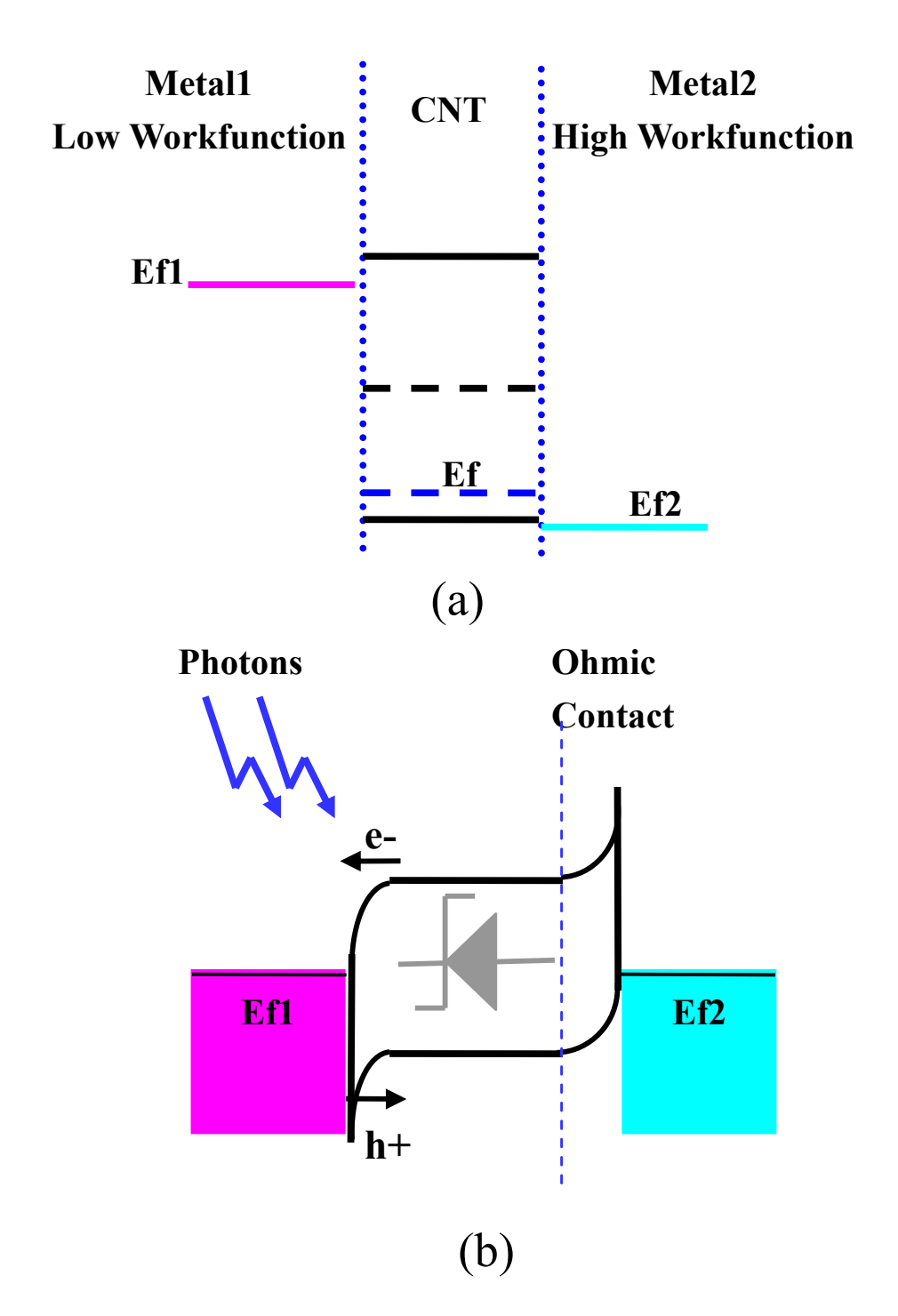


Figure 2.2: (a) Energy alignment of metals with high/low work functions and CNT. (b) Band diagram of the asymmetric CNT photo detector.

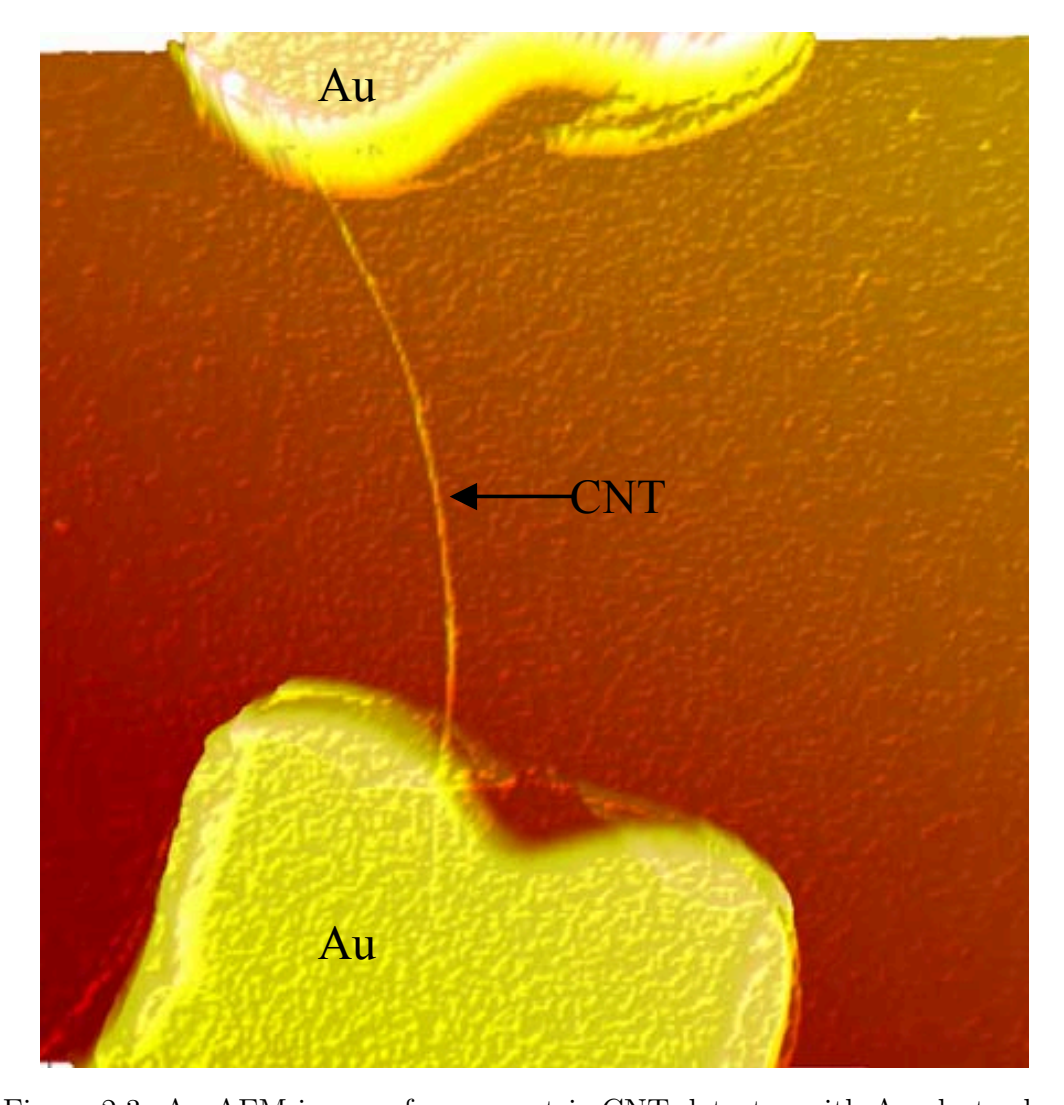


Figure 2.3: An AFM image of a symmetric CNT detector with Au electrodes.

The I-V characteristics of symmetric Schottky photodiodes with four different metals (Pd, Au, Cu and Al)were studied. Their typical I-V curves are shown in Figure 2.4, which based on more than 100 devices tested in our laboratory.

Figure 2.4 shows that the I-V characteristics for positive and negative biases are symmetric, indicating the symmetric barriers at both ends, while the conductance of these devices varied significantly. The Pd-CNT-Pd diode shows linear I-V characteristics, implying an ohmic contact or very weak Schottky barrier, which has been verified in [13]. A quasimetallic I-V characteristic of the Au-CNT-Au (weak parabolic) was observed, which resulted from two small Schottky barriers reversely connecting between the source and drain, since Au and SWCNT have similar workfunctions. While Cu and Al have much smaller workfunctions than SWCNT; the contacts between these metals with CNT form larger Schottky barriers, which is illustrated by the band diagram shown in Figure 2.1. Consequently, the Cu-CNT-Cu and Al-CNT-Al photodiodes have much smaller conductance. The highest conductance magnitude difference for these 1D photodiodes was approximately four orders, indicating the importance of the metal workfunctions. In conventional planar contacts, metal-induced gap states (MIGS) dominate the contacts, which weakens the role of metal workfunction in determining the properties of 3D Schottky barriers. That is to say, the 1D Schottky contacts have a much larger flexibility to tune the performance of the detectors by selecting proper metals.

In a conventional bulk Schottky diode, carrier injection is dominated by thermionic emission, while the thermal assisted tunneling dominates the carrier injection in the 1D Schottky barrier [33]. Temperature-dependent I-V characteristics of a Au-CNT-Au photodiode is shown in Figure 2.5. The conductance was reduced significantly as the temperature decreased from 300 K to 80 K, resulting in dark current suppression, since the decrease temperature

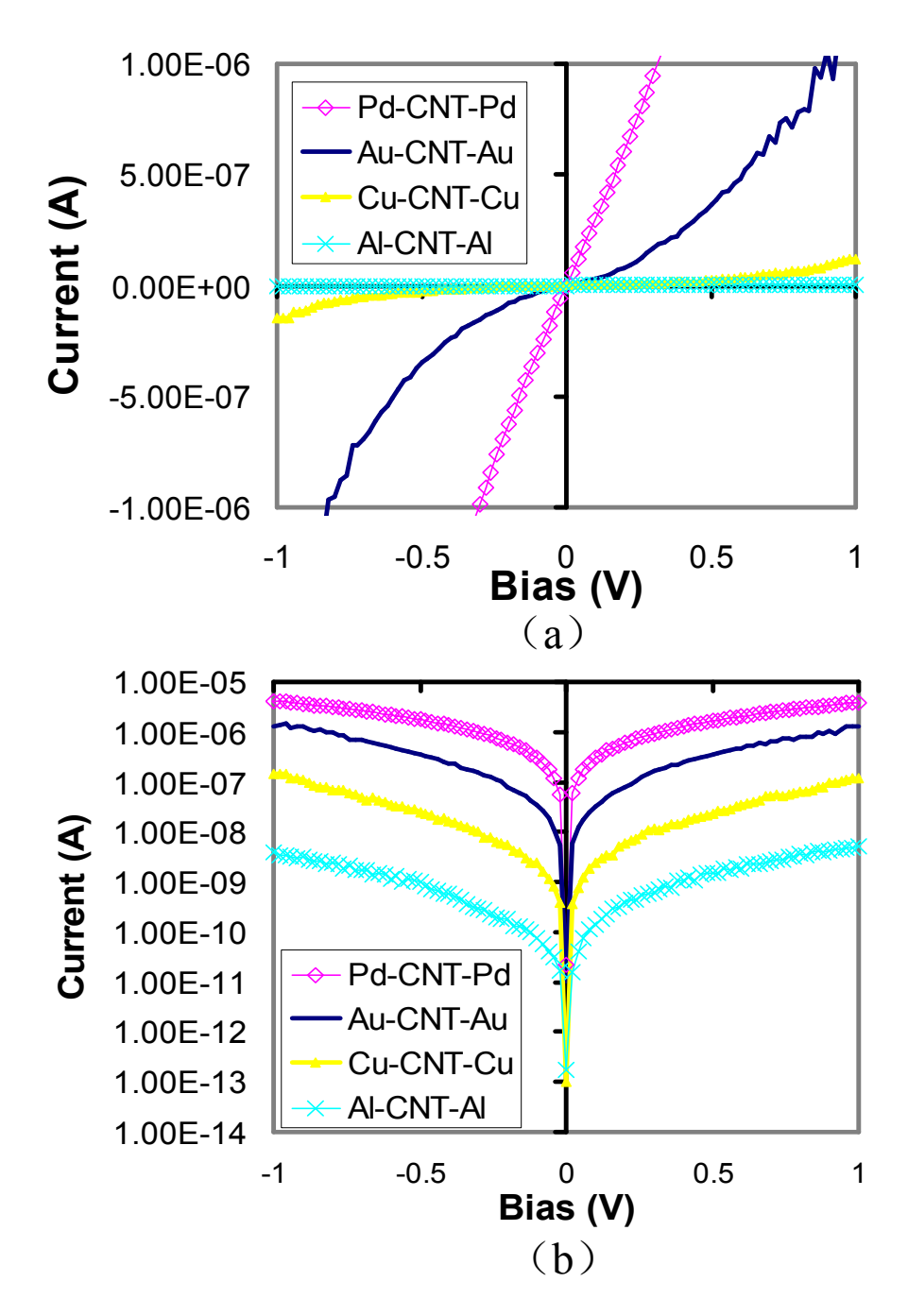


Figure 2.4: (a)I-V characteristics of CNT Schottky diodes with four different metals (Pd, Au, Cu and Al). (b)The I-V characteristics shown in logarithm scale.

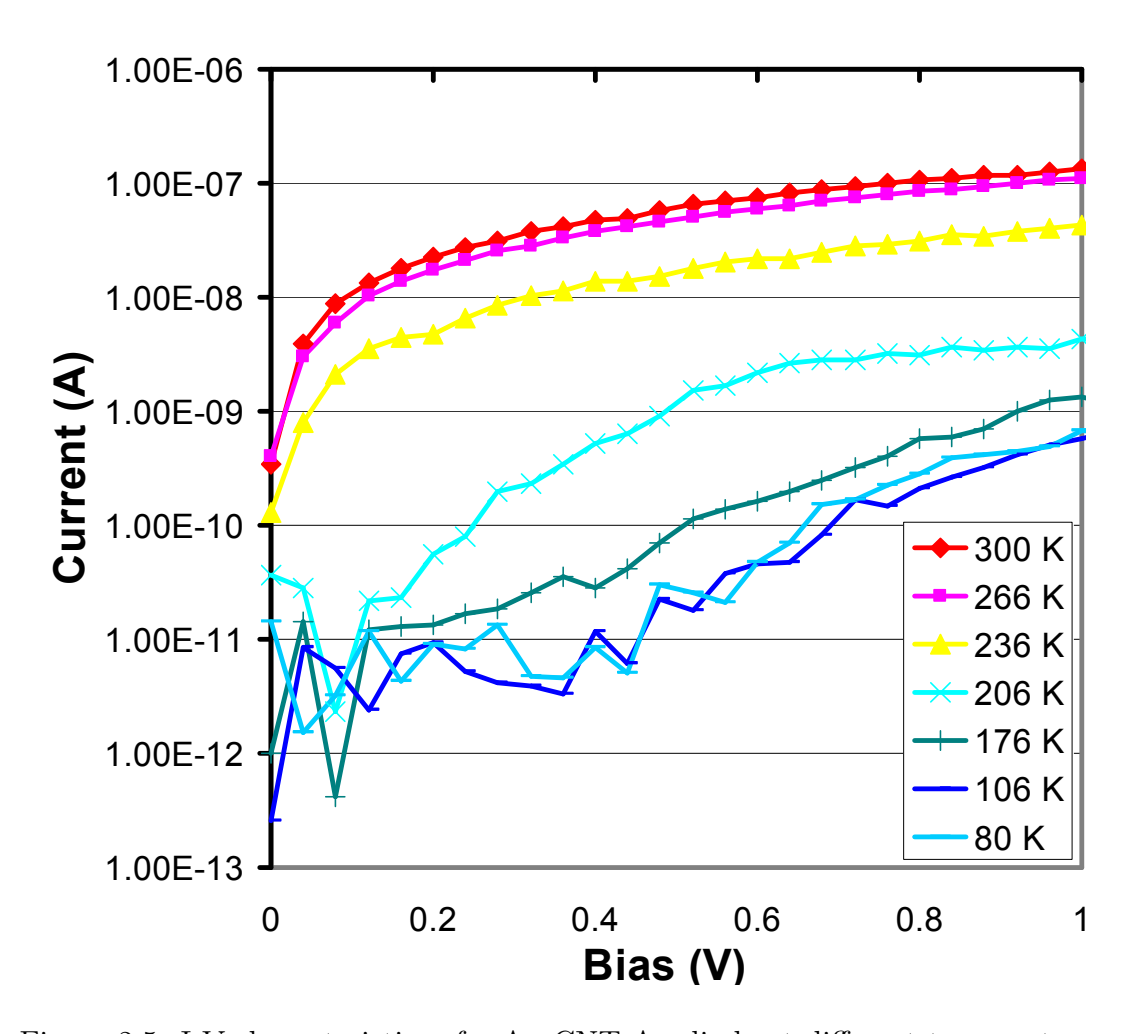


Figure 2.5: I-V characteristics of a Au-CNT-Au diode at different temperatures.

depresses the tunneling probability of carriers through the barriers.

The photo-responses of the Schottky photodiodes were also investigated. The testing system consisted of a 830 nm IR laser, radiating on a CNT detector housed in a chamber after passing through an IR window, which was schematically depicted in [34]. The current signal was measured using Agilent 4156C semiconductor analyzer by periodically switching the IR source ON and OFF. All measurements were conducted at zero bias. Figure 2.6 shows the IR response of a SWCNT Au-CNT-Au photodiode by radiating IR photons on its left and right contacts. One distinct characteristic is that the photocurrent changed direction but kept similar magnitude $(1.5 \times 10^{-11} \text{A})$ when the laser illuminated at two different contacts.

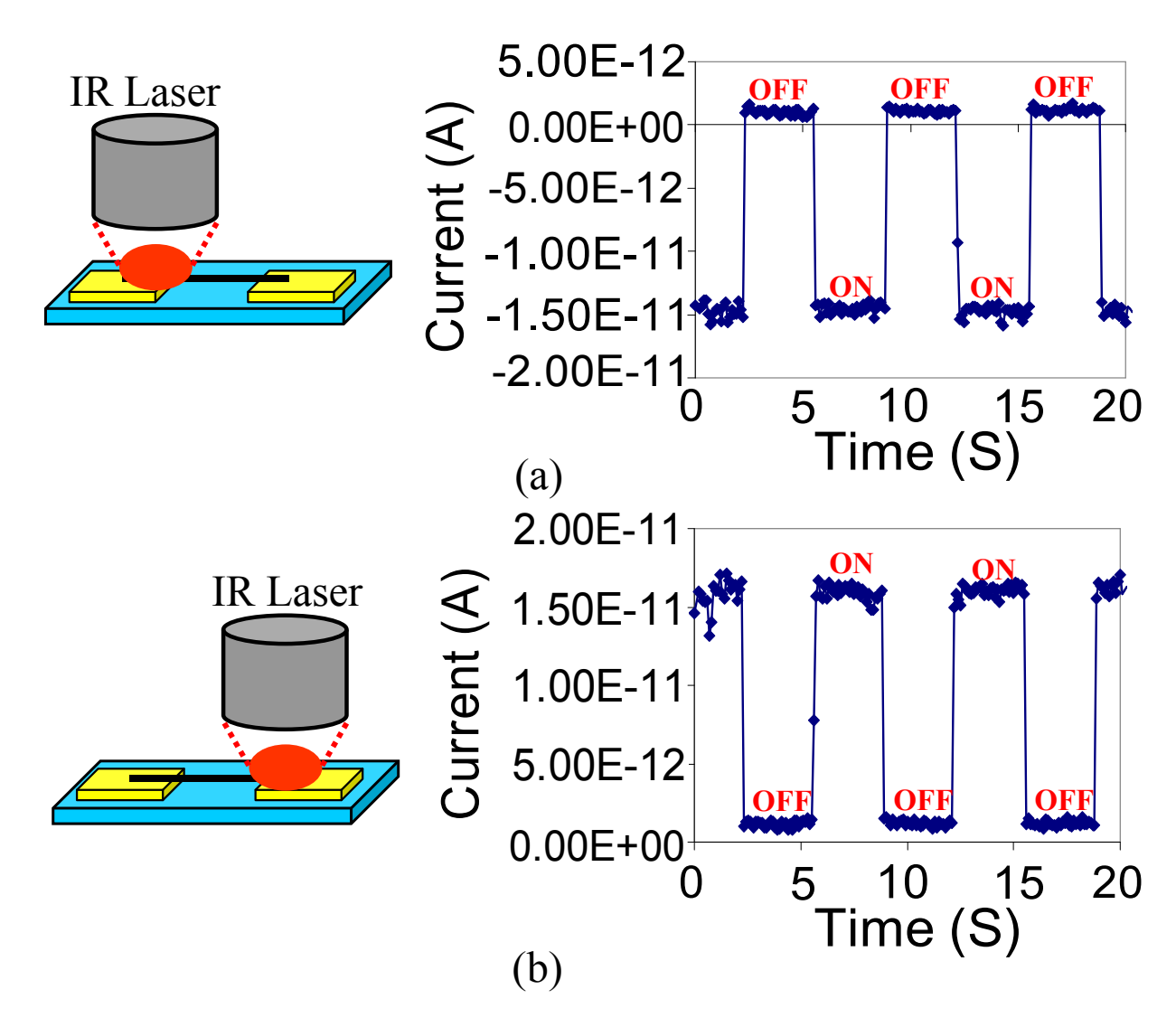


Figure 2.6: The IR responses of a Au-CNT-Au Schottky photodiode by radiating on (a) left electrode, (b) right electrode.

This is caused by two symmetric Schottky diodes between Au and CNT inversely connecting to each other, as indicated in the band diagram in Figure 2.1(b), a more detailed discussion can be found in [23].

The typical IR responses of four CNT Schottky photodiodes with different metals are shown in Figure 2.7 and Figure 2.8, in which IR laser was radiated at one contact.

The dark current and photocurrent (Iphoto) (current difference between IR ON and OFF) of these devices are summarized in Table 2.1. Pd-CNT-Pd and Au-CNT-Au photodiodes

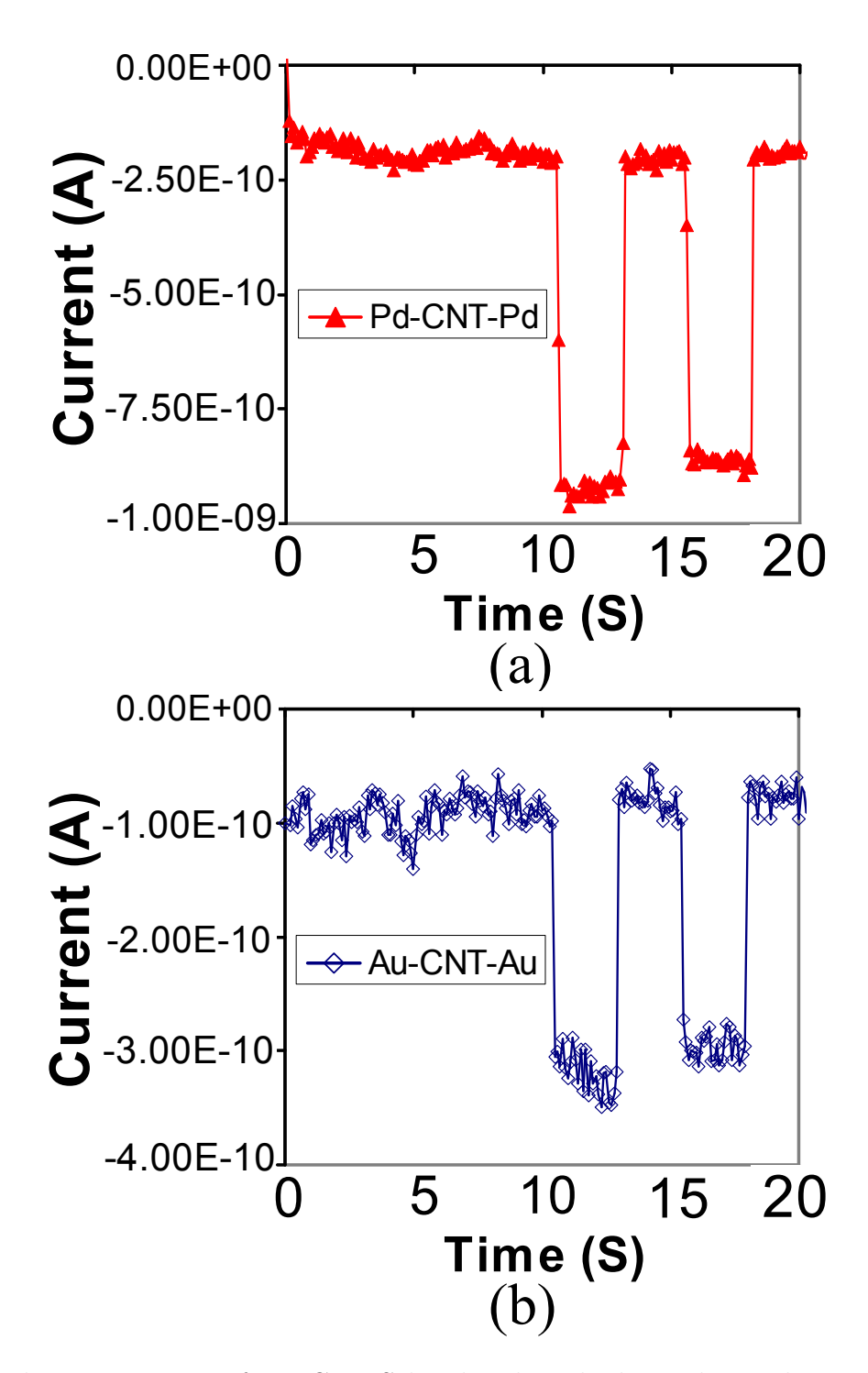


Figure 2.7: The IR responses of two CNT Schottky photodiodes with metal structures of (a) Pd-CNT-Pd, (b) Au-CNT-Au.

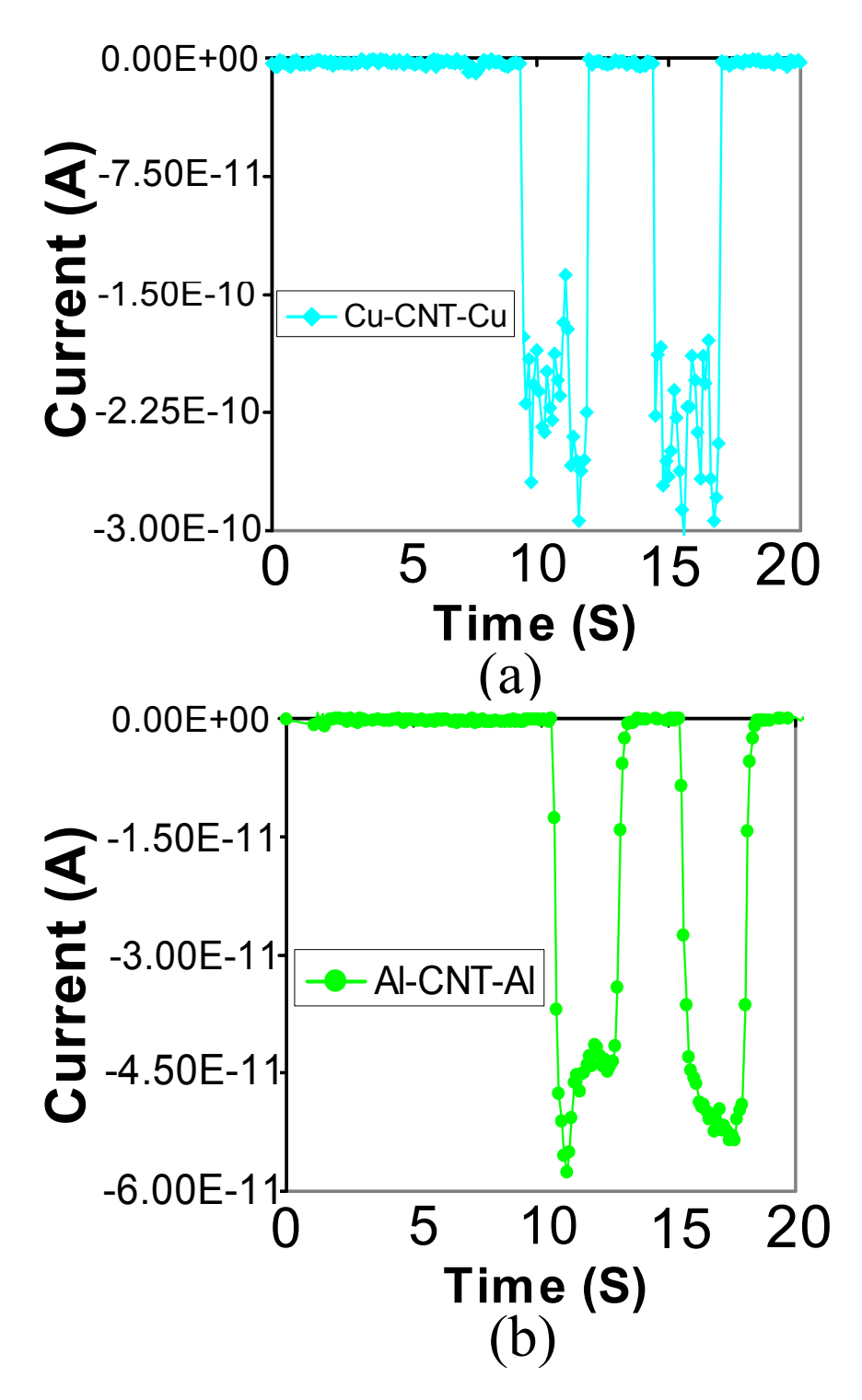


Figure 2.8: The IR responses of two CNT Schottky photodiodes with metal structures of (a) Cu-CNT-Cu, (b) Al-CNT-Al.

had relatively high dark current and photocurrent. This can be explained that both injected and photo-generated carriers are easily tunneling through the weak barriers. In contrast, the Al-CNT-Al photodiode had two strong barriers, making the carriers difficult to tunnel through. As a result, it has relatively low dark current and photocurrent. The Cu-CNT-Cu photodiode had moderate Schottky barriers, resulting in the highest signal-to-noise ratio among them.

Table 2.1: Performance of Four Detectors with Different Metals

SWCNT IR Detectors	Dark Current (A)	Iphoto (A)
Pd-CNT-Pd Au-CNT-Au	2.0×10^{-10} 1.0×10^{-10}	7.0×10^{-10} 2.0×10^{-10}
Cu-CNT-Cu Al-CNT-Al	$2.0 \times 10^{-12} \\ 9.0 \times 10^{-13}$	$2.3 \times 10^{-10} $ 4.5×10^{-11}

The importance of the signal-to-noise ratio of nano-devices needs to be emphasized here. Nano-photodetector is difficult to have photocurrent comparable to bulk photodiodes due to the small fill factor. However, the open circuit voltage (Voc) is determined by the ON/OFF ratio (the ratio between IR ON and OFF), which can be high even absorbing small amount of photons, because the dark current can be extremely low due to its nano-scale size and phonon scattering suppression in 1D structure. The typical IR responses of Cu-CNT-Cu and Au-CNT-Au with applied bias are shown in Figure 2.9. The bias-dependent photo-response of Cu-CNT-Cu shows photovoltaic characteristics: negative bias increases the photocurrent by widening the barrier, while positive bias reduces the photocurrent due to the shrinkage of the barrier. A Voc of 100 mV was observed when injected carriers were equal to photo-generated carriers, resulting in zero net current. The short circuit current of this device is only

 5×10^{-11} A, which is negligible compared to conventional photodiodes, but it corresponds to 100 mV Voc, which is on the same order as other traditional photodiodes. The photocurrent of Au-CNT-Au with bias is difficult to observe since the dark current dominates the current flow.

In this section, the performance and characteristics of symmetric photodiodes using different metal electrodes were introduced. Pd-CNT-Pd, Au-CNT-Au, and Al-CNT-Al detectors have low signal-to-noise ratio, since they have either too small or large Schottky barriers at both ends. The Cu-CNT-Cu detector has moderate Schottky barriers, generating a high signal-to-noise ratio and Voc.

2.3 Asymmetric Schottky Photodiodes

The symmetric structure of two reversely connecting Schottky diodes will significantly suppress photocurrent generation, since the two diodes are close to each other, and the photocurrents generated at the two contacts will cancel each other. In addition, the photo-generated carriers need to tunnel through another barrier before being collected. In order to address these problems, asymmetric Schottky diodes using metals with high/low workfunctions at two ends were designed. The band diagram is shown in Figure 2.2.

In order to verify the concept of this asymmetric infrared detector, a fabrication process was designed to measure the electrical properties and IR reponses of both Au-CNT-Au and Al-CNT-Au photodiodes using a single CNT. The process began with fabricating two Au electrodes with a gap of 1.2 μm using ebeam lithography on top of a quartz substrate, as shown in Figure 2.10(a). It was followed by depositing an individual SWCNT bridging these two electrodes using the DEP and AFM manipulation system (Figure 2.10(b)). The

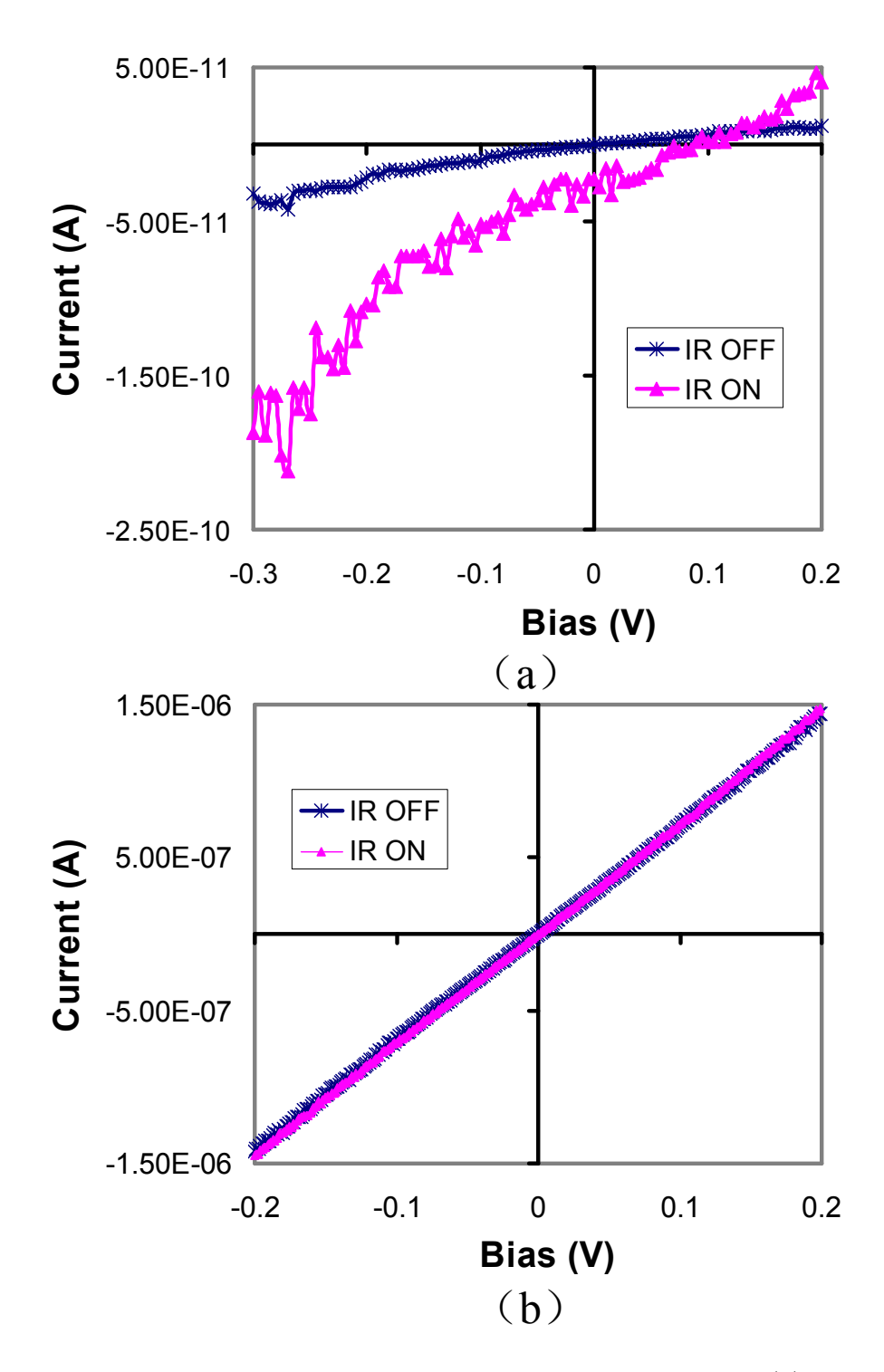


Figure 2.9: The IR responses of CNT Schottky photodiodes with bias (a) Cu-CNT-Cu, (b) Au-CNT-Au.

I-V characteristics were measured, denoted as Au-CNT-Au in Figure 2.10(d). After that, another ebeam lithography was used to pattern an Al electrode that covered one of the Au electrodes and extended 0.2 μm into the gap, making the device structured as Al-CNT-Au with a gap of 1.0 μm , as shown in Figure 2.10(c). Its electrical characteristics were measured and as shown in Figure 2.10(d), denoted as Al-CNT-Au. The Au-CNT-Au showed symmetric and quasi-metallic electrical characteristics (weak parabolic I-V characteristics with higher bias), while typical diode electrical characteristics were observed in the Al-CNT-Au structure. The electrical properties of the device changed significantly due to the replacement of an Au electrode. Therefore, there must be a higher barrier between Al and nanotube that dominates the optoelectronics properties of the detector [35].

The photo-responses of the Au-CNT-Au and Al-CNT-Au are also compared, as shown in Figure 2.11. The dark current decreased from 8.8×10^{-10} A to 1.1×10^{-11} A, while the photocurrent increased from 2.1×10^{-10} A to 2.4×10^{-9} A. The photocurrent enhancement increased the responsivity (photocurrent/infrared power) and quantum efficiency (number of generated electrons/number of photons), and both dark current suppression and photocurrent enhancement contributed to the improvement of the noise equivalent power (NEP)(noise/responsivity) and noise equivalent temperature difference (NETD). In other words, the asymmetric structure greatly increased the sensitivity and efficiency of the CNT based IR detector.

2.4 Chapter Summary

In summary, CNT based Schottky photodiodes using different metals and structures were fabricated and investigated. It was found that the workfunctions of metals play an impor-

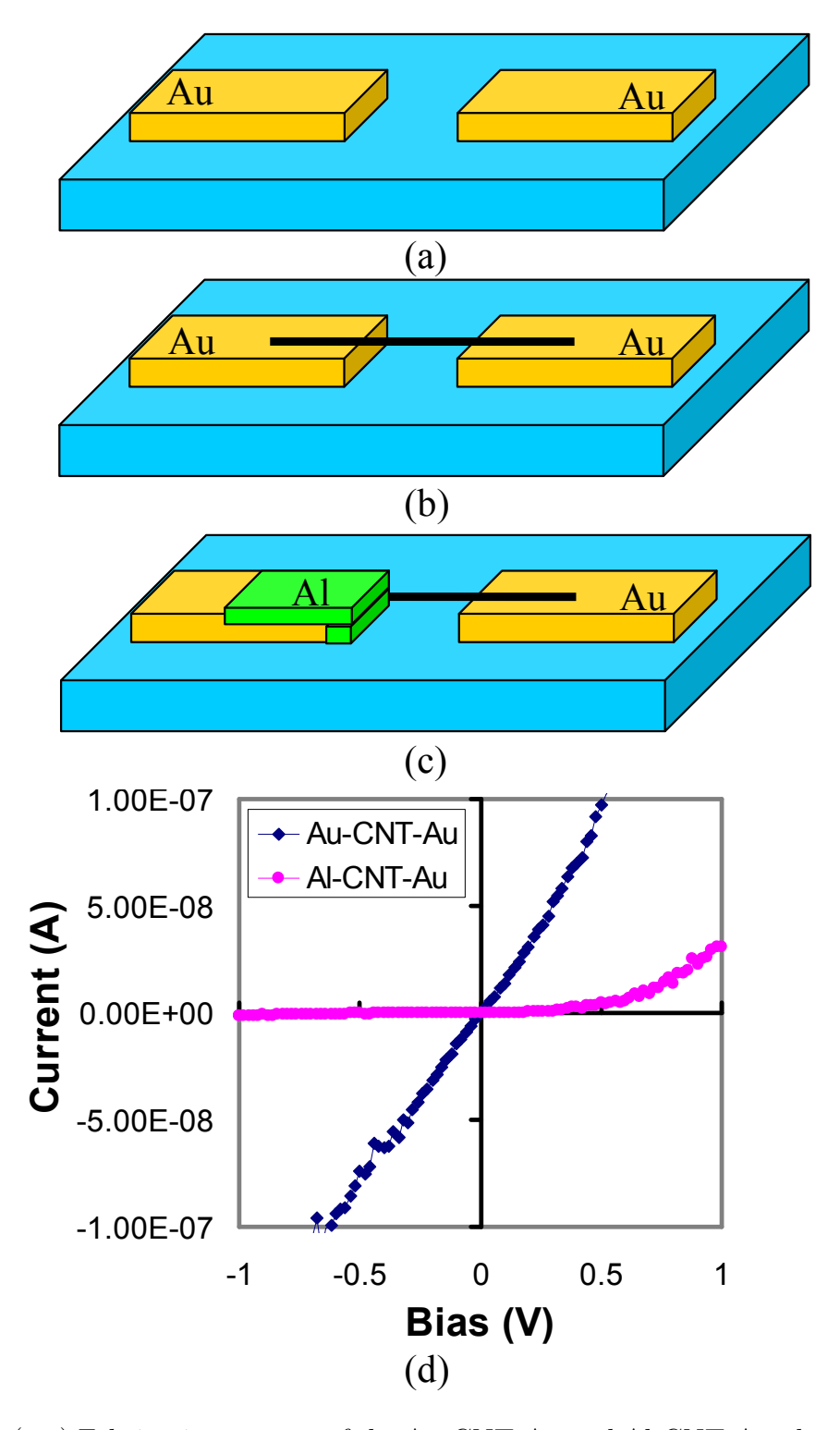


Figure 2.10: (a-c) Fabrication process of the Au-CNT-Au and Al-CNT-Au photodiodes using a single CNT. (d) Their I-V characteristics.

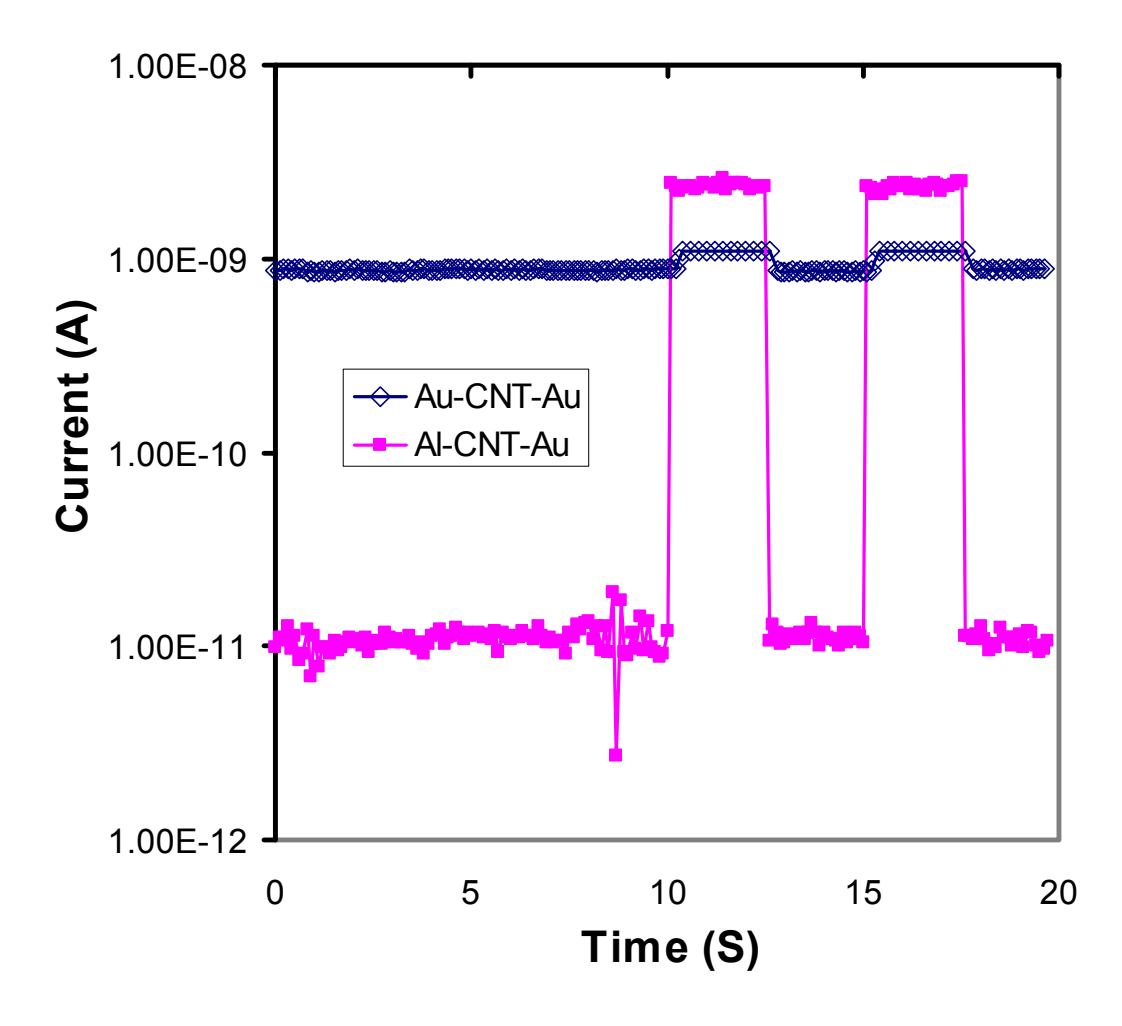


Figure 2.11: Photo-response of the Au-CNT-Au and Al-CNT-Au photodiodes using a single CNT.

tant role in determining the properties of the photodiodes. Symmetric Schottky photodiodes using different metals have varied dark current and photocurrent in several orders in magnitude. Low built-in potentials resulted in large dark current and photocurrent, while high built-in potentials caused smaller dark current and photocurrent. This can be explained by two Schottky barriers reversely connecting each other in the symmetric metal structure, which was verified by position-dependent photocurrent measurements. In order to improve the performance of CNT-based Schottky photodiodes, asymmetric structure photodiodes using metals with high/low workfunctions at two contacts were fabricated. Compared to the symmetric photodiodes, asymmetric photodiodes had lower dark current and higher photocurrent.

Chapter 3

Carbon Nanotube Field Effect

Transistor based Photodetectors

In the previous chapter, we demonstrated that 1D Schottky photodiodes between an individual CNT and metals were responsible for the photocurrent (Iphoto) generation under continuous IR illumination. The optoelectronic characteristics of CNT based IR detectors are determined by the Schottky barriers, which depend on the Fermi energy (workfunction) alignment between the CNTs and metals, therefore photo-response can be improved by selecting proper metals. However, the choices of metals are limited, especially those that are both compatible with current technology (e.g., CMOS) and have desired workfunctions. In addition, the performance of CNT Schottky photodiodes is constrained by workfunction variation caused by technical difficulties in controlling CNT synthesis [36]. Therefore, it is more effective to control the Fermi energies of CNTs in order to optimize the performance of CNT based photodetectors, instead of changing workfunctions by selecting proper metals. CNT field effect transistors (CNTFETs) can be considered as CNT Schottky diodes with an external terminal, called a gate, capacitively coupled to the CNT channel to electrostatically dope CNT by applying gate voltages (Vg). In other words, the Fermi energies of CNTs can be controlled by CNTFETs through their gates.

To begin with, a brief history of CNTFETs will be given. Conventional metal-oxide-

semiconductor field-effect transistor (MOSFET) technologies have been improved dramatically in the past decades by down scaling, which results in better performance. Down scaling of the MOSFET has recently led to a device size below 20 nm, but the ultimate limit will be reached in the near future due to current leakage. Therefore there is intense interest in finding alternative materials and devices. CNT is very promising in this respect, because its exceptional electrical properties, such as high current carrying capability and excellent carrier mobility, make it a potential candidate for replacing traditional semiconductors. CNTFETs have been demonstrated to operate in the ballistic transport regime at room temperature [13]. In addition, CNT essentially conducts current on its surface, where all the chemical bonds are saturated and stable. Thus it is compatible with high-k gate dielectrics, and there is no need to passivate the interface between the CNT channel and the gate dielectric.

The first CNTFET was reported in 1998 [21] [37]. The researches fabricated the CNTFET by dispersing CNTs in a solvent, separating bundles in an ultrasonic bath, and depositing the CNTs onto a Si/SiO₂ surface with prefabricated metal electrodes. A few of the semiconducting CNTs would bridge two electrodes and define a conducting channel between them. Modulation of the transistor conduction was achieved by applying voltages to the silicon back-gate. During the first few years after the report of CNTFETs, their working principle was not well understood. They were analyzed either like MOSFETs, barrier injection transit time (BARITT) diodes, or double 1D Schottky barrier transistors. The dominant Schottky barriers were experimentally confirmed in CNT cross-junctions made of one semiconducting and one metallic CNT in 2000 [38]. Since then, the performance of CNTFETs has been greatly improved by decreasing the thickness of dielectric layer [39], using high-k materials as gate the dielectrics [40], and eliminating barriers by forming ohmic contacts [13].

Although CNTFETs were extensively developed, CNTFET based IR detectors are not well understood, since high performance CNTFETs functioning as switches may not perform well as IR detectors. They require different characteristics: CNTFETs working as switches need high switching speed, low subthreshold slope, and high transconductance, while IR detectors require low noise, fast response, and large effective absorption area. In addition, although the theory of planar contact between metals and traditional semiconductors was fully developed and understood, it cannot be applied to 1D structures due to their unique characteristics, which arise from quantum confinement. That is to say, the behavior of CNT based photodetectors may differ from traditional photovoltaic devices even thought they share similar structures. Therefore, IR detectors using CNTFETs need to be investigated to understand their working principles so as to optimize their performance.

CNTFET based IR detectors have been fabricated to investigate their photoconductivity by modulating the Fermi energy of CNT though silicon back-gates [41] [42], as illustrated in Figure 3.1. In this configuration, a semiconductor CNT contacts two metal electrodes on a heavily doped Si/SiO₂ substrate. The metals serve as source and drain electrodes, while the conducting substrate acts as a gate terminal, which is used to control the Schottky barriers by modulating the Fermi level of the CNT. However, these CNTFETs focused on exploring the physics of the CNTs, rather than concentrating on optimizing performance of CNT photon-detectors. In this chapter, optimizing the design and performance of CNTFET based IR detectors will be discussed.

We have already studied the performance of CNT based Schottky photodiodes in the previous chapter. However, in order to optimize the design and performance of CNTFET based detectors, three questions remain to be answered: 1) how the Vg affects the detector performance; 2) whether an asymmetric metal structure is suitable for CNTFETs; 3) what

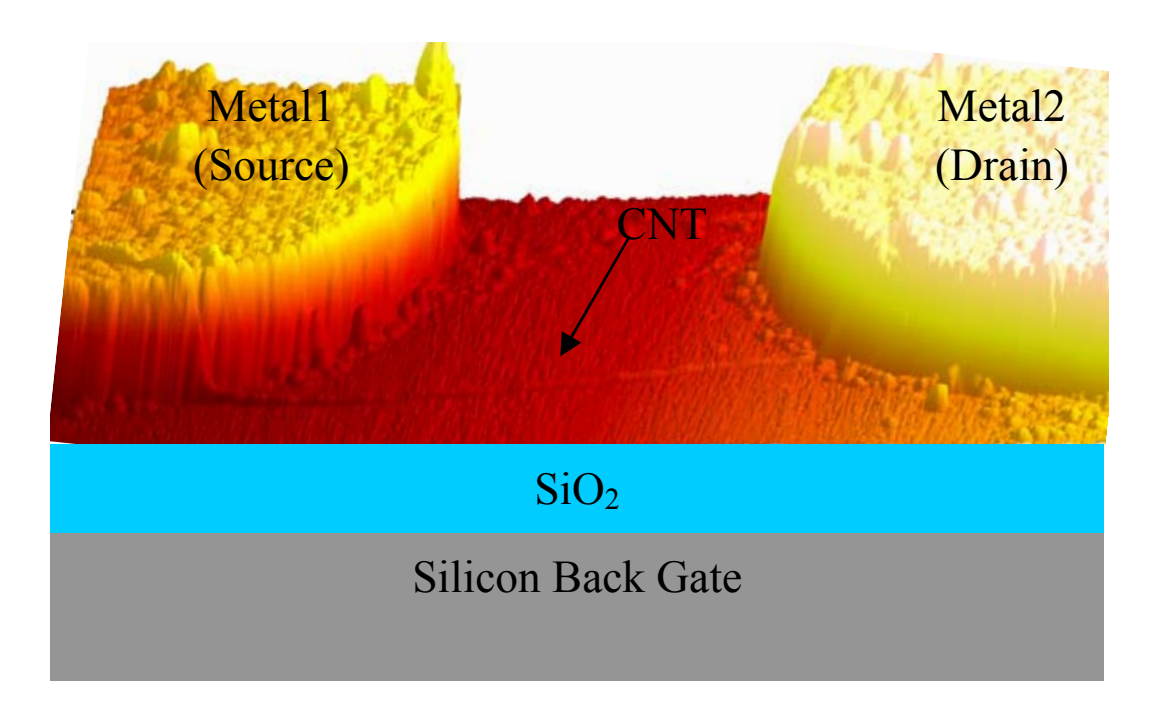


Figure 3.1: An AFM image of the structure of CNTFET with a silicon back-gate.

is the optimal gate structure. Five different CNTFETs will be introduced in the following sections to find the answers to these questions. A back-gate CNTFET with Au-CNT-Au structure is introduced first, and its photo-responses are compared with back-gate CNTFETs with Ag-CNT-Ag configuration, so as to understand the roles of metal workfunctions and Vg in determining the detector performance. Asymmetric back-gate CNTFET with Ag-CNT-Au structure was then investigated, and both high photocurrent and open circuit voltage (Voc) were obtained. The back-gate structure, albeit simple, provides valuable information to guide the design of CNTFET based IR detectors. However, the back-gate structure cannot be applied to a large scale detector array, since its component devices will be modulated simultaneously. Individual gate is required for each single detector. A middle-gate CNTFET consisting of an Al/Al₂O₃ gate between source and drain was examined, showing the capability to control detectors independently. Eventually, an asymmetric multi-gate CNTFET was investigated to find the optimal gate structure. The multi-gate CNTFET comprise four

different gates: back-gate, gates for source and drain, and middle-gates for the CNT channel.

3.1 Back-gate Au-CNT-Au Transistor

Figure 3.2 shows the configuration of a back-gate Au-CNT-Au CNTFET. The fabrication process of this device began with making two Au electrodes with gap of around 1 μm using photolithography, thermal evaporation, and lift-off on top of a heavily doped Si substrate covered with 200 nm SiO₂. It was followed by dropping a droplet of CNT suspension between the electrodes that connect to the DEP system [27]. An individual CNT can be deposited between the electrodes by adjusting the suspension concentration, assisted by an AFM manipulation system [28] [29].

Conductance of the CNTFET was varied by applying Vg to the back-gate, which changes the tunneling probability through the Schottky barriers. The I-V characteristic of a CNT-FET using CNT with three different Vg are shown in Figure 3.3(a). A weak parabolic I-V characteristic was observed without Vg, because of two small Schottky barriers reversely connecting between the source and drain. When no Vg was applied, the Fermi energy of Au is close to that of CNT (~5.0 eV) [43]. By applying different Vg to the gate, p-type transistor characteristics were observed: positive Vg reduced the conductance, while negative Vg increased the conductance, as shown in Figure 3.3(b). An exceptional characteristic is that negative Vg caused linear I-V relationship, while positive Vg resulted in strong parabolic I-V characteristics. In 1D barriers, thermally assist tunneling dominates the carrier injection [44], therefore the linear I-V characteristics indicated an extreme thin or zero barrier, while strong parabolic I-V characteristics were caused by a strong barrier.

The photo-responses of the CNTFET were measured by focusing an IR laser with 830 nm

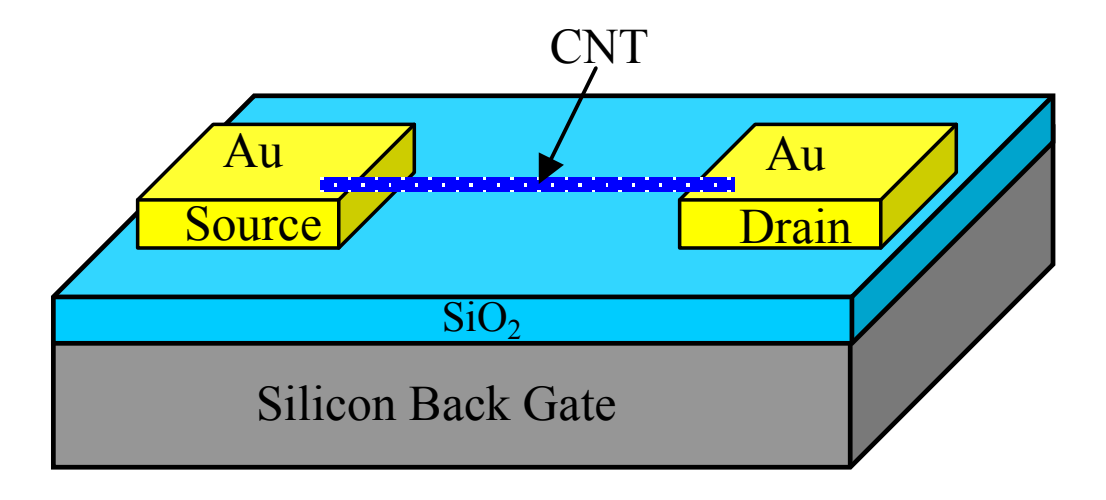


Figure 3.2: Structure of the back-gate Au-CNT-Au CNTFET.

wavelength and a maximum power of 50 mW, on one barrier. A more detailed introduction to the testing system can be found in [31]. The transfer characteristics of the device at zero bias with IR laser off and on (50 mW) are shown in Figure 3.4(a). When the IR source was off, the conductance has similar correspondence to Vg as in Figure 3.4(b). However, extremely different transfer characteristics were observed when the IR laser was turned on. This indicated that excess carriers were generated by IR illumination, and contributed to current flow. The current difference between IR on and off status was denoted as photocurrent (Iphoto) in the following discussion. The relationship between Vg and Iphoto is shown in Figure 3.4(b). The Iphoto at zero Vg was approximately -17.5 pA. The Iphoto was positive and enhanced by increasing positive Vg, while it became negative when negative Vg was applied. This can be explained by the band diagram shown in Figure 3.4(b), and the energy level alignment shown in Figure 3.5 (CNT is p type material in the air [45]). When positive Vg was applied, the Fermi energy of the CNT became lower than that of Au. In contrast, sufficient negative Vg increased the Fermi energy of the CNT beyond that of Au. As a result, the direction of the Schottky barrier changed, which inversed the sign of Iphoto.

The magnitude of Iphoto was enhanced by increasing the magnitude of both positive and

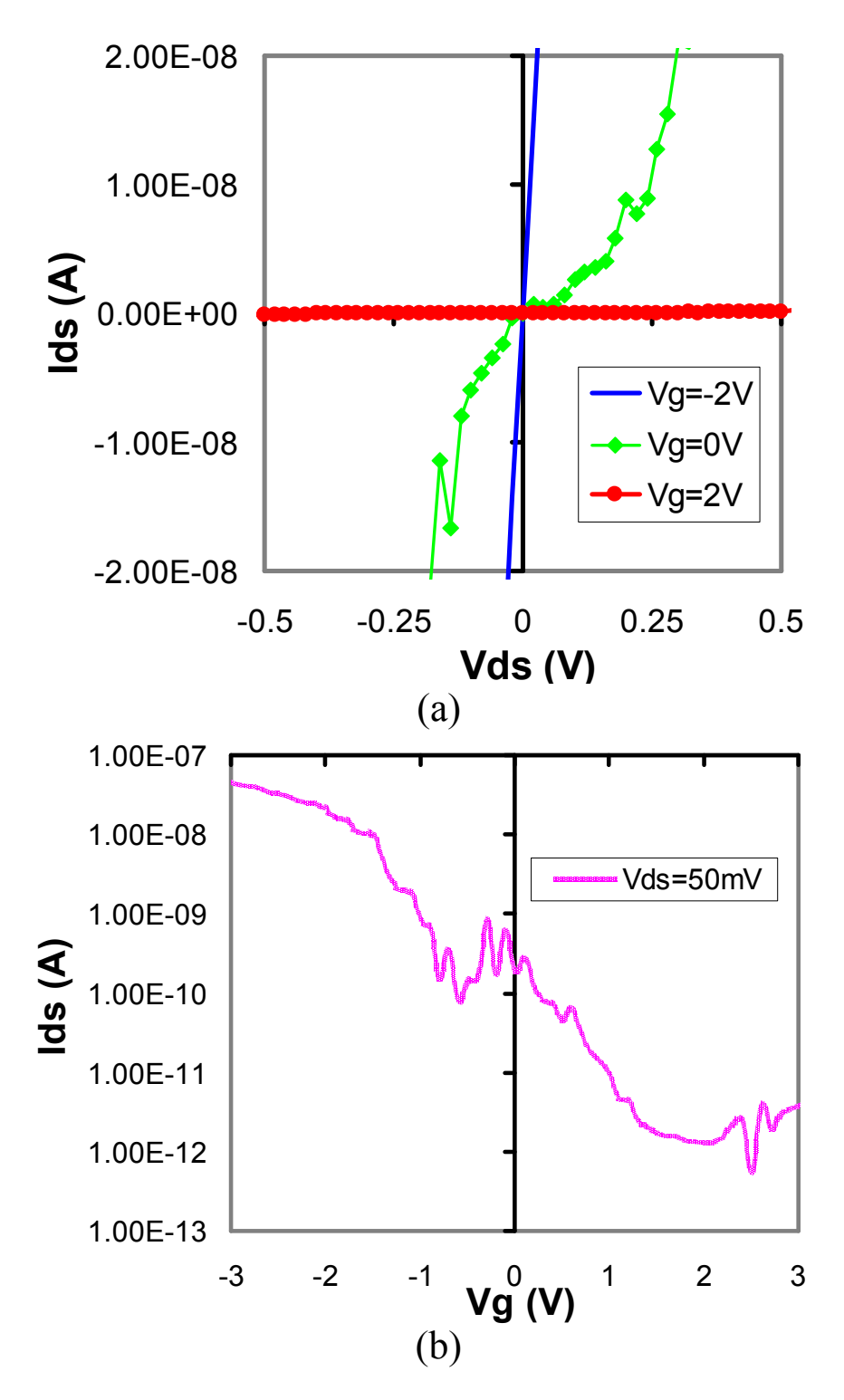


Figure 3.3: (a) The I-V characteristics of the CNTFET. (b) Transfer characteristics of the CNTFET at Vds=50~mV.

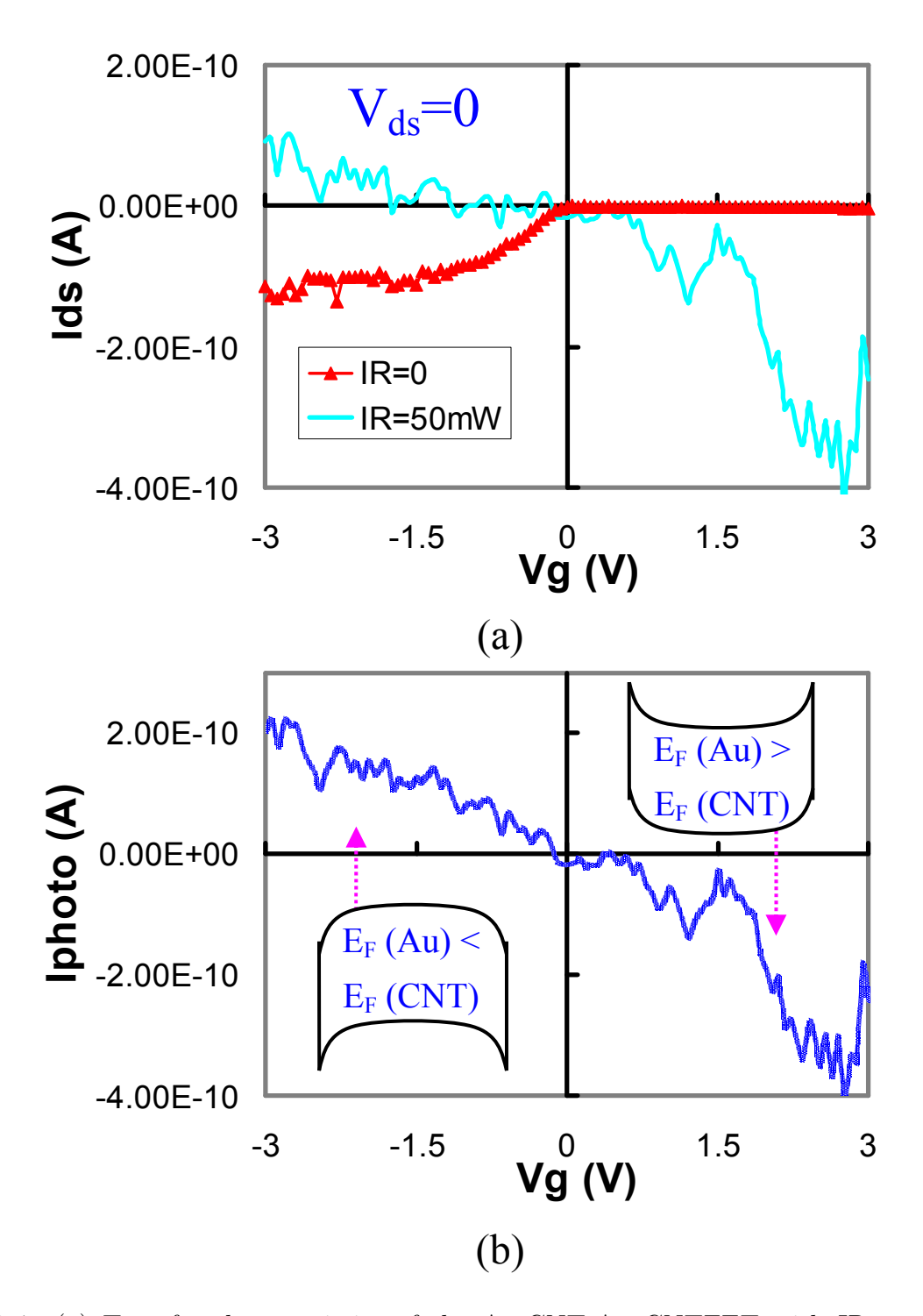


Figure 3.4: (a) Transfer characteristics of the Au-CNT-Au CNTFET with IR source off (IR=0) and on $(IR=50 \mathrm{mW})$ at zero bias. (b) The relationship between gate voltage and photocurrent and corresponding band diagrams at negative and positive gate voltages.

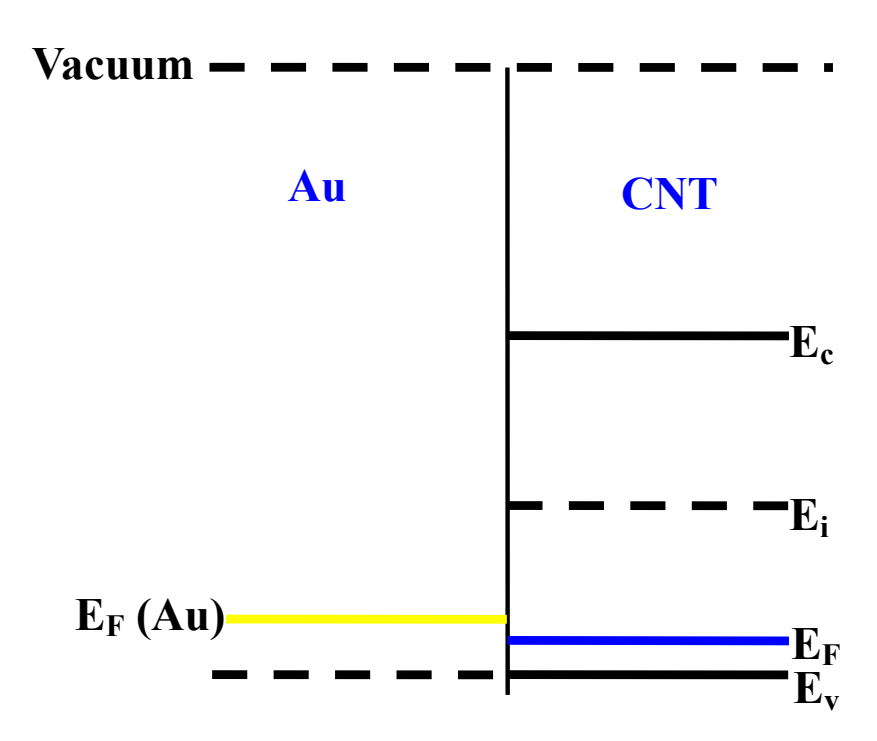


Figure 3.5: The energy levels of Au and CNT.

negative Vg. However, the Iphoto to dark current ratio (denoted as ON/OFF ratio in the following discussion) at positive Vg was much higher than that at negative Vg, as explained in the following discussion.

For negative Vg, increasing Vg caused higher built-in potential and p-doping levels (assume Au and CNT have the same Fermi energy). The additional p-doping may turn the CNT into a degenerated p-doped semiconductor. This is supported by the linear I-V characteristics at negative Vg (Figure 3.3). The bias-dependent Iphoto values at Vg=-0.5 V are shown in Figure 3.6(a). One particular feature is that the current decreased with IR illumination, which was caused by the contradiction of the separated photo-generated carriers and injection carriers. Higher bias decreased carrier transit time, leading to photoconductive gain, resulting in higher Iphoto.

For positive Vg, larger bias resulted in higher built-in potential but lower p-doping level.

Note that the ON/OFF ratio at positive Vg was greatly improved due to the suppression of dark current and enhancement of Iphoto. The bias dependent measurement at Vg=2 V (Figure 3.6(b)), which clearly showed the photovoltaic characteristics. At Vds=0.12 V, Iphoto was equal to the current produced by the bias, resulting in zero net current. This bias is the open circuit voltage, denoted as Voc. Simulation has shown that depletion width varies exponentially with inverse doping [15] and built-in potential [46]. Therefore, the Iphoto at positive Vg was increased by the widened depletion width, which enlarged the effective absorption area.

3.2 Back-gate Ag-CNT-Ag Transistor

It was demonstrated that applying proper voltages to the back-gate can improve the performance of CNT detectors in Au-CNT-Au structure. In order to achieve that, both high built-in potential and low doping level are desired. However, the built-in potential in the Au-CNT-Au structure is limited by the workfunction of Au, which is close to that of CNTs. In addition, the barrier height using Au is small because the majority is holes, as shown in Figure 3.5. In 3D bulk material, the Schottky barrier properties are dominated by the Fermi level pining effect, which makes metal workfunction insignificant in determining Schottky barriers, but this effect is trivial in 1D structures [47]. Therefore, using a metal with lower workfunction (Ag=4.2-4.5 eV) [48] as electrode can form a higher built-in potential and barrier height, as shown in Figure 3.7.

A back-gate CNTFET using Ag electrodes was fabricated to investigate the role of metal workfunction. The fabrication process was the same as for the Au-CNT-Au CNTFET, but depositing Ag instead of Au. Figure 3.8(a) shows the electrical characteristics of the Ag-

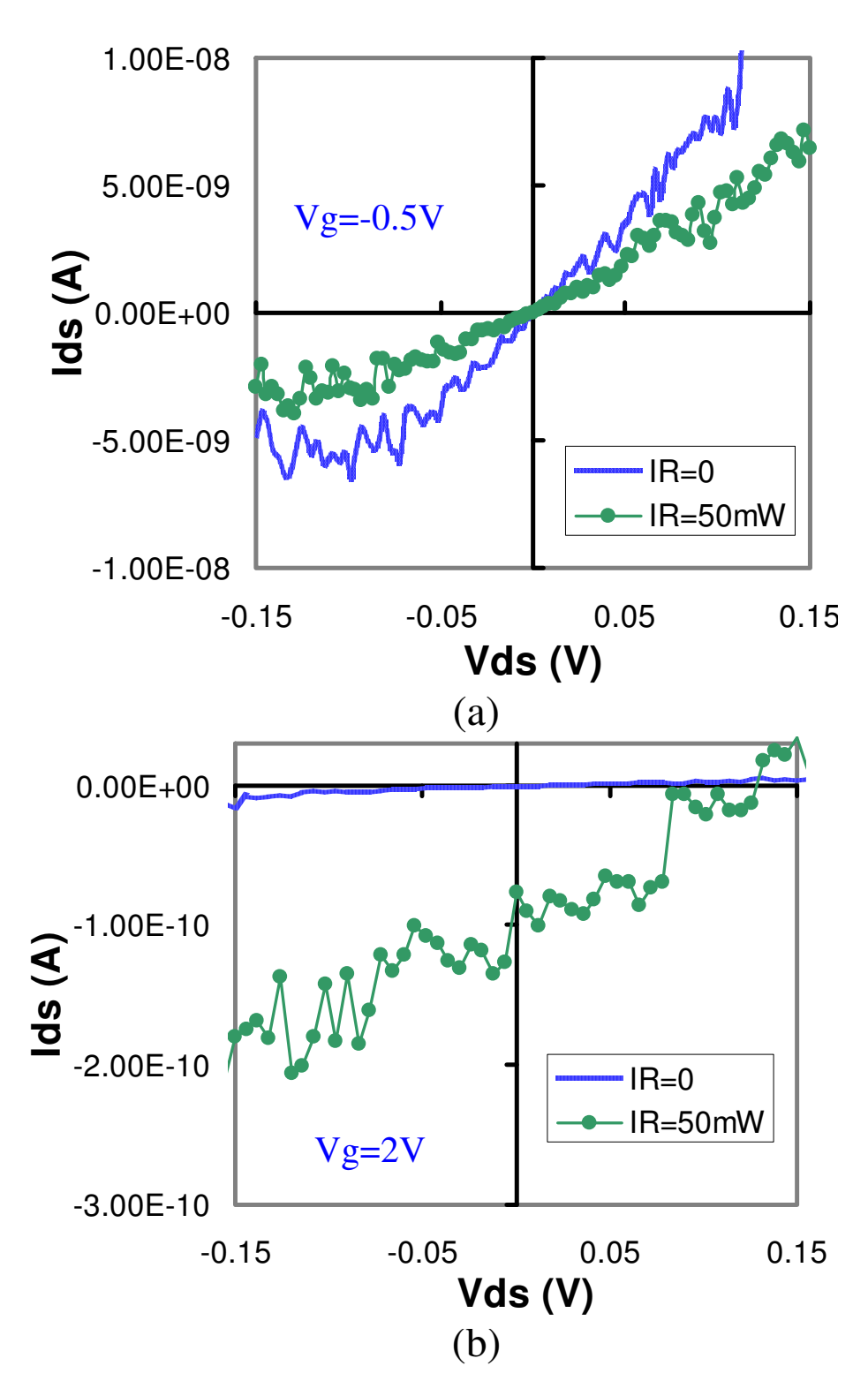


Figure 3.6: The bias-dependent measurement of the Au-CNT-Au CNTFET with IR=0 and IR=50 mW at (a) Vg=-0.5V and (b)Vg=2V.

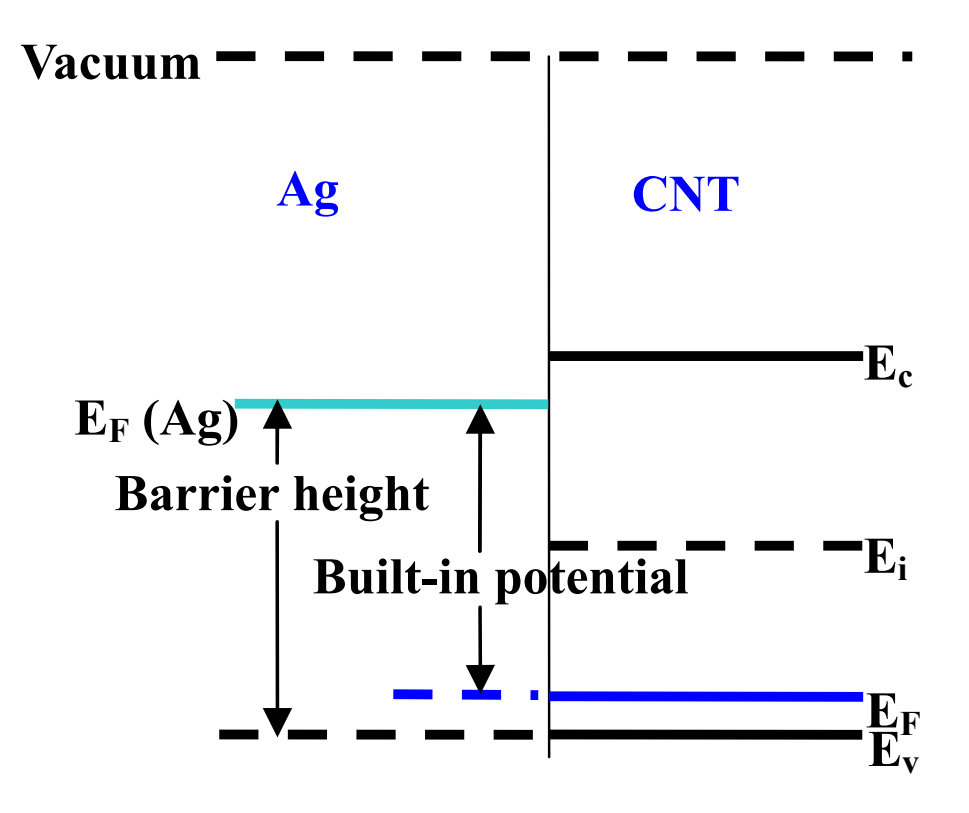


Figure 3.7: The energy levels of Ag and CNT.

CNT-Ag CNTFET with an individual CNT of 1.4 nm diameter. P-type transistor transfer characteristics were also observed in this device. In addition, negative Vg caused linear I-V characteristics, while positive Vg resulted in current rectifying. However, one distinct feature was that the conductance was ~1-2 orders of magnitude smaller than in the Au-CNT-Au CNTFET, resulting in smaller dark current. This can be explained by a decreased tunneling probability through stronger Schottky barriers between Ag and CNT. The dark current of this detector was changed corresponding to the conductance change: increased by negative Vg, but decreased by positive Vg, as shown in Figure 3.8(b).

The relation between Vg and Iphoto is shown in Figure 3.9(a). Positive Vg not only reduced dark current, but also increased Iphoto, resulting in enhanced ON/OFF ratio. The Voc at zero Vg was small; however, a Voc of 0.3 V was observed when a Vg of 3 V was applied

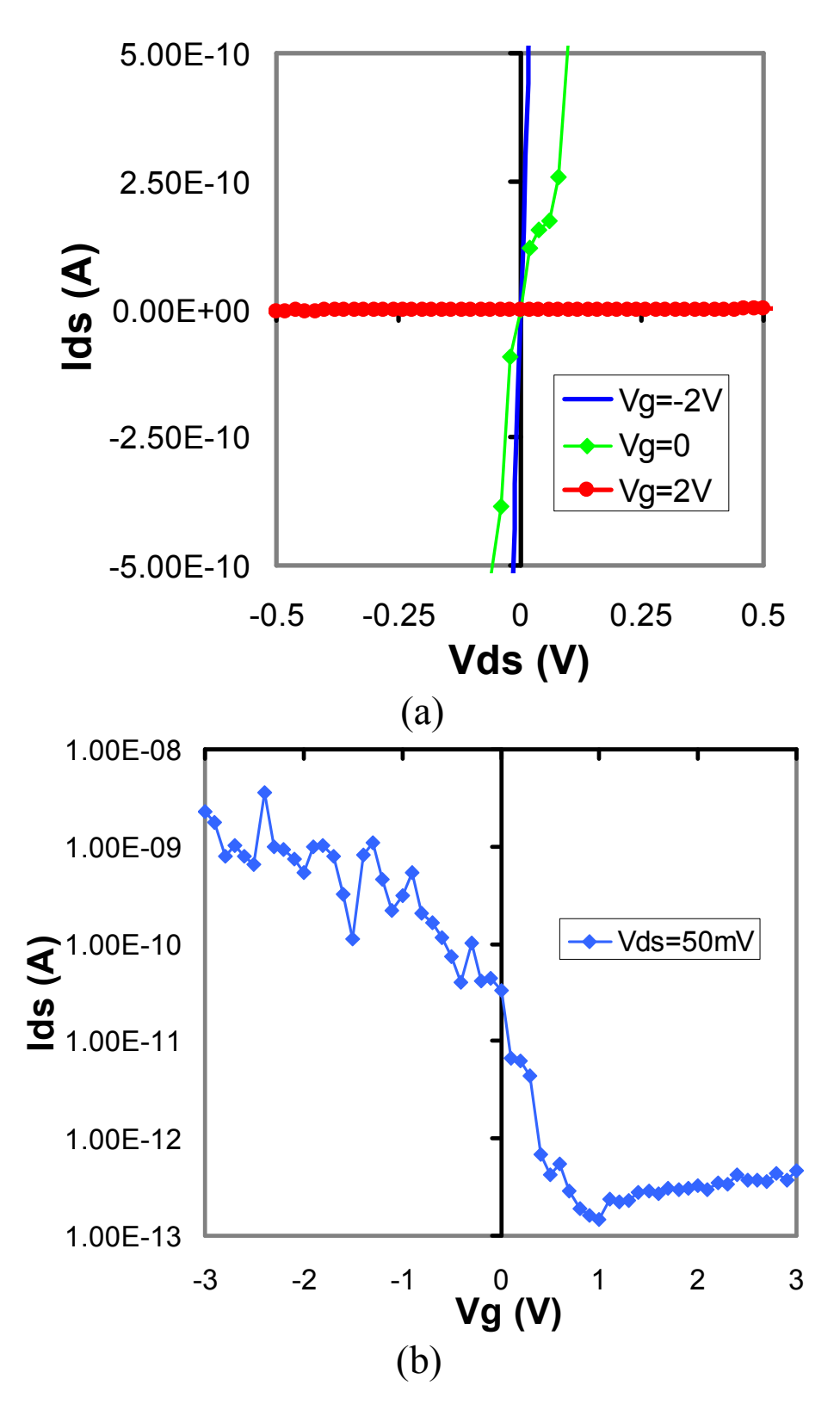


Figure 3.8: (a) I-V characteristics of the CNTFET. (b) Transfer characteristics of the CNTFET at Vds=50~mV.

to the back-gate with 50 mW IR illumination (Figure 3.9(b)). Bias-dependent measurement with four different power outputs was conducted. Typical photovoltaic characteristics were measured: Iphoto was linearly proportional to the output power, while Voc was exponentially proportional to the output power.

One particular feature is that the highest Iphoto of the Ag-CNT-Ag CNTFET at IR=50 mW $(5\times10^{-11} \text{ A})$ was smaller than that of the Au-CNT-Au CNTFET $(1\times10^{-10} \text{ A})$ in the bias-dependent measurements, but Voc was much higher. This can be explained by the symmetric metal structure: a higher built-in potential in Ag-CNT contacts resulted in wider absorption width (depletion width) and lower dark current, but the separated electrons and holes at one barrier needed to tunnel through a wider barrier in order to contribute to Iphoto generation. The comparison between these two CNTFETs indicates that metal selection plays a vital role in determining detector performance. Ag has lower work function than Au, resulting in a higher built-in potential and barrier height in the metal-CNT contacts. As a result, a higher Voc was obtained in the back-gate Ag-CNT-Ag CNTFET.

3.3 Back-Gate Au-CNT-Ag Transistor

Electrostatic doping in two symmetric CNTFETs has been demonstrated in previous sections as an effective method to improve detector performance by depressing dark current and enhancing Iphoto with widened Schottky barriers. However, the symmetric structure depressed photocurrent generation, since the separated electrons and holes need to tunnel through a wide barrier before contributing to current flow. Motivated by this problem, a back-gate Au-CNT-Ag CNTFET was fabricated, as shown in Figure 3.10. CNT and Au form a quasi-ohmic contact, while CNT and Ag form a Schottky barrier. As a result, this detec-

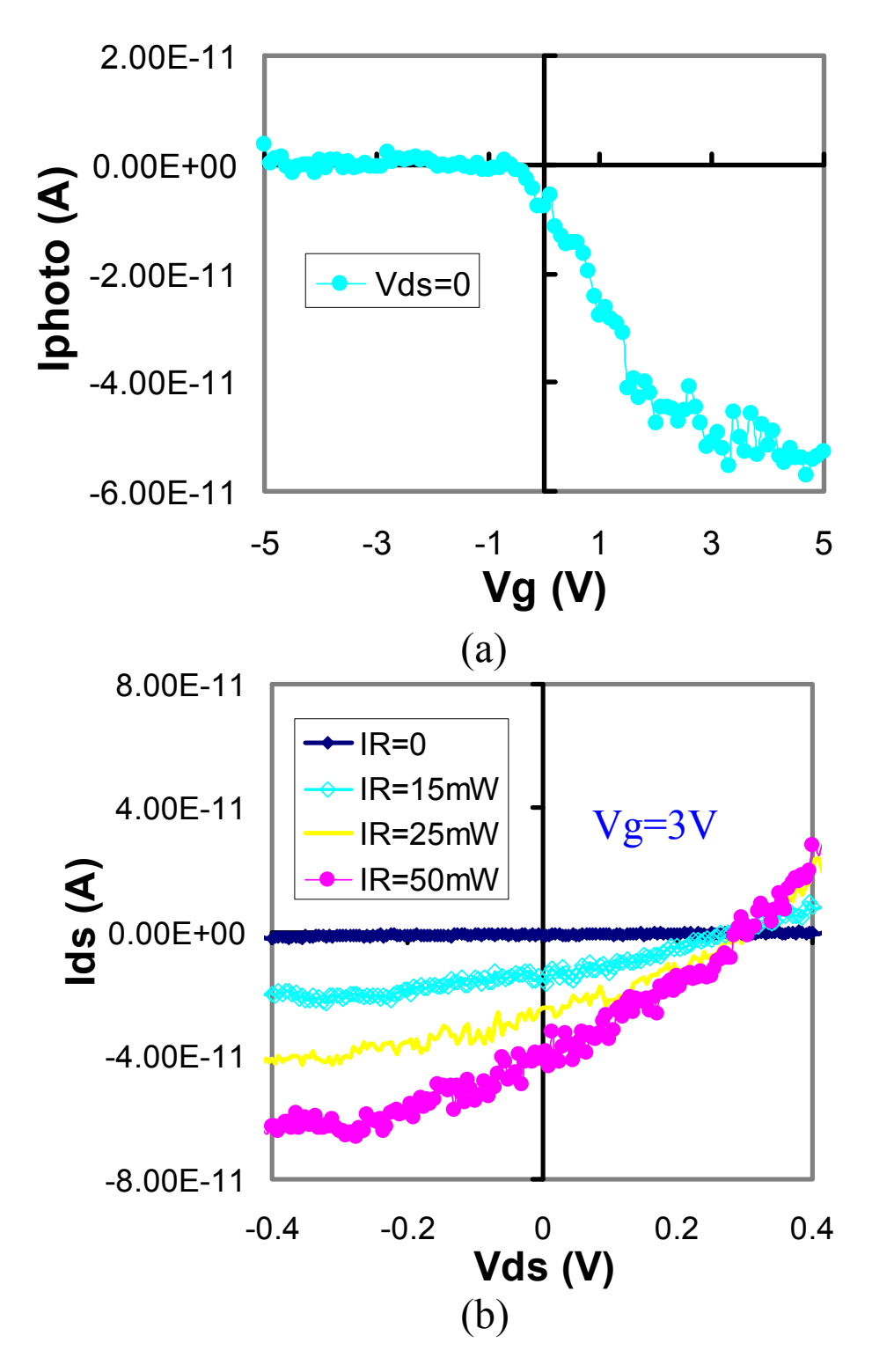


Figure 3.9: (a) The relation between gate voltage and photocurrent of the Ag-CNT-Ag CNTFET. (b) Bias dependent measurement with IR at four different output powers at Vg=3~V.

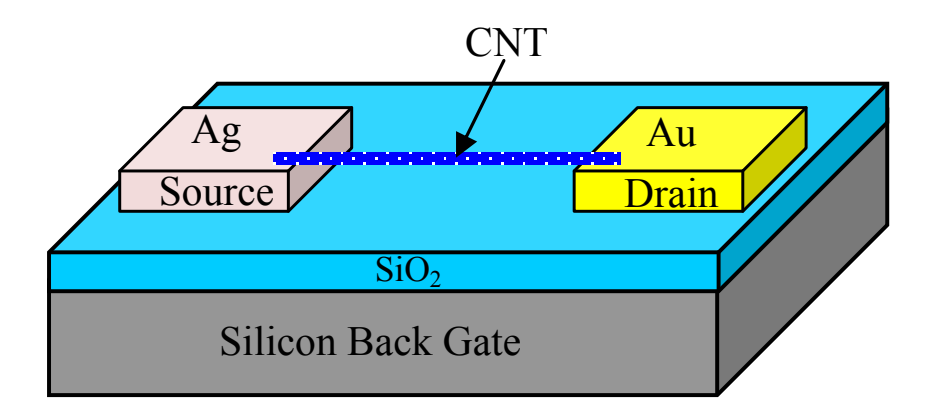


Figure 3.10: Structure of the back-gate Au-CNT-Ag CNTFET.

tor becomes a Schottky diode. By irradiating the device with IR photons, photo-response can be improved, since the separated electrons and holes do not need to pass through as a strong barrier (Ag-CNT) as in the symmetric structure. The fabrication process began with making an Au electrode, followed by fabricating an Ag electrode with a gap of 1 μm to the Au electrode after fine alignment.

Figure 3.11(a) shows the transfer characteristics of the Au-CNT-Ag CNTFET with and without IR illumination. The dark current showed p-type transistor characteristics. Iphoto was highly improved with positive Vg, although no obvious improvement is apparent in Figure 3.11(b) due to the hysteresis effect [49]. By measuring the temporal photo-response, it is shown that the Iphoto was increased from 2×10^{-11} (Vg=0) to 1.2×10^{-9} A (Vg=8V) (Figure 3.11(b)). The highest Iphoto value, around 1 nA, was an order in magnitude higher than that of symmetric detectors.

A high ON/OFF ratio was obtained with positive Vg, thus the Voc was expected to improve. The bias dependent measurement with four different output powers at Vg=5 V is shown in Figure 3.12. This is a typical photovoltaic photo-response: negative bias enlarged the Schottky barrier that increased the Iphoto, while positive bias shrank the depletion region that suppressed the Iphoto. In addition, the Iphoto is proportional to the output

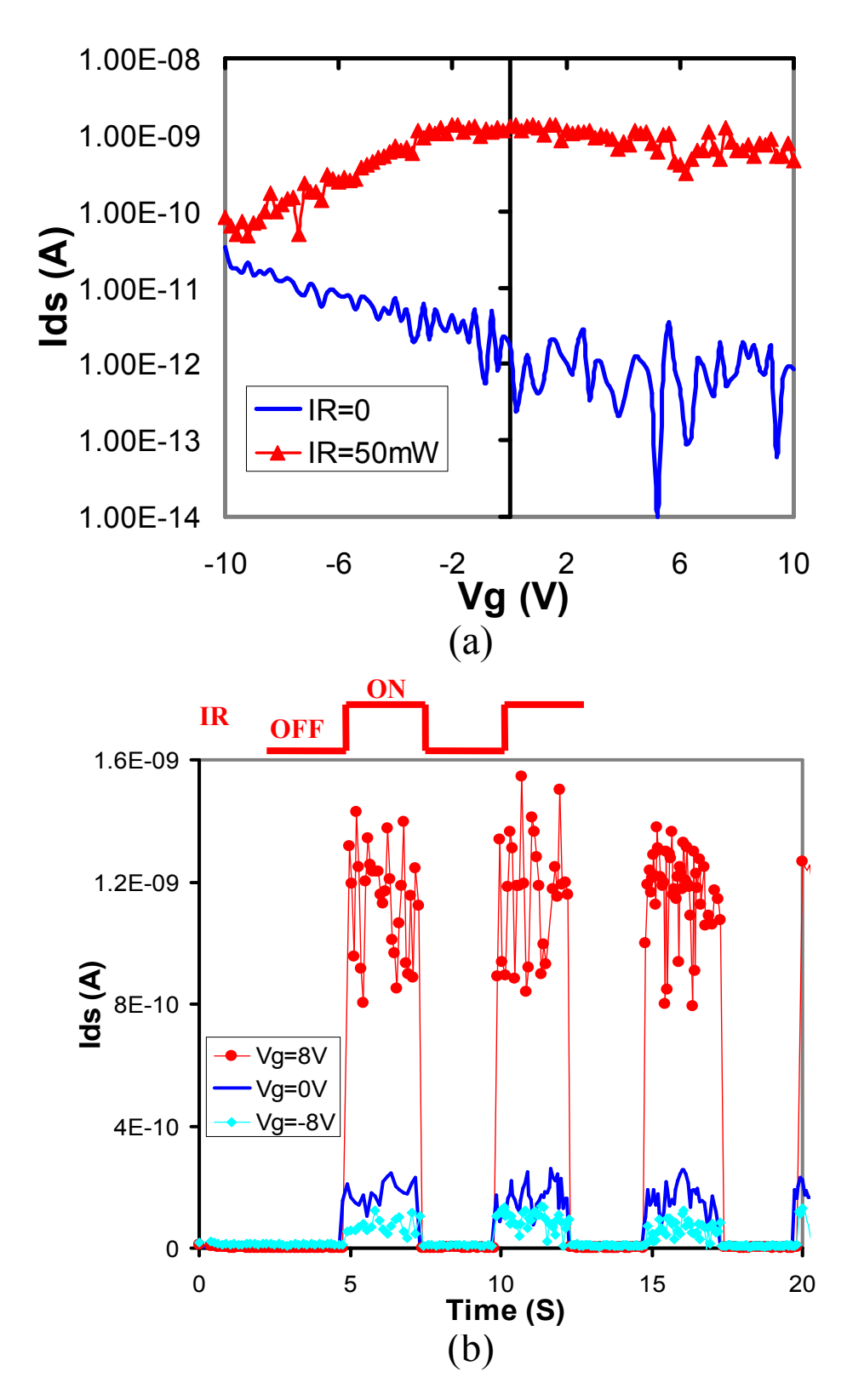


Figure 3.11: (a) Transfer characteristic of the asymmetric CNTFET with and without IR illumination. (b) Temporal photo-response with three different gate voltages at IR=50 mW.

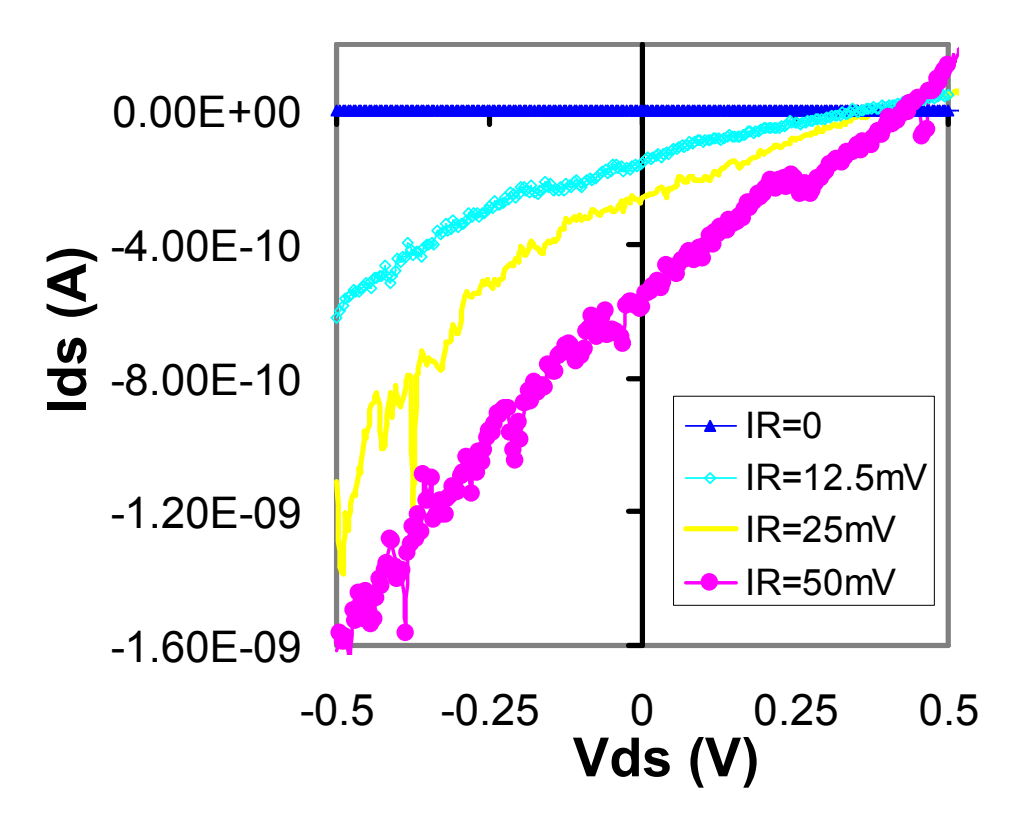


Figure 3.12: Bias dependent measurement with IR at four different output powers at Vg=5 V.

power, while the Voc is exponentially proportional to the output power. A Voc around 0.45 V was observed with 50 mW IR illumination, which is the highest Voc reported to date for an individual CNT based photo-detector. In contrast to the Iphoto, which is linearly dependent on the absorbed photons, the Voc is determined by the ON/OFF ratio. Therefore, although the detector absorbs small amounts of photons, Voc can still have a high value because the dark current can be extremely low in 1D structures due to the phonon scattering suppression and its nano-scale size.

3.4 Middle-Gate Transistor

Previous CNTFETs showed promising improvement by using a back-gate to modulate the Schottky barriers between metals and a CNT. However, back-gates cannot be used in large scale detector arrays, since all the devices will be modulated simultaneously. In this section, a middle-gate CNTFET, which has the capability to control each individual detector independently, will be introduced.

The structure of the middle-gate CNTFET and its AFM image are shown in Figure 3.13. A CNT bridges two Au electrodes as source and drain, and an Al/Al₂O₃ middle-gate is made underneath the CNT and partially couples it. The fabrication process begins with making two Au electrodes with an insulating gap of 2 μ m. A 1- μ m-wide Al electrode was fabricated in between the source and the drain by e-beam lithography, thermal evaporation, and lift-off. The sample was then bombarded by oxygen plasma, and a thin layer of Al₂O₃ grown on the Al as the insulator for the gate. The last step is to deposit a CNT to connect the two Au electrodes using the DEP deposition system and AFM manipulation system. Two inversely connecting p-n junctions (p-n-p) will be formed by applying proper Vg to the middle-gate, as shown by the band diagram in Figure 3.13(c).

The I-V characteristics of the middle-gate CNTFET with three different Vg are shown in Figure 3.14(a). P-type transistor characteristics were observed. Its conductance slightly increased with negative Vg, but decreased significantly with positive Vg. Current was linearly dependent on the bias without Vg, implying that ohmic contact is most probably between the CNT and Au. This was further verified by the no photo-response at Vg=0 V. The conductance increased with negative Vg may have resulted from the fringing field effect to the contacts. Positive Vg converts the middle of CNT into n-type material, forming a p-n-p structure, which can be considered as two inversely connected p-n junctions. Thus, diodelike I-V characteristics are shown at Vg= 2 V in Figure 3.14(a). The transfer characteristics at Vds=10 mV are shown in Figure 3.14(b) with a 200 mV/dec subthreshold slope.

The transfer characteristics, at Vds= 0 V with IR on and off, are shown in Figure 3.15(a),

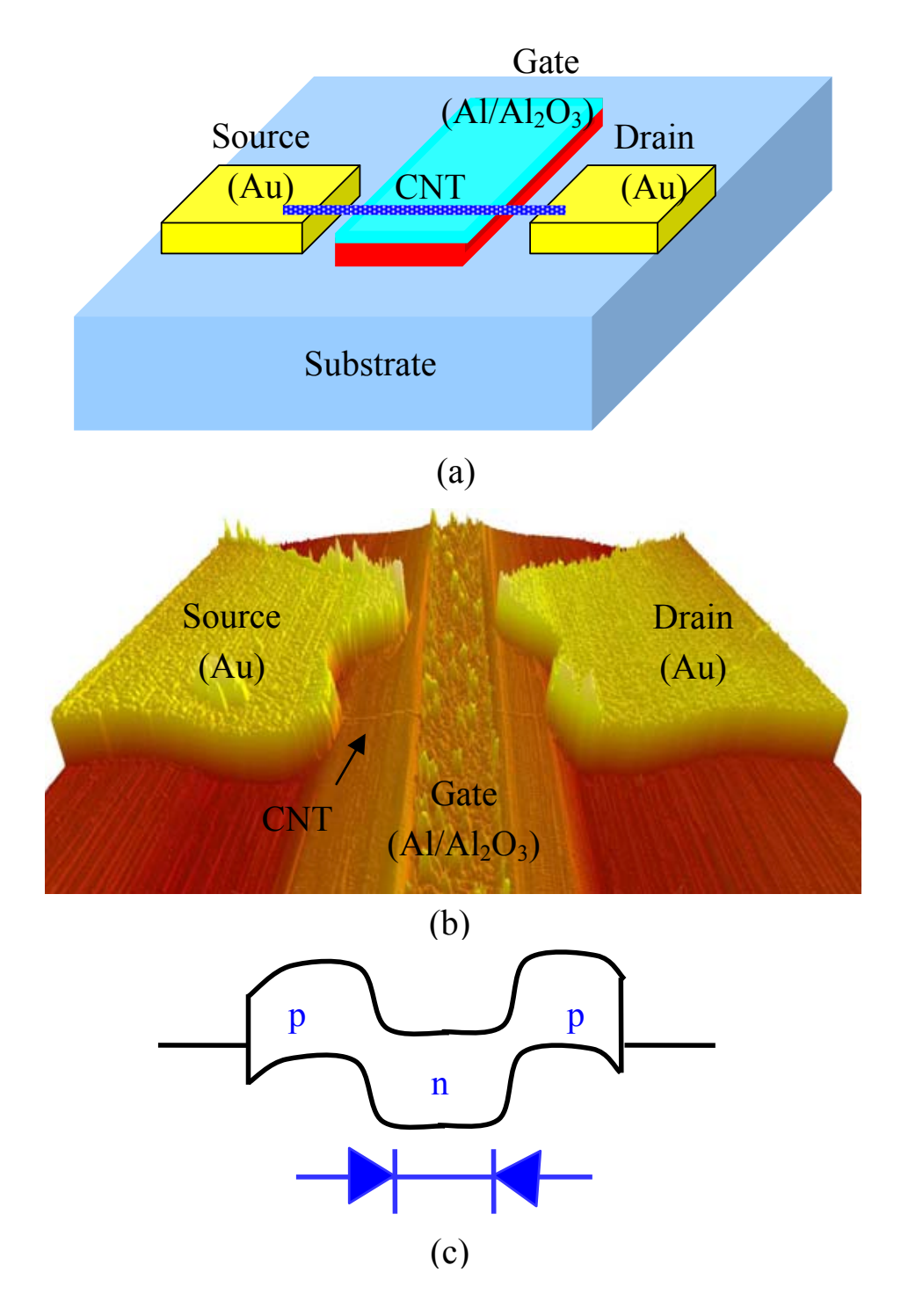


Figure 3.13: (a) Structure of the middle-gate CNTFET. (b) AFM image of the middle-gate CNTFET. (c) Band diagram of the working status of the middle-gate CNTFET.

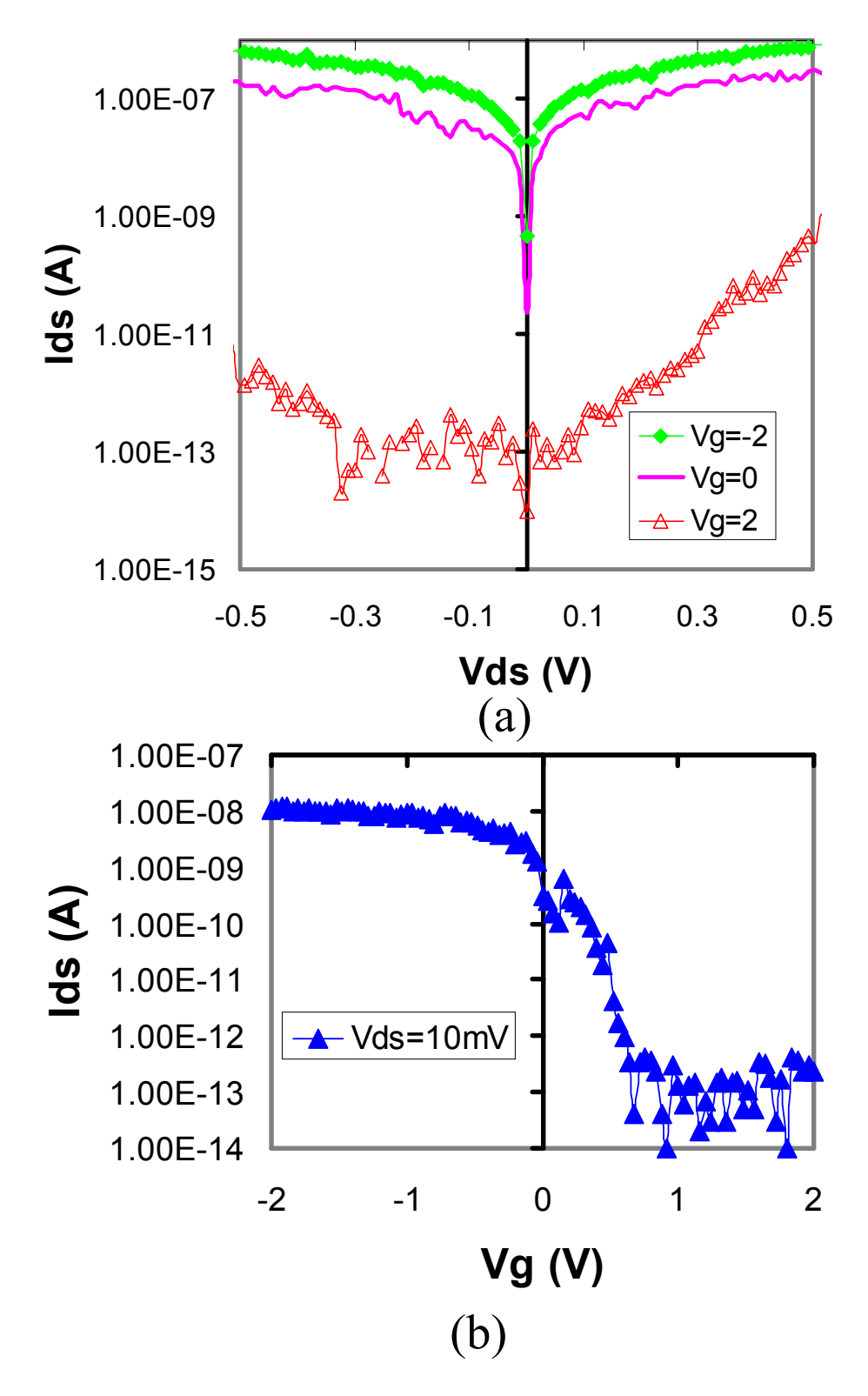


Figure 3.14: (a) I-V characteristics of the middle-gate CNTFET at three Vg in log-scale. (b) Transfer characteristics of the CNTFET with Vds=10 mV.

by sweeping the Vg from -2 V to 2 V. Dark current of the CNTFET decreased from 5×10^{-11} A (zero Vg) to 5×10^{-14} A with increasing positive Vg, since the electrons needed to tunnel through two p-n junctions in the CNT in order to contribute to the dark current. When 50 mW IR illuminated the CNT, similar transfer characteristics were observed with negative and small positive Vg, indicating no Iphoto was produced. Iphoto was observed with Vg values that are larger than 0.5 V, as shown in Figure 3.15(a). There was a sudden drop of the current signal at Vg of around -1 V, which may have been caused by defects in the CNT. The hysteresis phenomenon was observed in this device, and that is the reason why the sudden drops of the current with and without IR di not cause at the same Vg. In order to eliminate the effect of the hysteresis, we measured the temporal photo-response at fixed Vg by switching IR on and off at 0.2 Hz, as shown in Figure 3.15(b). No Iphoto was generated at Vg=0 V and Vg=-2 V, and the dark currents were large compared to those with positive Vg. When a 2 V Vg is applied, Iphoto with value of 1×10^{-11} A was generated, and an ON/OFF ratio of around two orders was observed.

Although the Iphoto is small, the Voc is determined by the ON/OFF ratio and operating temperature. We investigated the Voc by measuring bias dependent current at Vg=2 V, as shown in Figure 3.16. A typical photovoltaic photo-response was observed, and a 0.1 V Voc was obtained.

By introducing a middle-gate to the CNTFET, each individual detector in a large scale array can be controlled separately. However, this structure has some limitations that prevent optimal performance. First of all, the Iphoto generation is based on two inversely connecting p-n junctions, which is similar to the CNTFET with symmetric Schottky barriers. The detected Iphoto reflects the signal intensity difference between two junctions that are only $1 \ \mu m$ away from each other. What is more, although ohmic contact can be formed between

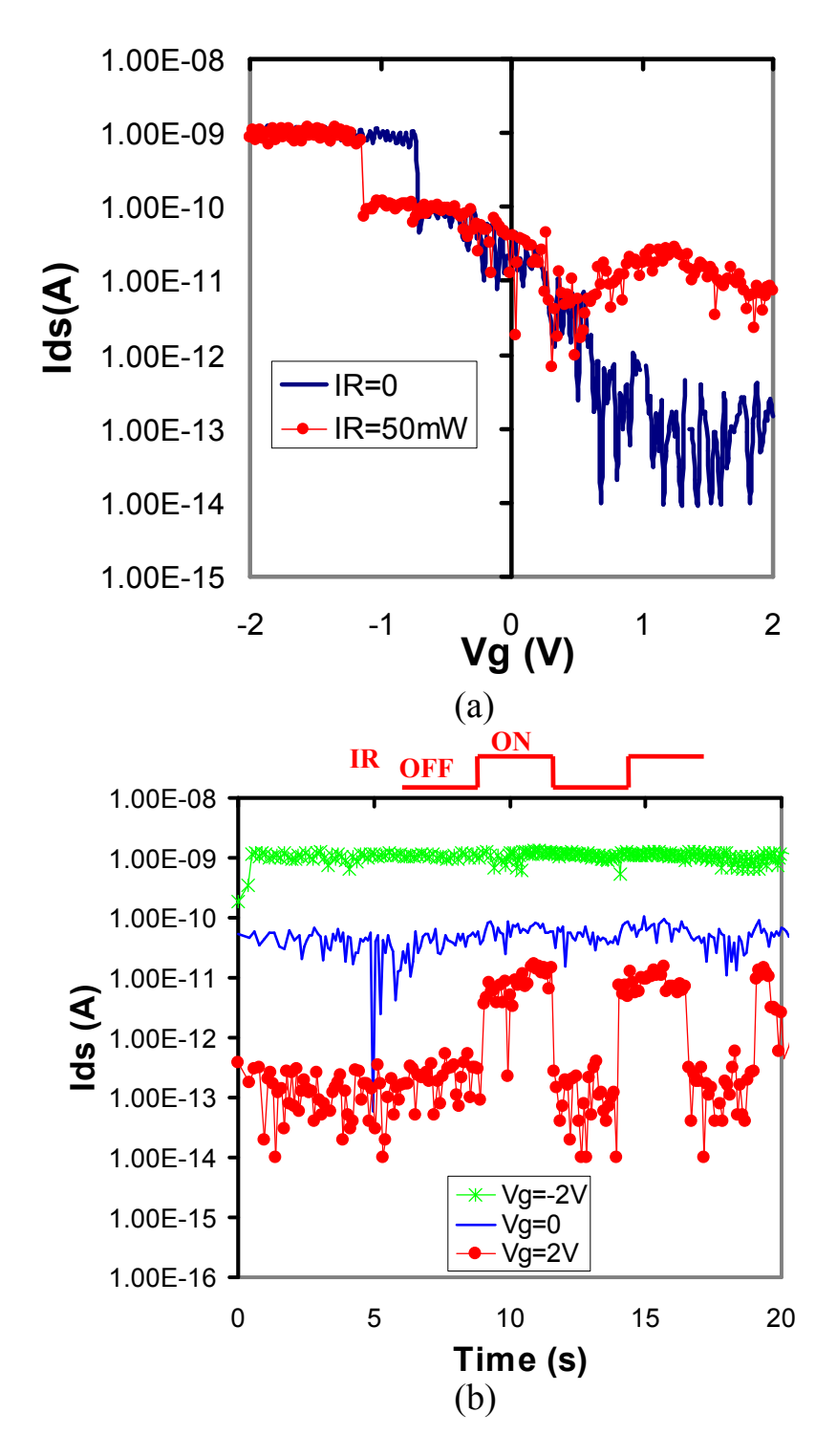


Figure 3.15: (a) Transfer characteristics of the middle-gate CNTFET with IR on and Off at zero bias. (b) Temporal photo-response measurement by switching IR on and off at 0.2 HZ.

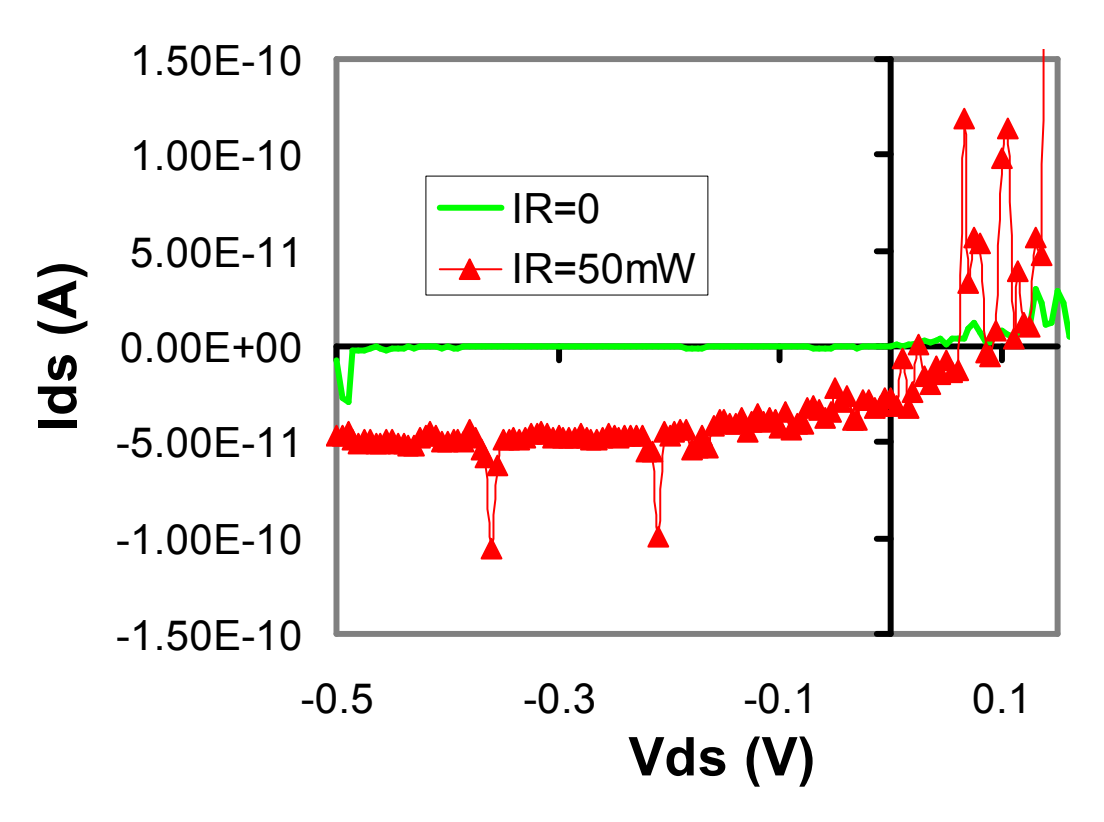


Figure 3.16: Bias dependent measurement with IR at two output powers at Vg=2 V.

a CNT and metals by selecting a proper metal, the fringe field from the middle-gate may produce a barrier that suppresses the generation of Iphoto.

3.5 Multi-Gate Transistor

In previous sections, we have demonstrated that both an asymmetric metal structure and electrostatic doping using a back-gate can improve the performance of the CNT detectors by manipulating the energy alignment between metals and a CNT, but a back-gate modulates all the detectors simultaneously. In order to control detectors independently, a middle-gate CNTFET was fabricated and investigated. However, all these CNTFETs have their limitations to perform optimally.

In order to optimize the design of the CNT detectors, an asymmetric multi-gate CNTFET

based IR detector was fabricated, integrating an asymmetric metal structure (Au-CNT-Al) with multiple gates, which allow controlling the Fermi energies at source, drain, and CNT channel independently. Examining gate structure dependent photo-responses may lead to an improved understanding and design of the photodetectors.

A multi-gate asymmetric CNTFET was fabricated with a back-gate and three pairs of side-gates that can locally dope the source, SWCNT channel, and drain, as shown in Figure 3.17. This device was an extension from the asymmetric (Al-CNT-Au) CNFEET with three pairs of Al side-gates located 400 nm to the SWCNT, denoted as Gate1, Gate2, and Gate3. Gate1 and Gate3 are used to modulate the Fermi level of source and drain independently. Gate2 is not only used to modulate the Fermi level of the SWCNT channel, but also blocks the fringing electrical field of Gate1 from Gate3 to guarantee the local doping capability.

Previous comparisons between symmetric and asymmetric CNTFET are based on different CNTs. A fabrication process was developed to compare electrical and optical characteristics of symmetric and asymmetric CNTFETs connecting to the same CNT. The fabrication process started with a heavily doped p-type single-crystal Si substrate, which was cleaned and coated with 200 nm of thermal SiO₂. The source-drain electrodes made of Au were fabricated by EBL, thermal evaporation, and liftoff, with a separation of 1000 nm, width of 500 nm, and thickness of 40 nm. SWCNT suspension was prepared by dispersing SWCNT powder in alcohol medium, followed by 10-15 minutes ultrasonication. Metallic SWCNTs were filtered out by a micro-dielectrophoresis chamber [32]. A droplet of SWCNT suspension was deposited between the source-drain electrodes, and dielectrophorisis force was generated by applying a sine wave (frequency of 10 kHZ and Vpp of 1 V) to trap a semiconductor SWCNT between the electrodes. An atomic force microscopy (AFM) manipulation system

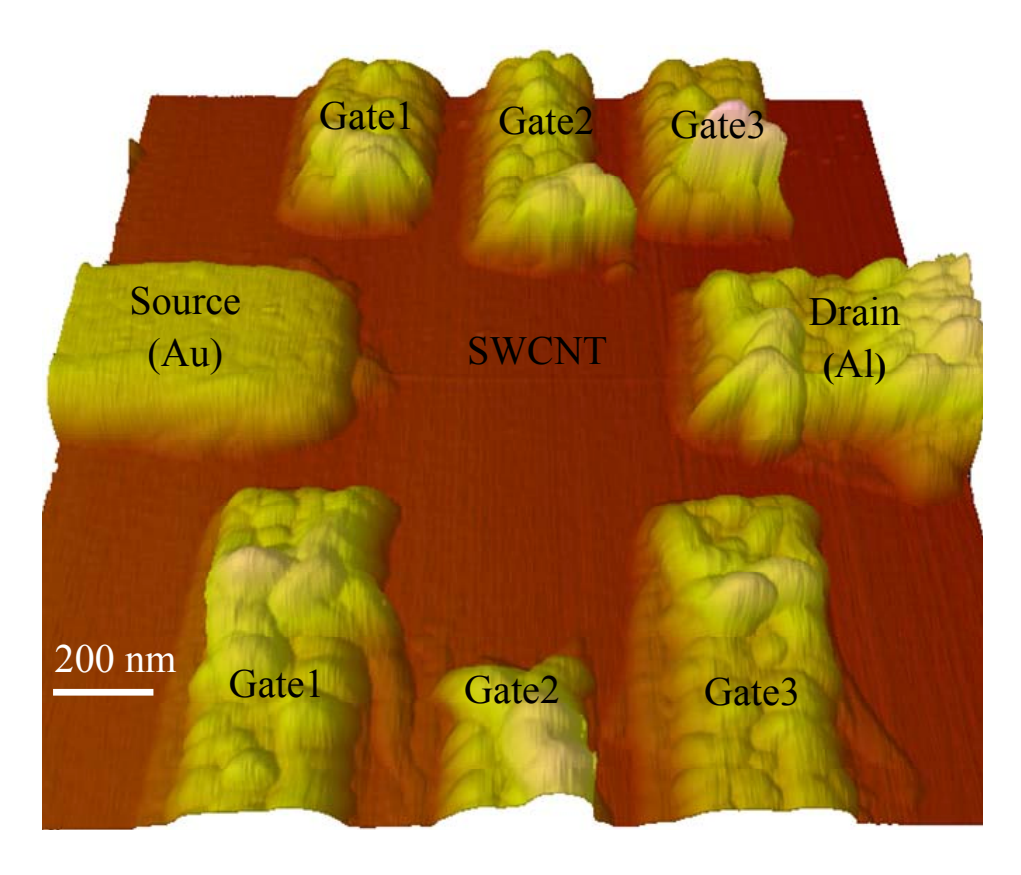


Figure 3.17: AFM image of the multi-gate asymmetric CNTFET with a back-gate and three pairs of side-gates that can locally modulate source (Gate1), SWCNT channel (Gate2), and drain (Gate3).

was utilized to guarantee the deposition of an individual SWCNT for each device [30]. Then the symmetric CNTFET was formed, and its I-V characteristics and photo-responses were measured. To convert this device into an asymmetric CNTFET, an Al electrode was used to cover one of the Au electrodes. The Al electrode was patterned by EBL and liftoff using 50 nm Al. To guarantee the formation of the asymmetric metal structure, the Al electrode was 200 nm extending towards the gap of two Au electrodes, as shown in the insets of Figure 3.18. Meanwhile, three pairs of side-gates are fabricated. The electrical and optical characteristics of the asymmetric CNTFET were recorded using the same experimental setup as in the symmetric CNTFET.

Electrical measurements were performed on the devices with source electrode maintained at ground potential using Agilent 4156C semiconductor parameter analyzer. Figure 3.18 shows the I-V characteristics of the symmetric and asymmetric CNTFETs at zero gate bias. The symmetric CNTFET forms two reversely connecting Schottky barriers at two contacts (inset of Figure 3.18), resulting in symmetric I-V characteristics. The I-V characteristics of asymmetric CNTFET exhibited current rectifying, with a high conductivity when forward biased and a low conductivity when reverse biased, due to the formation of two Schottky barriers in the same direction at two contacts.

Before the measurement of all gates, we firstly test the back-gate (Vgs) dependent photoresponses. An IR laser with wavelength of 830 nm and an output power of 50 mW was used to investigate the photo-responses of the CNT CNTFETs. The IR light is linearly polarized along the axis of the SWCNT. The laser was mounted on a high precision triple divide linear translation stage to align the laser spot onto the CNTFETs. Figure 3.19 shows the transfer characteristics of the symmetric CNTFET at zero bias with and without IR illuminating. The symmetric CNTFET exhibited typical unipolar p-type transfer characteristics at dark

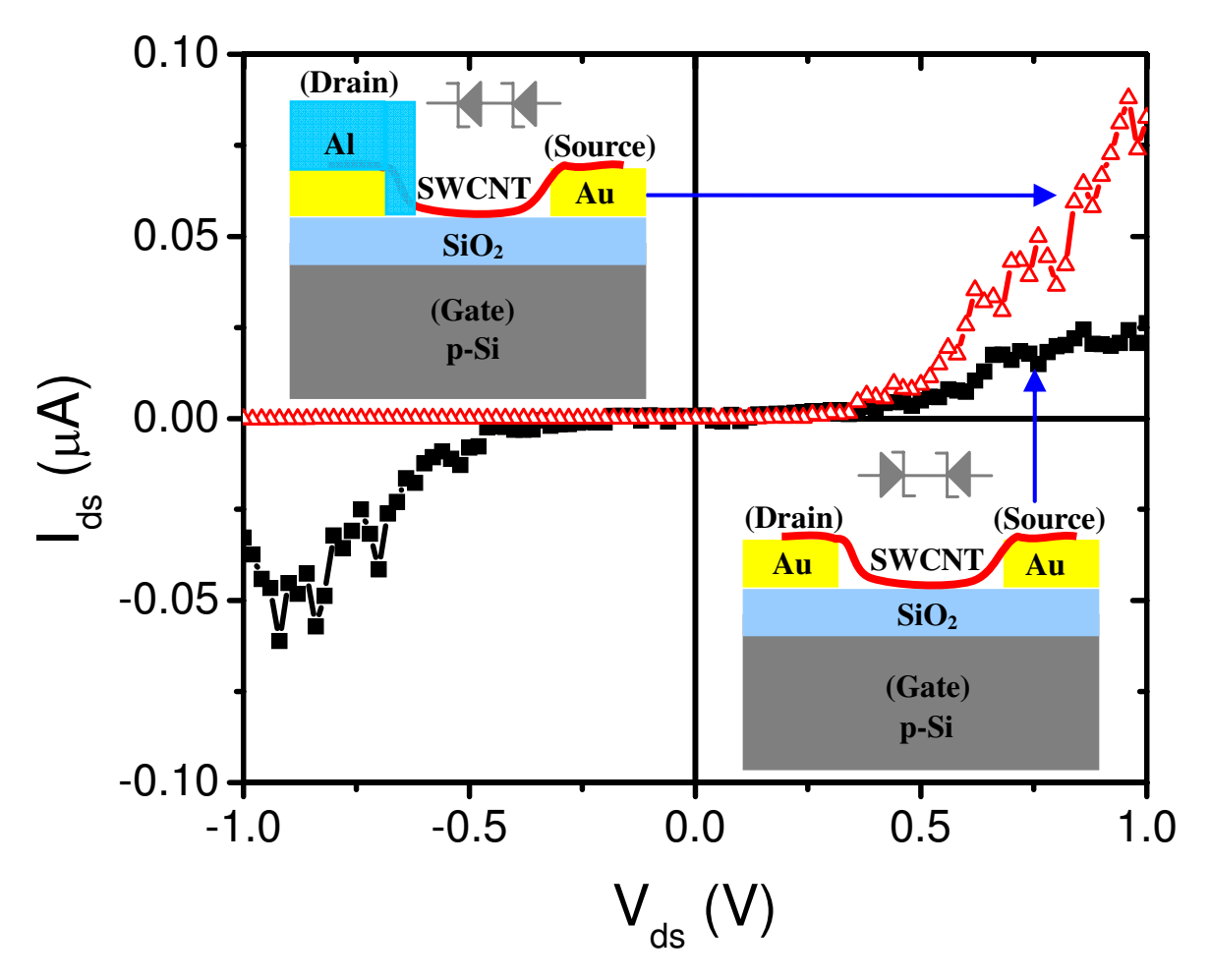


Figure 3.18: The I-V characteristics of the CNTFET with symmetric (Au-CNT-Au) and asymmetric (Al-CNT-Au) metal structures. The insets shows the cross-section of the CNT-FET.

(denoted as "IR OFF" in Figure 3.19): the dark current decreased from 60 pA (Vgs=-3 V) to 0.8 pA (Vgs = 3 V). Under IR illumination, denoted as "IR ON" in Figure 3.19, a different transfer characteristic was measured (blue curve), implying photo-generated electron and hole pairs were generated and separated by the Schottky barriers, and consequently contributed to the photocurrent. Photocurrent was positive with positive Vgs, while it changed polar with negative Vgs, as indicated by the arrows in Figure 3.19. This implied that Vgs changed the direction of Schottky barriers through electrostatic doping (band diagrams in Figure 3.19), because the workfunction of Au is only slightly bigger than that of SWCNT.

The asymmetric CNTFET at dark converted to an n-type transistor (Figure 3.20). The lowest dark current was obtained at Vgs = -3 V with a value of 0.02 pA. Upon IR illumination, the current signal exhibited p-type transfer characteristics: Figure 3.20 clearly shows current increased towards decreasing Vgs with IR ON. As a result, the photocurrent transfer curve of asymmetric CNTFET showed p-type characteristics, as shown in Figure 3.21. With regard to a transistor, this device can induce n- to p-type conversion by illuminating light onto the device due to change of the barrier width (w): negative gate bias increased the built-in potential between Al and SWCNT that enlarged the effective absorption region (w), as illustrated in the band diagrams of Figure 3.21. With regard to a photodetector, the sensitivity was enhanced 140 times according to the definition of sensitivity as the ratio of photocurrent to dark current. Because the lowest dark current of asymmetric CNTFET was 40 times smaller than symmetric CNTFET, and highest photocurrent was 3.5 times larger than symmetric CNTFET. In addition, photocurrent of the asymmetric CNTFET remained the same polar with Vgs in the range between -3 V to 3 V due to the large workfunction difference between Al and CNT.

Temporal photocurrent measurement was performed with different gate biases by switch-

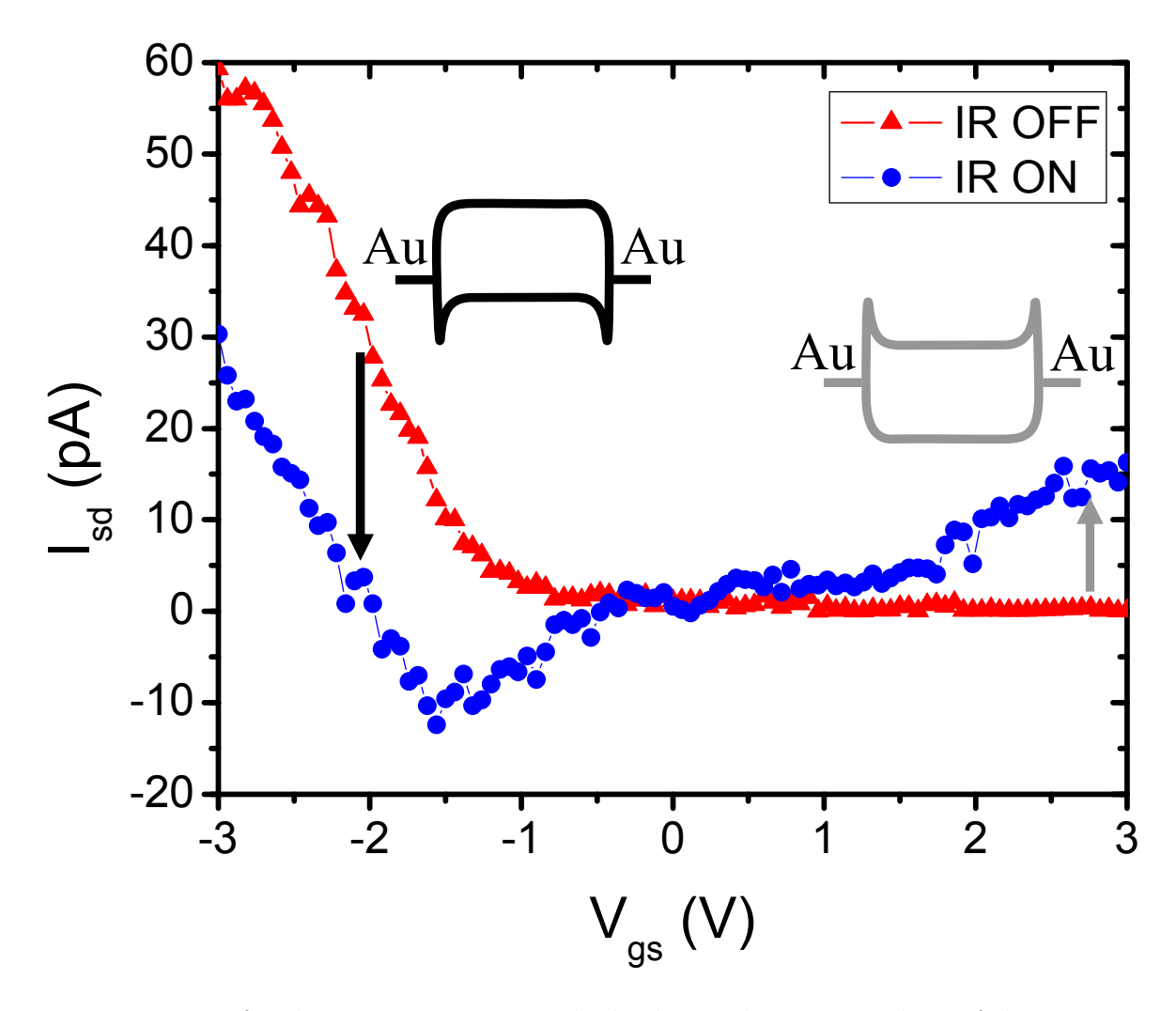


Figure 3.19: Transfer characteristics versus the back-gate bias at zero bias of the symmetric CNTFET with absence and presence of IR laser illumination (wavelength of 830 nm and output power of 50 mW) by sweeping the gate bias from -3 V to 3V. Two band diagrams show the Schottky barriers at negative and positive gate biases.

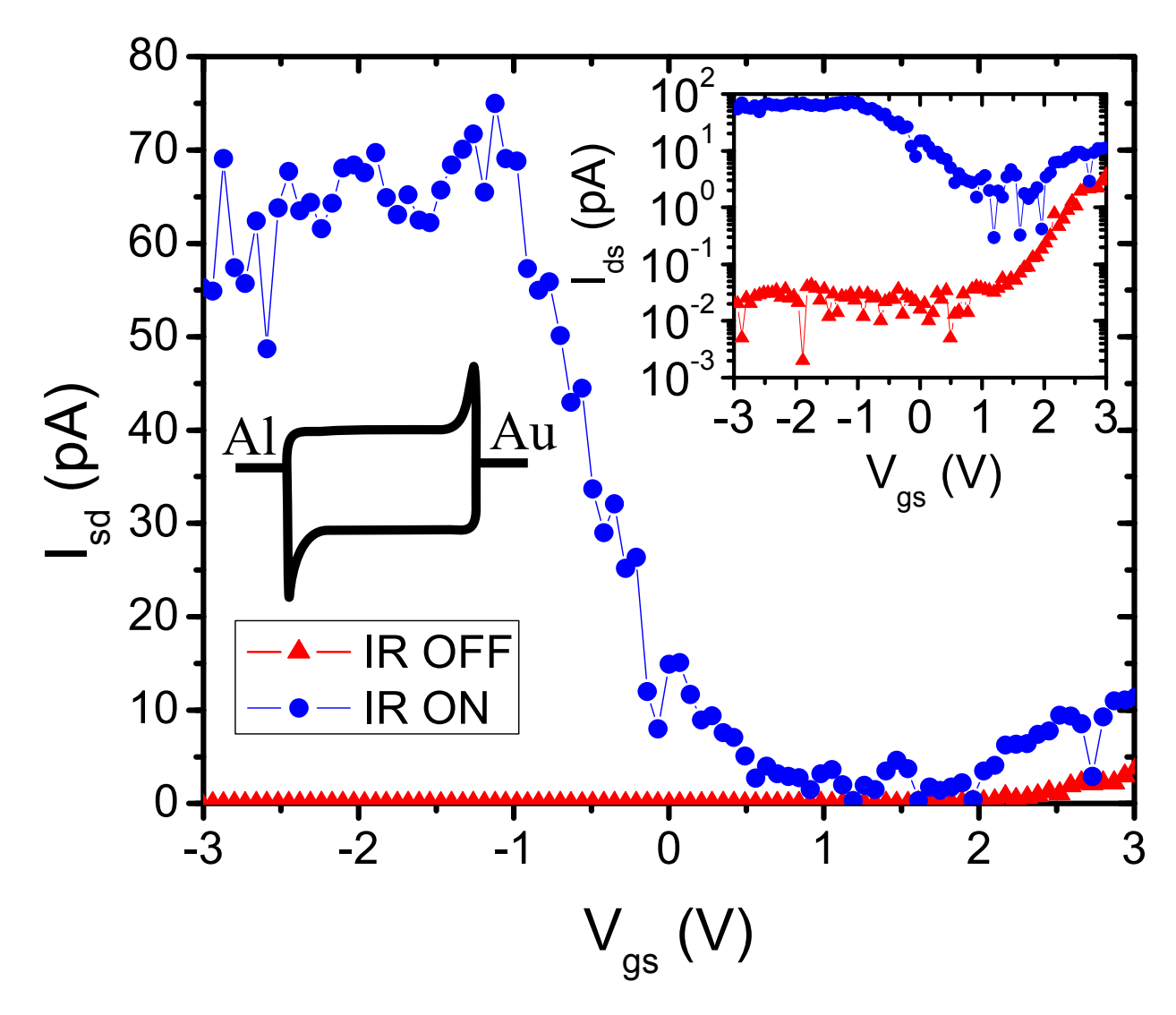


Figure 3.20: Transfer characteristics at zero bias of the asymmetric CNTFETs with absence and presence of IR illumination. The inset shows the transfer characteristics in logarithm scale. The band diagram shows the energy alignment of the device.

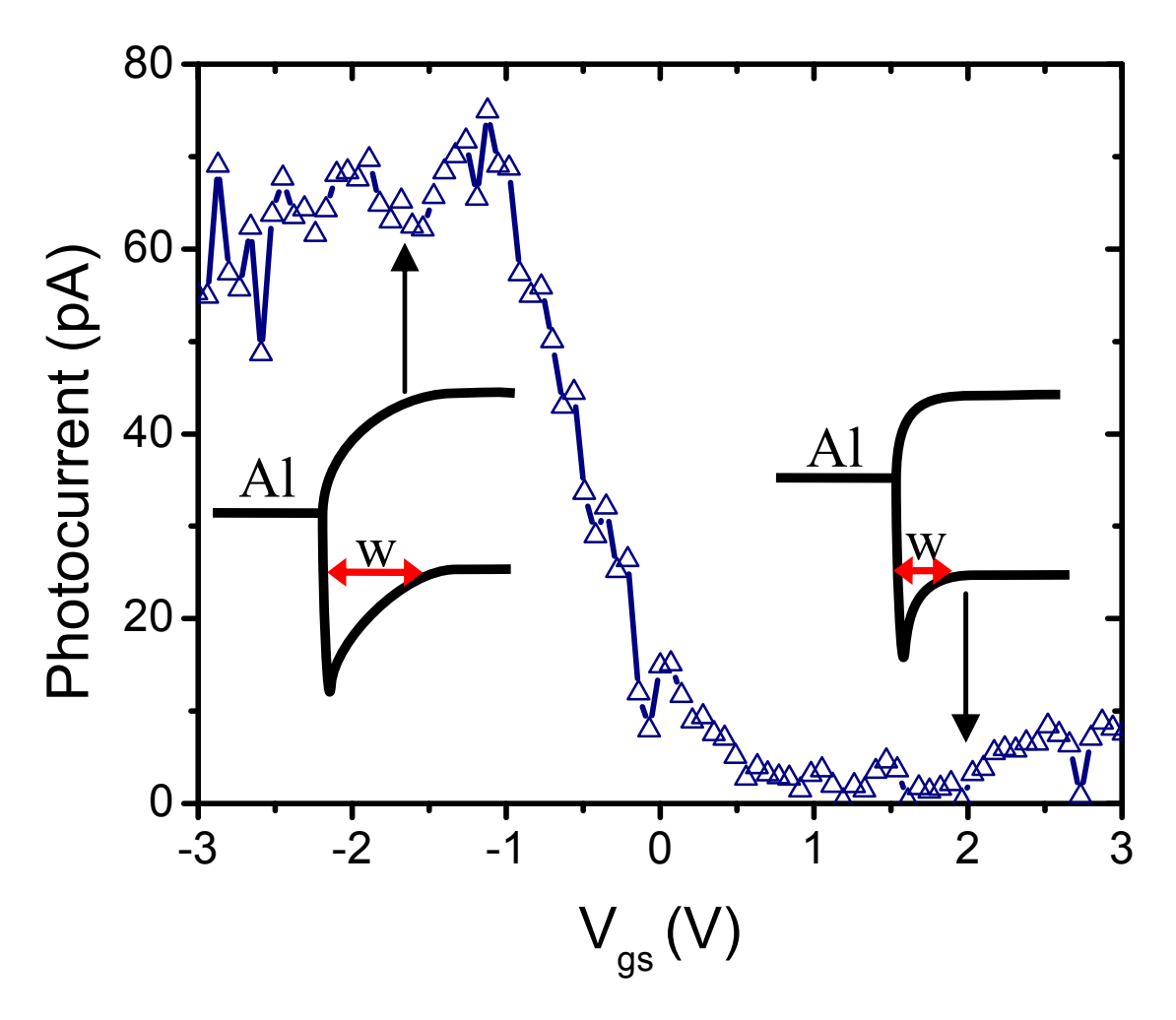


Figure 3.21: Photocurrent transfer characteristics of the asymmetric CNTFET at zero drain to source bias. The band diagrams show the barrier width (w) at negative and positive gate biases.

ing IR on and off at 0.2 Hz. Figure 3.22 shows that the dark current was reduced with decreasing Vgs at the absence of IR illumination, and the current was increased significantly upon light illumination, especially at large negative gate bias. The current dropped to the dark current when the IR laser was turned off. The reproducibility of the photo-response was excellent, and the response time was short. The maximum sensitivity was obtained at Vgs = -3 V with lowest dark current and highest photocurrent.

After the testing of back-gate dependent photo-responses, we compared the transfer characteristics of all gates. Considering the differences of distance and dielectric constant of the

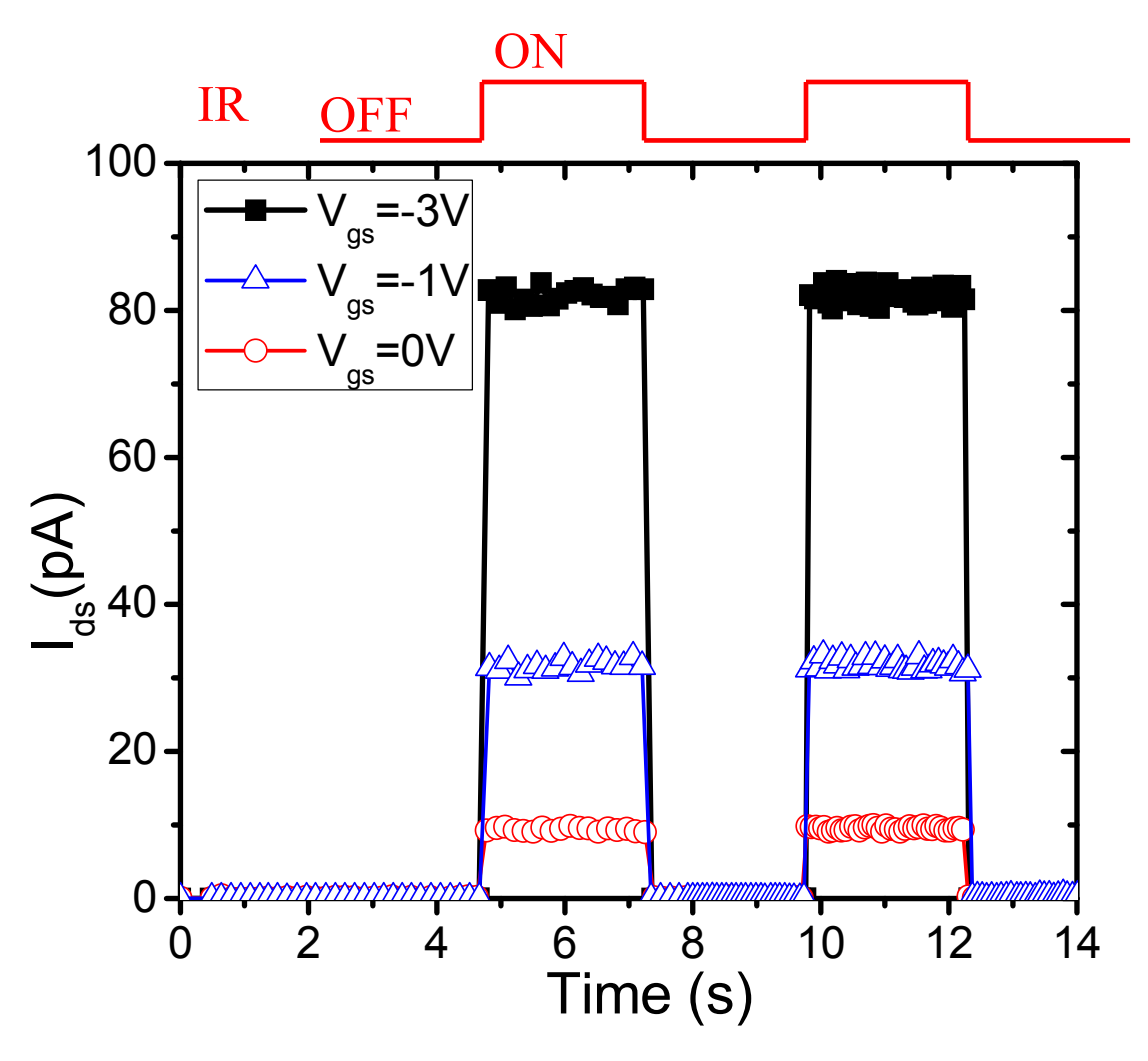


Figure 3.22: Temporal photocurrent measurement of the asymmetric CNTFET with three different gate biases (-3V, -1V, and 0V) by switching IR OFF and ON at 0.2 Hz.

back-gate and side-gates that capacitively-couple to the SWCNT, we normalized the gate voltages in transfer characteristics measurement. Figure 3.23(a) shows the normalized photocurrent transfer characteristics by sweeping the gate biases of back-gate (Vgs), source (Vg1), SWCNT channel (Vg2), and drain (Vg3) to independently dope different portions of the SWCNT. Unexpectedly, the trend of photocurrent transfer characteristics was the same, independent of the gate location. Although the Gate1 and Gate3 locally doped Au-CNT and Al-CNT contacts, all photocurrent transfer characteristics showed p-type characteristics that were the unique signature of Al-CNT contact (photocurrent decreased with increasing gate biases). The magnitude of the gate voltage to obtain maximum photocurrent was smallest for the back-gate (Vg=-2.3 V), while the largest gate voltage was required for the side-gates of drain (Vg=-3.5 V). These results were verified by temporal photocurrent measurement in order to avoid the influence of hysteresis [49]. We have fabricated five devices, all of which showed similar results.

These photocurrent transfer characteristics were completely different from conventional planar devices. We attribute this unique property to the charge distribution in 1D materials: there is a long tail extending from the junction into the undoped region, and this charge tail can be several micrometers long [15], as shown in Figure 3.23(b). This implies that the depletion region from the Al-CNT junction may extend into the whole SWCNT channel, and even approach the Au-CNT junction. In other words, the SWCNT channel became a partially "full" depletion region, resulting in an enlarged effective absorption area. Traditional p-n photodiode increases its effective absorption area by introducing an intrinsic semiconductor between p-type and n-type semiconductors to form the p-i-n junction, while 1D semiconductors can naturally enlarge their depletion region. The charge along the charge tail decreased from the Al-CNT depletion region towards to the Au-CNT contact, resulting

in the difference of magnitude of gate voltages required to obtain maximum photocurrent in Figure 3.23(a). In addition, this implies that the gate structure of CNTFETs can be simplified into a single gate structure, which can significantly facilitate large scale device manufacturing, and thus CNTFETs may become the building blocks for nano-photodetector arrays.

3.6 Detector Array using CNT based Transistors

In previous sections, we demonstrated that photocurrent improvement has weak dependence on the gate position. Thus multiple gates can be replaced by one pair of gates, as shown in Figure 3.24. This simplification can not only make the device smaller, but also avoid the electric field influence from neighboring devices.

A 3×3 CNT detector array was fabricated, as shown in Figure 3.25, which also shows the AFM image of the structure of one of its pixels. For this array, two Au electrodes of each detector were fabricated with a gap of 1 μm using EBL, thermal evaporation, and lift-off. A single CNT was then deposited between the electrodes using DEP deposition system and AFM manipulation system, followed by fabricating two gates and replacing one of the Au electrodes with Al. At the end, the whole device was packaged by a parylene-C layer in order to protect the device from environmental contaminations.

The pitch size of this array is 15 μm . Each individual detector in the array can be controlled independently using their own gates. We first measured the photo-response of each detector separately, and then calibrated proper values of Vg for each individual detector in order to make them generate the highest photocurrent.

By irradiating the detector array with IR photons from a laser, photocurrent of all detec-

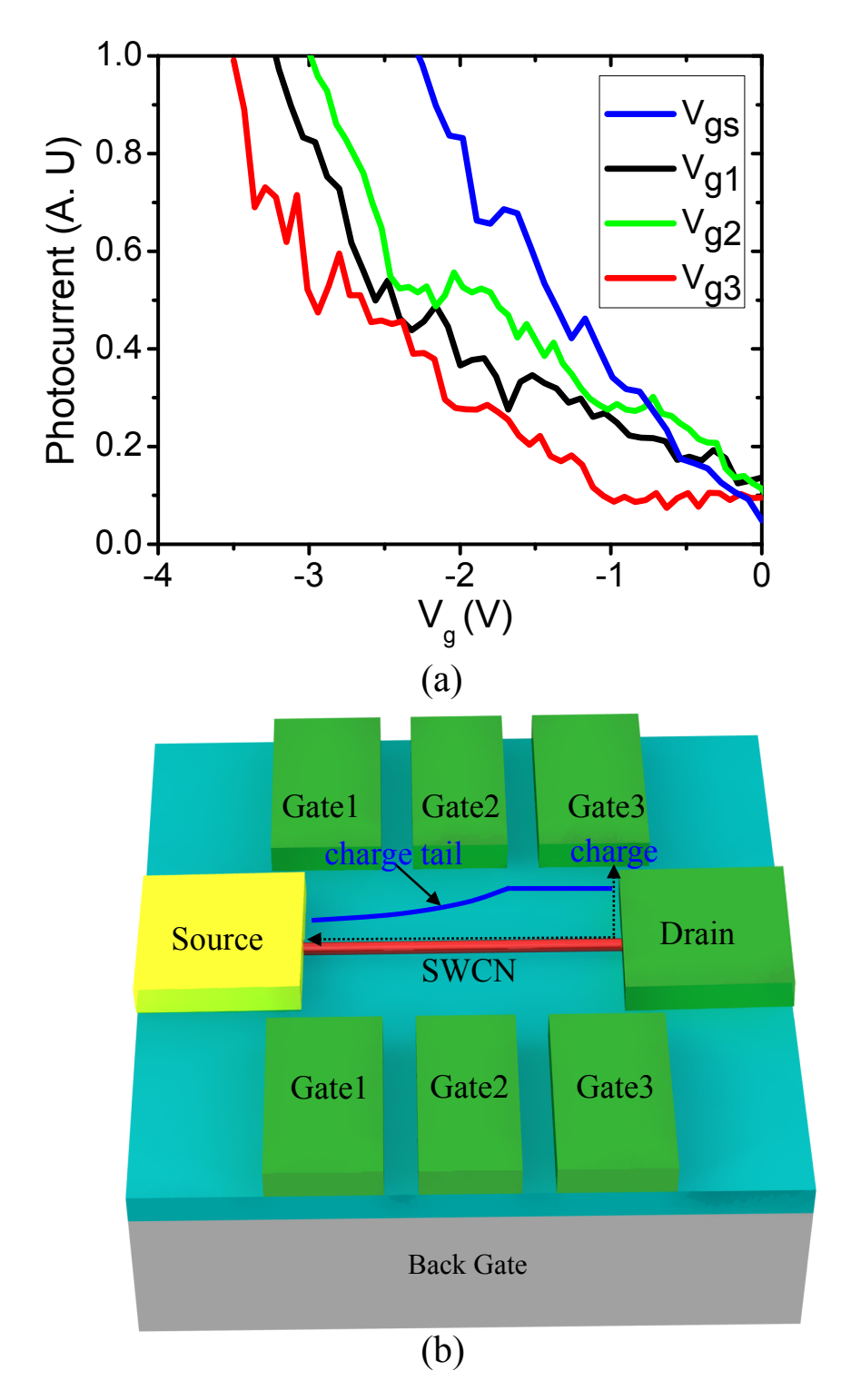


Figure 3.23: (a) Photocurrent transfer characteristics by applying gate biases to back-gate (Vgs), source (Vg1), SWCNT channel (Vg2), and drain (Vg3). (b)A 3D geometry of the multi-gate CNTFET and the charge distribution of the SWCNT, showing the charge tail on the SWCNT.

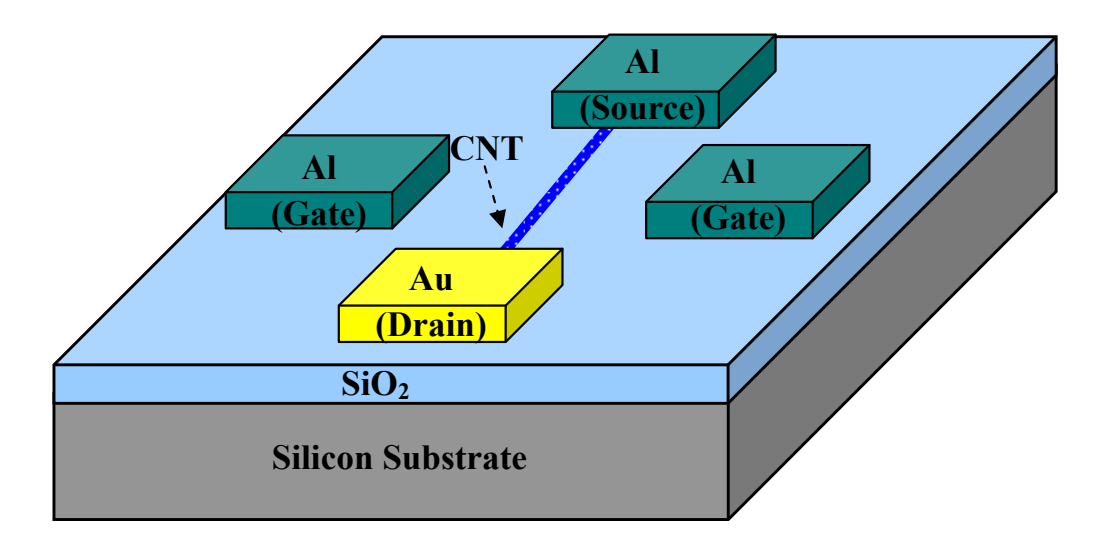


Figure 3.24: Asymmetric CNTFET with a simplified gate structure.

tors was measured. The images obtained from the measurement are shown in Figure 3.25. The color lightness shows the magnitude of photocurrent, which was normalized. In the images, the darker the color, the higher the Iphoto. Figure 3.25(a) shows that the highest light intensity of the laser is radiating on Pixel5. Other pixels have smaller Iphoto, and the value of Iphoto decreased as the distance between the detector and laser spot increased. When the laser was moved towards top-left, Figure 3.25(b) shows that the highest intensity point has moved to Pixel1. This detector array can be considered a small focal plane array in an IR imaging system. If the CNT detector array had a larger number of detectors, a higher resolution IR image could be obtained.

3.7 Chapter Summary

In summary, five types of CNTFETs were fabricated to investigate and improve the performance of the CNT based IR detectors. In the back-gate Au-CNT-Au CNTFET, the detector performance was improved by applying voltages to the back-gate, resulting in smaller dark

3x3 Detector Array Pixel9 Detector Al (Source) Al A1 (Gate) (Gate) Au (Drain)

Figure 3.25: The image of a 3x3 detector array and the AFM image of the Pixel9.

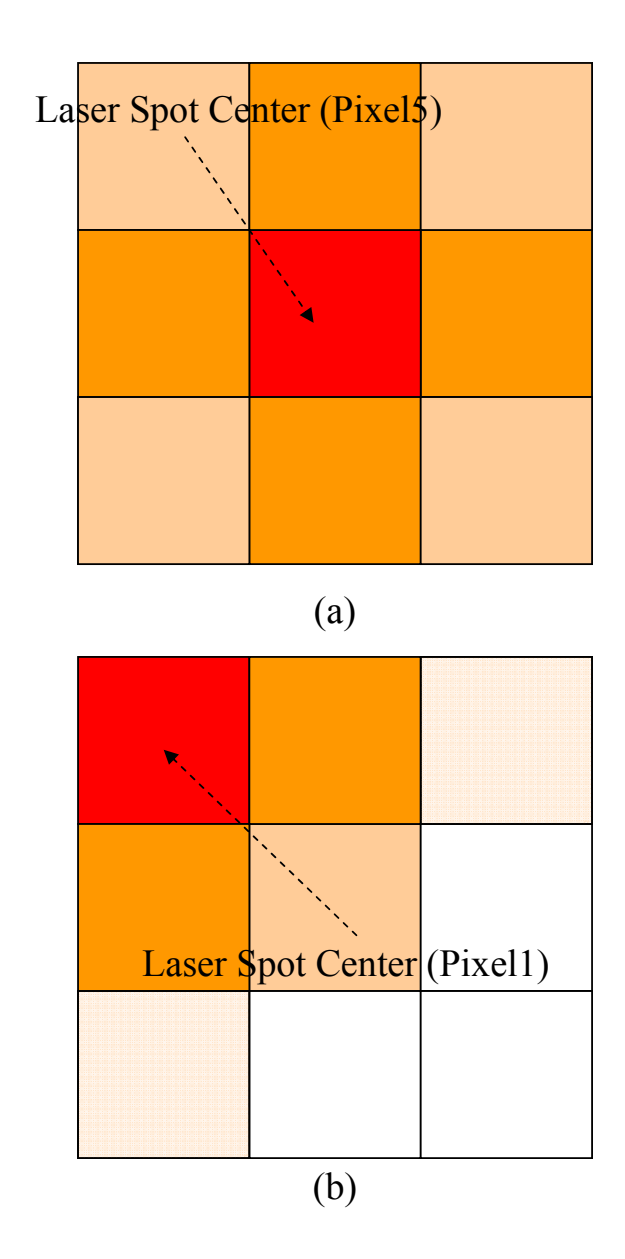


Figure 3.26: The images obtained from the detector array, and color lightness shows the magnitude of photocurrent. The laser spot center is on (a)Pixel5, (b)Pixel1.

current and higher Iphoto. Back-gate is capacitive-coupled to the CNT, thus applying Vg can electrostatically modulate the Fermi energy of CNT so as to control the Schottky barriers that are responsible for Iphoto generation. The back-gate Ag-CNT-Ag CNTFET produced higher Voc under IR illumination, since the built-in potential between Ag and CNT is higher than that of Au and CNT, showing the significance of metal workfunction. The previous two CNTFETs are with symmetric metal structures, which constrained the performance of the detectors, since separated electrons and holes from one Schottky barrier need to tunnel through another barrier. In the back-gate Au-CNT-Ag CNTFET, an asymmetric metal structure was used, and both Iphoto and Voc were highly improved. The reason is that the electrons and holes from the Ag-CNT interface only needed to pass through a small barrier between Au and CNT before being collected. CNTFET with back-gate structure is easy to fabricate and provide valuable information for improving detector performance. However, the back-gate structure is not suitable for larger scale detector arrays, because the back-gate will modulate all detectors simultaneously. A middle-gate CNTFET was fabricated in order to control each detector independently. But CNT detector with middle-gate structure and symmetric metal structure could not deliver optimal performance. In order to find the optimal detector design, an asymmetric multi-gate CNTFET was introduced, with asymmetric metal structure and multiple gates, including back-gate, gates for source and drain, and middle gates. A multi-gate CNTFET was developed and tested, revealing an unconventional photocurrent transfer characteristic, which was attributed to the unique charge distribution of 1D materials. Therefore, CNT detectors can be simplified into a single gate structure. A 3×3 focal plane array using the asymmetric CNT detector with one pair of side-gates was fabricated, effectively detecting the laser intensity distribution.

Chapter 4

Spectral Responses of CNT

Photodetectors

The bandgap energy of a CNT is inversely proportional to its diameter, therefore precise control of CNT diameter will find a wide range of applications in electronics and photonics. However, there are some technique difficulties to synthesize CNTs with an uniform diameter and chirality. In this chapter, we will firstly measure the spectral response of a SWCNT based photodetectors. Electrical breakdown process was introduced to tailor the bandgap energy of MWCNTs. After a number of consecutive breakdowns, it was found that CNT photodetectors can detect MWIR at room temperature.

4.1 Spectral Response of SWCNT based Photodetectors

In previous chapters, we have demonstrated that both asymmetric metal structure and electrostatic doping through a gate can significantly improve the photo-responses of CNT photodtectors. However, all previous testings used IR laser with wavelength of 830 nm as light source. Therefore, the spectral responses of the CNT photodetectors are not clear.

In order to understand the spectral responses of CNT photodetectors, a blackbody test-

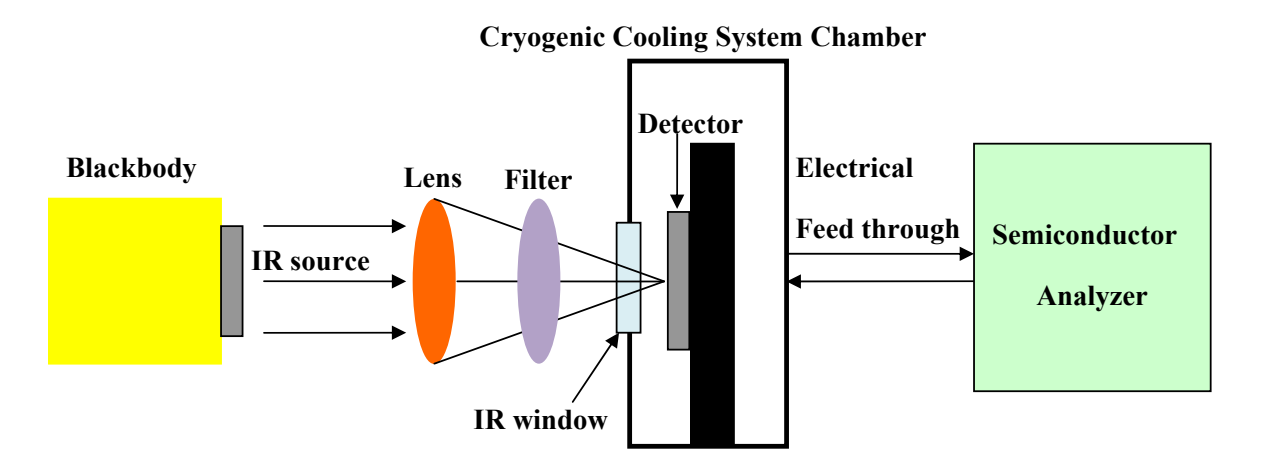


Figure 4.1: The blackbody testing system.

ing system has been developed as shown in Figure 4.1. The IR source with wide range of wavelengths radiates from an Oriel 67030 blackbody (Newport Corp.) with a temperature range of $50^{o}C$ to $1050^{o}C$. To measure the spectral responses of the photodetectors at a specific wavelength, different bandpass filters were used and positioned between the blackbody and the CNT photodetectors. The lens focuses IR signal onto the CNT photodetector that is mounted outside the cryogenic cooling chamber. The sensor temperature can vary from room temperature to $-196^{\circ}C$ by feeding liquid nitrogen. With the blackbody testing system, the CNT photodetectors can be characterized at different temperatures as well as different gas environments.

We fabricated an asymmetric (Ti-CNT-Au) CNTFET based photodetector with a backgate to provide electrostatic doping. The fabrication started with fabricating Au and Ti electrodes with a gap of 1 μm on top of a heavily doped Si substrate with a 200 nm-thick SiO₂ layer. An individual SWCNT was deposited between the electrodes using dielectrophorisis deposition system and AFM manipulation system. The I-V curves of the device at different gate voltages are shown in Figure 4.2(a). Current rectifying of these I-V curves revealed the asymmetric Schottky barriers at two contacts. The transfer characteristics (Figure 4.2(b))

of the transistor show that conductivity decreases with increasing gate voltage, a typical p-type transistor characteristic.

The temporal current at different gate voltages without IR illumination was shown in Figure 4.2(c). The dark current and noise obtained from Figure 4.2(c) are summarized in Table 4.1. The dark current is the average current; noise is the standard derivation of the current. Positive gate voltages can significantly reduce both dark current and noise due to the increase of built-in potential and the consequently enlarged Schottky barrier width.

Table 4.1: Dark Current and Noise at Different Gate Voltages

Vg (V)	Dark Current (pA)	Noise (pA)
-3	-52.3	14.5
0	-13.9	1.29
3	-2.65	0.14

The photo-responses of the detector were measured by using the blackbody as the IR source. There was no photo-response when zero gate voltage was applied (Figure 4.3(a)) by switching the shutter on and off at 0.5 Hz. When the magnitude of gate voltage was increased, the photo-responses became clearer to be detected due to the suppression of dark current and noise, and enhancement of photocurrent with proper electrostatic doping.

We also measured the spectral responses by using different bandpass filters in front of the detector. This photodetector can sense IR signals with wavelengthes of shorter than 1.55 μm , as shown in Figure 4.4. The diameter of the SWCNT was 1.2 nm, identified by the height information from an AFM. Diameter of 1.2 nm corresponds to bandgap energy of 0.7 eV, which equal to wavelength of 1.6 μm . There are two peaks in the spectral response: one at 1.55 μm , the other at 0.83 μm . Since the CNT is 1D material, its density of states is not continuous, but discrete. The two peaks can be explained by the Van Hove singularities

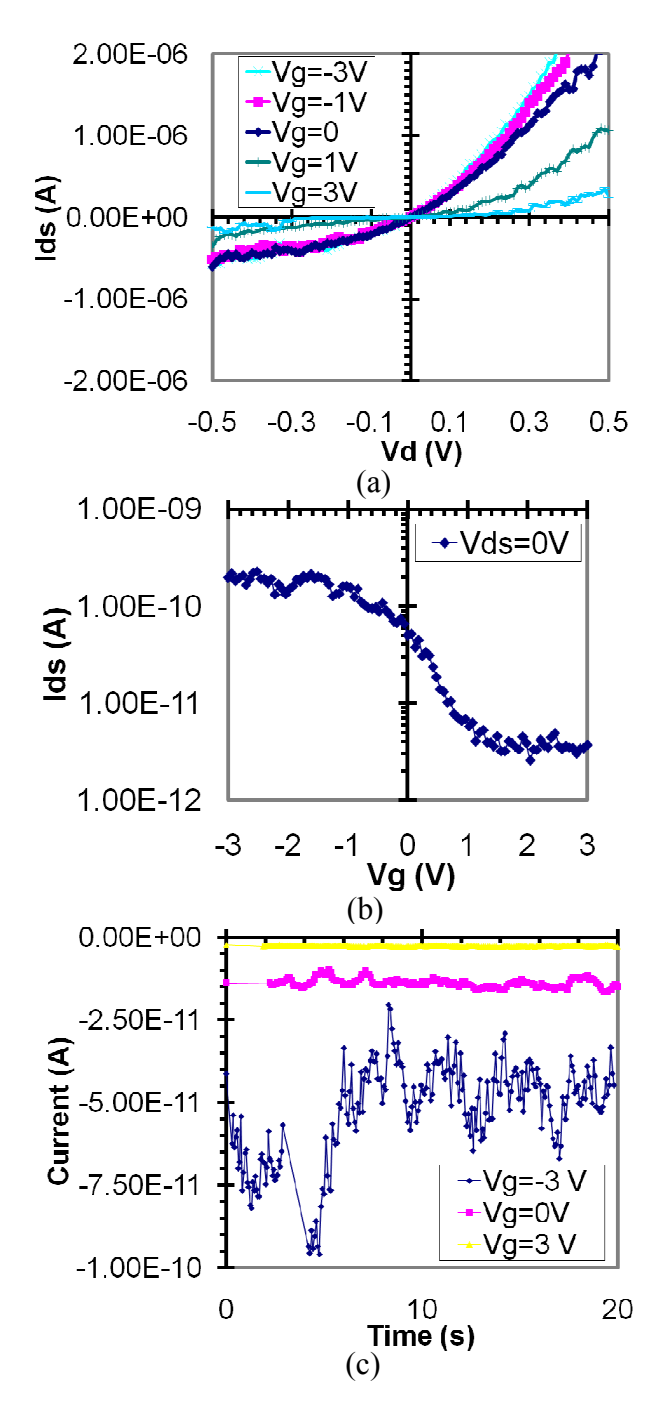


Figure 4.2: (a) The I-V characteristics of the transistor with Vg from -3V to 3V. (b) The relationship between Vg and current, showing conductivity decreases with increasing positive gate voltages. (c) The temporal dark current measurement with three different gate voltages.

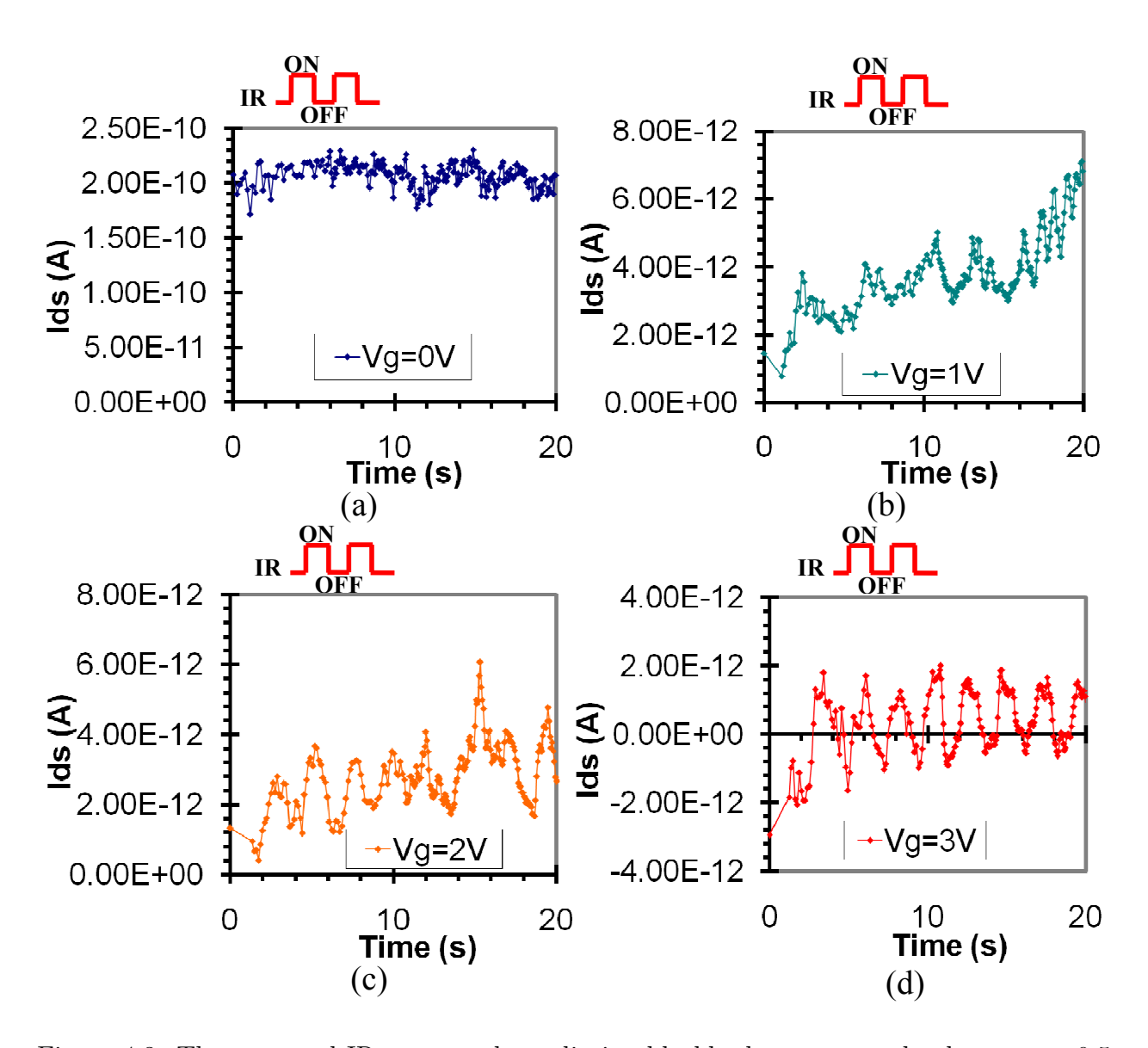


Figure 4.3: The temporal IR response by radiating blackbody source to the detector at 0.5 Hz with (a) Vg=0 V, (b) 1 V , (c) 2 V and (d) 3 V.

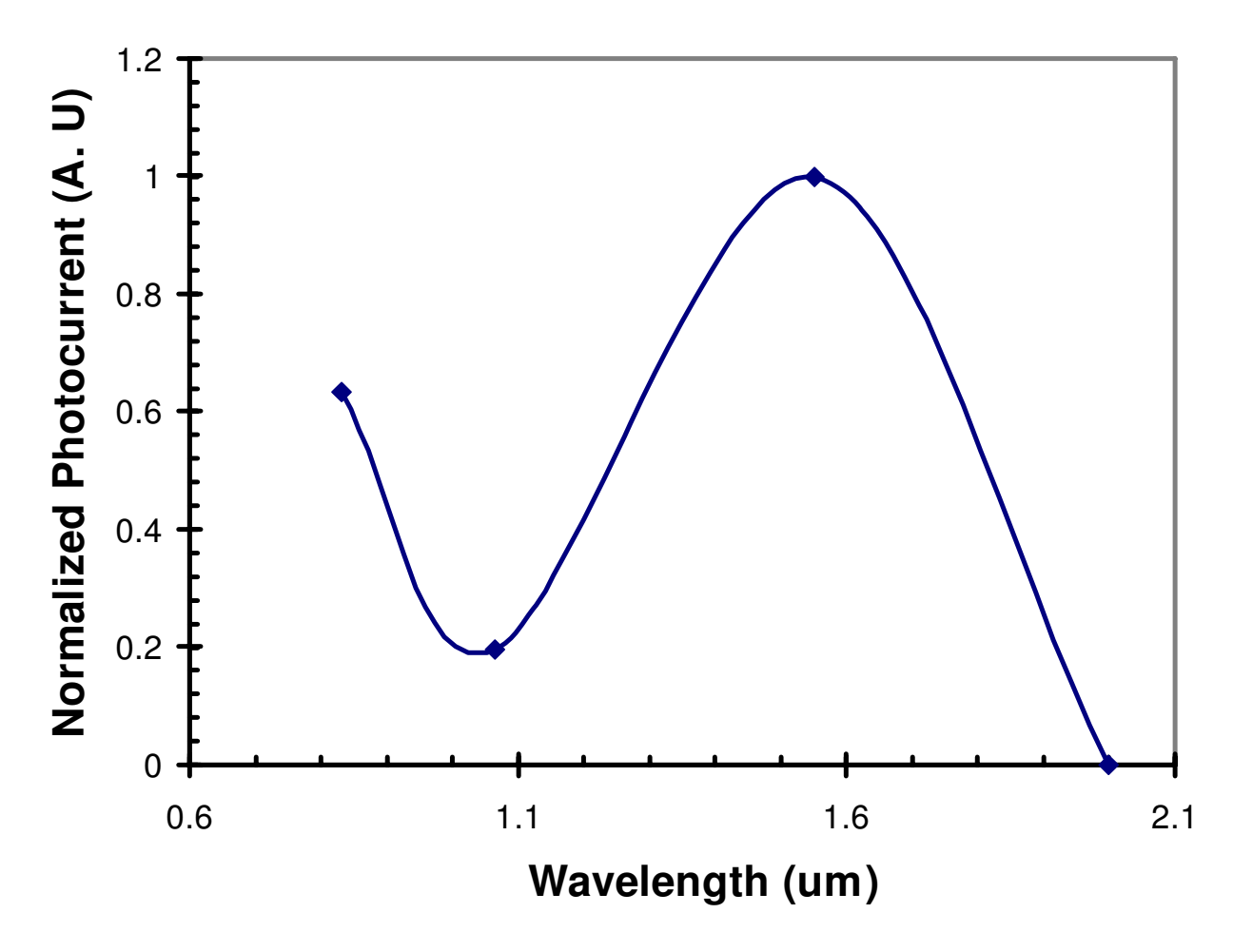


Figure 4.4: The spectral response of the SWCNT based photodetector.

occurs at E_{11} and E_{22} . The band structure of CNTs that have certain chirality can be calculated through well-established models [7,50]. A Kataura plot was proposed by Hiromichi Kataura to relate the diameter and CNTs and their bandgap energies in order to rationalize experimental findings [51]. It was found that E_{22} and E_{11} of 1.2 nm-diameter CNT resides at 0.83 μm and 1.55 μm .

4.2 Electrical Breakdown Control

It was demonstrated that SWCNT with 1.2 nm diameter can detect IR signal with wavelength shorter than 1.55 μm . In order to detect MWIR signal, the diameter of CNTs should be larger than 3 nm. Current synthesis techniques are difficult to grow uniform SWCNT with this large diameter.

MWCNTs are CNTs with a number of concentric nano-cylinders with varied diameters. MWCNTs may have much smaller bandgap than SWNCTs due to their large diameters. However, selecting MWCNTs with desired bandgap energies remains a major challenge. The as-synthesized MWCNTs are typically mixed with different bandgaps. In this section, we will introduce how to control MWCNT bandgap energy using an electrical breakdown system.

The electrical breakdown process was proposed by Collins et al. to peel off the outer shell of MWCNTs with applied voltages [24]. The shells of a MWCNT can only sustained certain power, therefore outer shells can be electrically removed when applied voltage beyond the breakdown limits. However, this bandgap engineering process remains uncontrolled that may result in cascade breakdown and cause the damage of MWCNTs.

In order to electrical breakdown the outer shell of MWCNTs in a control manner, we designed a controller to control the breakdown process in order to prevent cascade breakdown. The breakdown voltage was increased gradually according to the optimal estimate from the extended Kalman filter, which was designed based on the quantum electron transport model. Utilizing the statistical information of the current data as the feedback, the modeling error and random measurement noise are optimally minimized by the filter without sacrificing the response speed. The current signal caused by breakdown process can be detected by

fault diagnosis technique, which generates fault residual that stops the breakdown process. The controller is capable to generate stable breakdown voltage even with noisy and unstable current. The random current jitters will not yield large fault residual to affect the fault decision and cause a false alarm. When the fault residual exceeded fault threshold, a real breakdown was detected. The controller withdraw the applied voltage immediately to prevent the cascade breakdown. The fault threshold is experimentally optimized to minimize the false alarm and maintain quick response.

Figure 4.5 and Figure 4.6 show the breakdown process to control the MWCNT shell peel off using the controller. The breakdown process started with a bias voltage of 0.5 V, an abrupt current change was observed when the voltage was increased to 2.23 V (Figure 4.5). The control voltage was immediately withdraw to stop the cascade breakdown. The conductivity was decreased from 2.20×10^{-4} S to 1.52×10^{-4} S after one breakdown process due to the removal or the defect generation on the outmost shell (Figure 4.6).

In addition, an experiment was conducted to verify the CNT breakdown phenomenon. The results indicated the CNT breakdown happened at a particular region on the CNT. Single MWCNT was placed on three pairs of Au microelectrodes as illustrated in Figure 4.7(a). I-V characteristics of different segments (AB, BC, and AC) of the CNT were measured and studied before and after the breakdown process (see Figure 4.7). When a voltage was applied to the segment AB, the first CNT breakdown occurred between the segment AB. We observed a significant change in the I-V curve of the segment AB while no obvious change in the I-V curve of the segment AC included both the segments AB and BC, the I-V curve of the segment AC was also affected. Similarly, when the voltage was applied to the segment BC, the second CNT breakdown occurred between the segment BC, and the I-V curve between the segment AB remained unchanged because

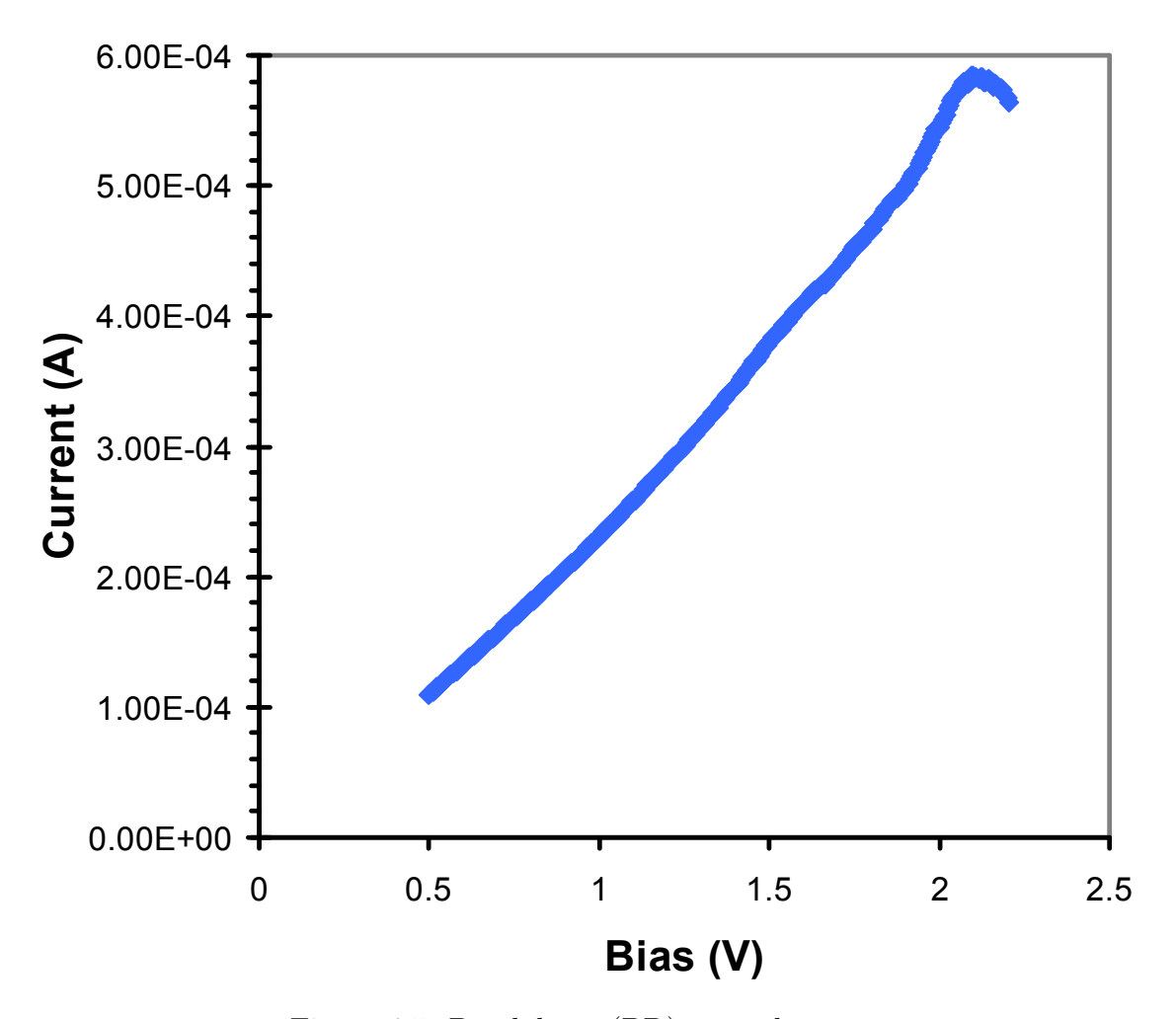


Figure 4.5: Breakdown (BD) control curve.

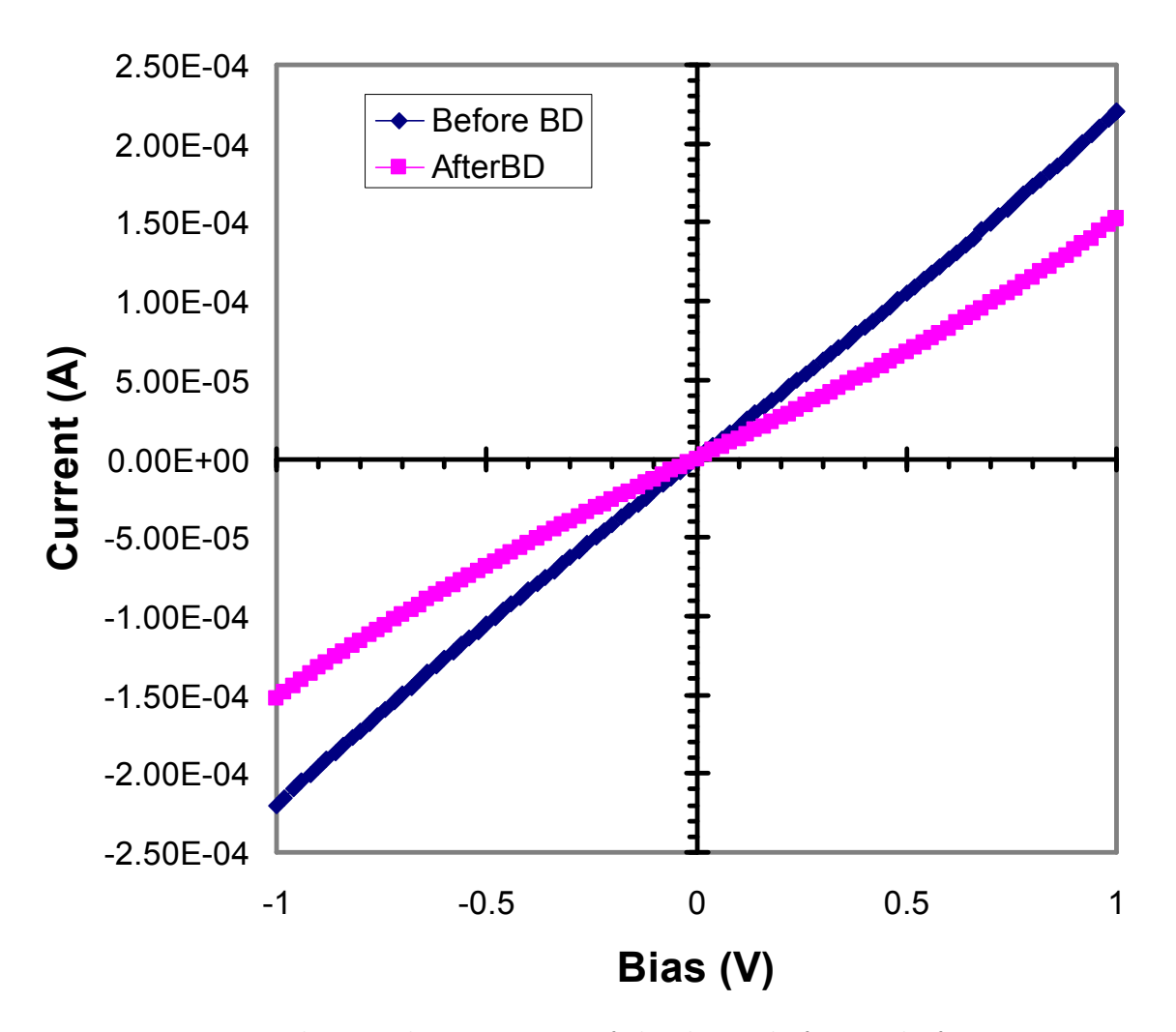


Figure 4.6: The I-V characteristics of the device before and after BD.

the breakdown occurred on the segment BC only. This experimental result clearly indicated that the breakdown position of a CNT can be adjusted by applying the electrical current at specific locations.

4.3 Spectral Response of MWCNT based Photodetectors

In order to detect MWIR, the functional materials need to have a bangap energy that is smaller than the energy of the MWIR photons. Bandgap energy of a MWCNT is proportional to its diameter, but most of MWCNTs have a over-size diameter, resulting in a zero bandgap energy. In order to control the bandgap energy to be a desired value, we used the breakdown control system to consecutively tailor the outer shells of MWCNT.

The fabrication of this device is similar to that of the SWCNT photodetector, but deposited MWCNT instead of SWCNT using the dielectrophorisis deposition system. Figure 4.8 shows the I-V curves of the MWCNT photodetector before and with 6 breakdowns. A linear I-V characteristic before breakdown indicates ohmic contact at both ends even though both metals have different work functions, reflecting the zero bandgap or metallic property of the as-prepared MWCNT. After serval consecutive breakdowns, current rectifying (curving I-V characteristic) became clearer, indicating the metallic MWCNT converts to a semiconductor MWCNT. The MWCNT photodetector cannot sense MWIR before the breakdown due to the zero bandgap energy of MWCNT with large diameter. After a number of breakdowns, we found that the photodetector can detect the radiation from the blackbody.

In order to understand its spectral responses, we measured the photocurrent by placing bandpass filters in front of the photodetector. It was found that the photodetector can

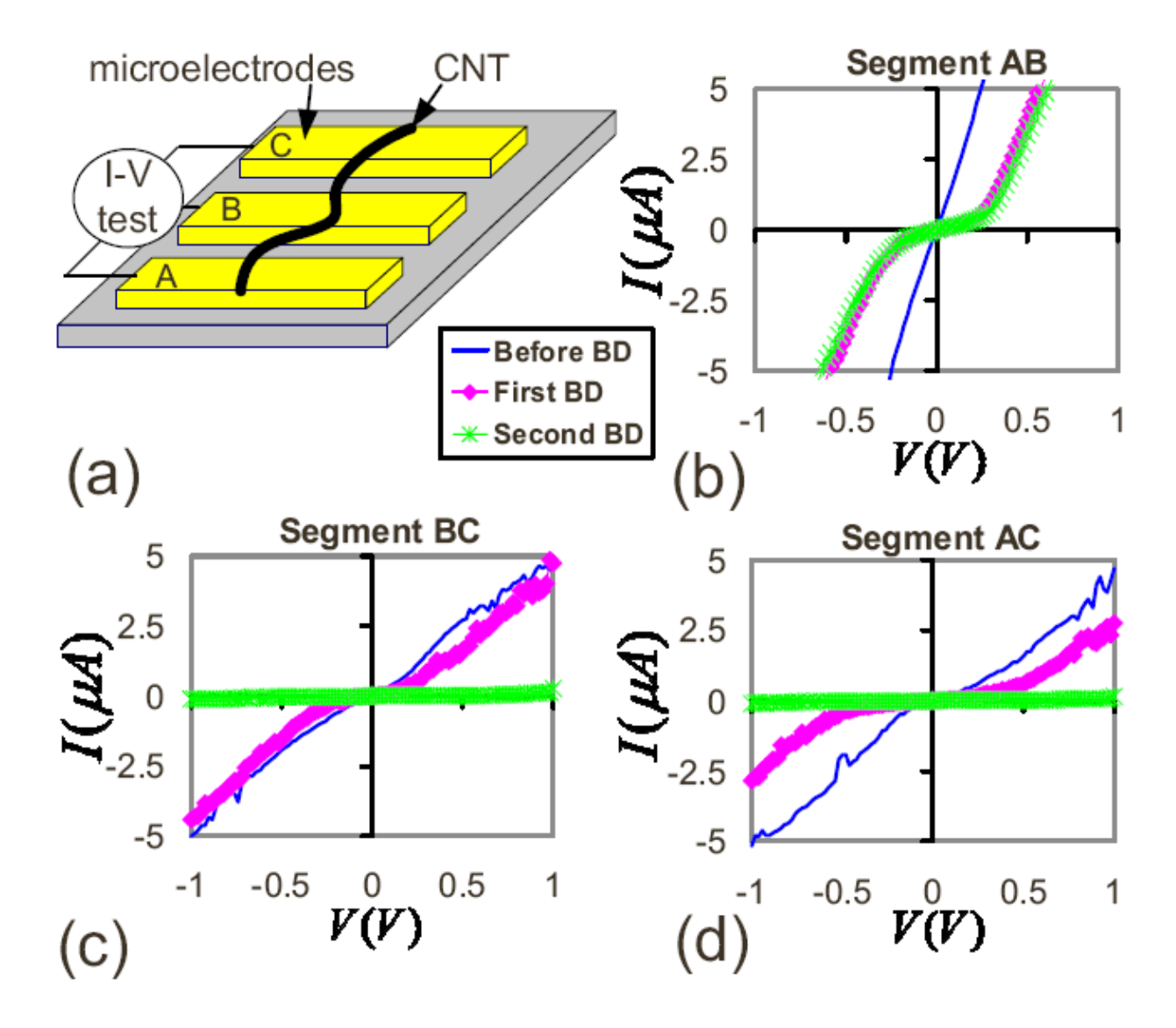


Figure 4.7: (a) Illustration showing a single MWCNT connected to three gold microelectrodes. The I-V characteristics of the MWCNT at different segments: (b) Segment AB, (c) segment BC, and (d) segment AC.

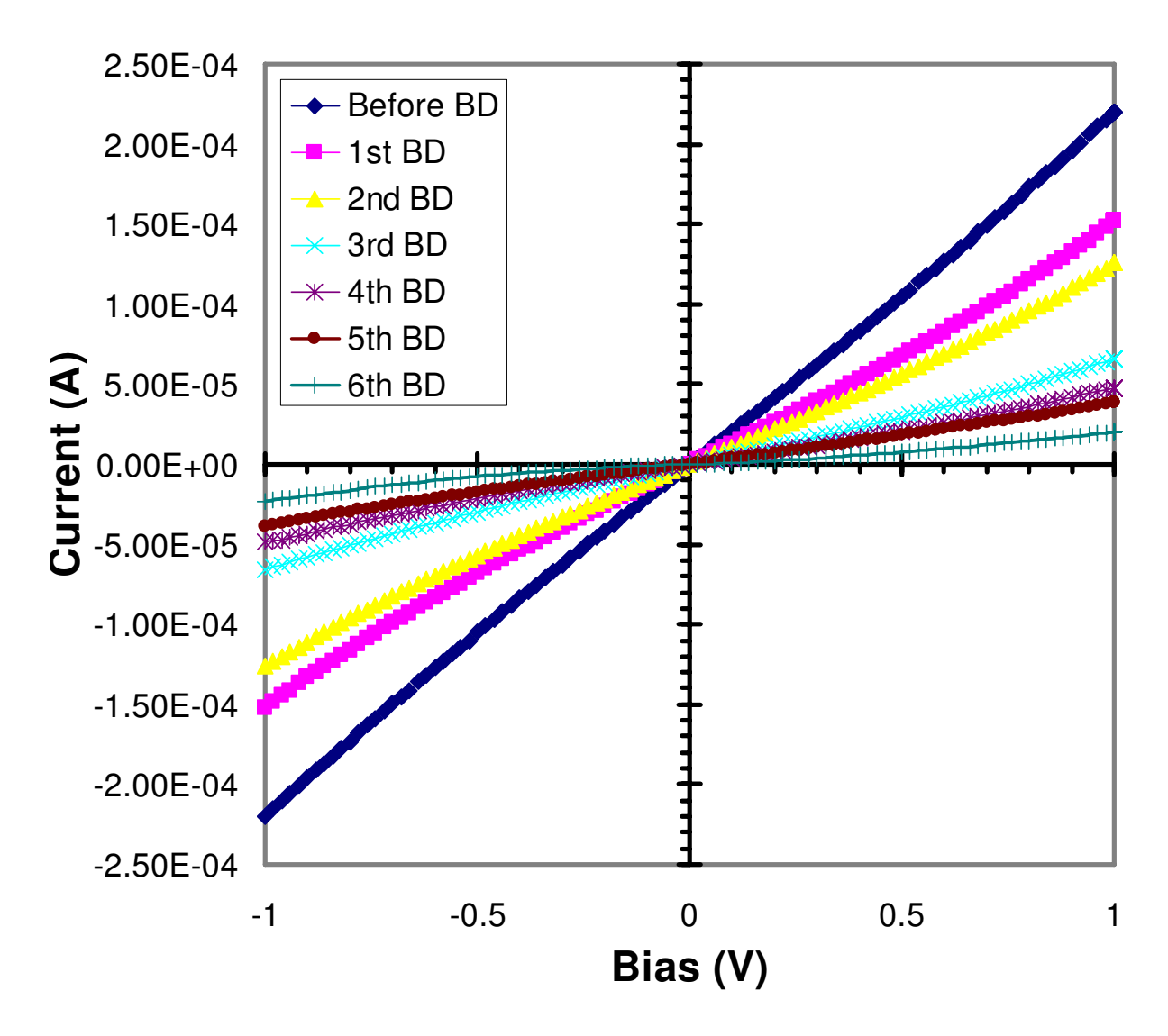


Figure 4.8: The I-V characteristics of a MWCNT photodetector before and after consecutive breakdowns (BD).

measure a wide spectrum ranging from 1 μm up to 8.8 μm , as shown in Figure 4.9. The measurement was performed at room temperature. In other words, this photodetector can sense MWIR and IR signal with longer wavelengthes at room temperature. In addition, we found that the detection spectrum can be tuned by controlling the times of breakdown. It should be noted that the detection spectrum of the MWCNT photodetector is much wider than that of traditional photodetectors. We attributed this to that multiple layers of MWCNT are contributing to the photon absorption and photocurrent generation. Conventional photodetectors need to stack materials that have different bandgaps to widen the detection spectrum, highly increase the fabrication complexity and cost [52–55]. The MWCNTs with controlled breakdown can be naturally a wide spectral material.

4.4 Chapter Summary

In summary, we measured the spectral responses of a SWCNT based photodetector, which can detect IR signal with wavelength less than 1.5 μm using a SWCNT with diameter of 1.2 nm. In order to measure MWIR, CNTs with larger diameters are required. An electrical breakdown system was developed to conquer the technical difficulties in synthesis CNT with desired diameters and bandgap energies. The electrical breakdown system precisely controlled the applied voltage to the MWCNT in order to prevent cascade breakdown. In other words, the outermost shell of the MWCNT can be breakdown one by one. After a number of consecutive breakdowns, the MWCNT based photodetector can detect MWIR at room temperature. The MWCNT showed wide spectral responses, which was attributed to the photon absorption at multiple layers of the MWCNTs.

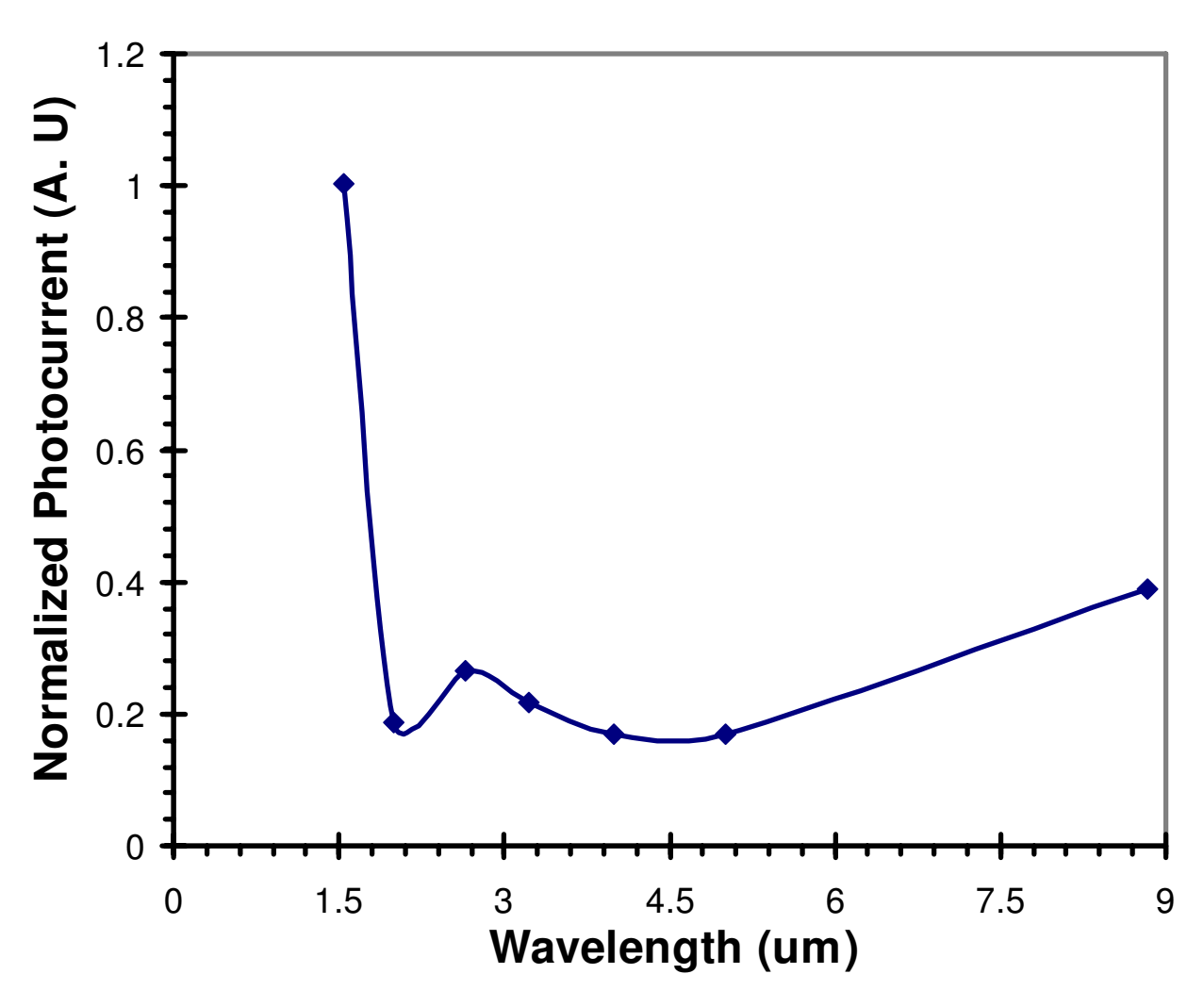


Figure 4.9: The spectral response of the MWCNT based photodetector.

Chapter 5

Plasmonic Lens using Optical

Antenna

CNT based photodetectors have shown outstanding performance by using CNT as sensing element. However, detection wavelength is much larger than the diameter of the CNT, resulting in small fill factor (absorption area). Bowtie antenna can confine light into a subwavelength volume based on plasmonic resonance, acting as a plasmonic lens. Therefore, integrating a bowtie antenna to CNT based photodetectors can highly improve photo-response of the detectors. The electric field enhancement of bowtie antennas was calculated using the device geometry by considering fabrication difficulties and photodetector structure. It is shown that the electric field intensity enhancement increased exponentially with distance reduction between the CNT based photodetector to the antenna. A redshift of the peak resonance wavelength is predicted due to the increase of tip angles of the bowtie antennas. Experimental results showed that photocurrent enhancement agreed well with theoretical calculations. Bowtie antennas may find wide applications in nano-scale photonic sensors.

5.1 Introduction of Optical Antenna

We have demonstrated that CNT can be utilized as a functional element for photodetectors. However, a critical challenge for obtaining high performance 1D photodetectors is the dimension incompatibility between photodetectors and optical wavelengths. The radial sizes of CNTs are much smaller than detection wavelengths, resulting in low fill factor and responsivity. Motivated by this challenge, optical antennas were designed to integrate with CNT based photodetectors so as to bridge the gap between nano-size sensing elements and micro-size wavelengths. Due to plasmonic resonance, optical antennas can confine strong optical near fields in a volume far below a cubic wavelength of excitation light. This can greatly enhance photon absorption owing to the increase of coupling between CNT and vibrating electrical fields of photons. By integrating CNT based photodetectors with optical antennas, the nano-scale photodetectors can be made with outstanding performance and photon absorption efficiency.

In our design, the optical antenna performs as a plasmonic lens that funnels light into the CNT based photodetector. This is analogous to the microlenses on top of conventional charge coupled device (CCD) array to increase detector fill factor [56]. If the CNT based photodetector occupied the same area as the antenna/CNT photodetector, they have same fill factor. However, technical difficulties prevent the assembling of a large array of uniform CNTs. Assembling a CNT thin film has been demonstrated, but the interaction between CNTs in thin film resulted in the loss of their unique optical properties. Therefore, one single CNT is more favorable and easier to manipulate in order to fabricate high performance photodetectors. But the challenge of one individual CNT as the core material for photodetectors is the small diameter of CNT. The optical antenna can strongly concentrate light into sub-wavelength volume that couples to the CNT in order to improve fill factor.

Optical antennas have invoked considerable interests, because of their ability to generate large and localized electromagnetic fields. The basic principle of optical antennas is based on the resonant behavior between excitation light and metal structure. When light inter-

acts with optical antennas that have proper dimensions, surface plasmons are generated due to resonant coupling between the electromagnetic surface waves and oscillations of free electrons in the metal. Light irradiating on the optical antenna at frequencies below the resonant frequency is reflected, since it induces motion in the charge carriers that act to screen out the incident field [57]; when the frequency of light is above the resonant frequency, light is transmitted because the charges are unable to respond quickly enough to screen out the incident field; only at the resonant frequency, light is resonant coupling to free charges of metals, and the incident waves will be absorbed and reradiated. By properly orienting the reradiated waves, intensely localized near-fields can be generated. Confining or localizing light into a small volume has found plenty of applications in many research fields, including spectroscopy, microscopy, lithography, bio-sensing, chemical studies, and so on [58, 59]. In recent years, optical antennas used to improve the performance of planar photovoltaic devices became a hot field [60]. However, very little research was conducted to improve the performance of 1D photodetectors using optical antenna, although 1D materials become an emerging platform in photovoltaic devices [61].

There are a variety of novel shaped optical antennas, such as nano-sphere, nano-rod and nano-triangle monomers, nano-sphere dimmers, dipole antennas, bowtie antennas, Yagi-Uda antennas, cross antennas, and so on [59]. Among all these optical antennas, dipole and bowtie antennas are particularly suitable for integrating with 1D photodetectors because of their geometries. Dipole antennas are nano-rod dimmers, while bowtie antennas are nano-triangle dimmers, therefore both dipole and bowtie antennas can be considered as two opposing tip-to-tip nano-triangles (non-zero apex width) with tip angles ranging from 0 degree (dipole antennas) to wider angles. The coupling between two pieces of metals in these antennas concentrates the incident light into a nano-scale gap, which locates above a

CNT photodetector in order to enhance the interaction between the localized near-fields and CNTs.

There were a number of approaches to improve a photodetector's performance using plasmonic resonance: photocurrent enhancement was demonstrated in a Si photodiode via the excitation of plasmon resonances in spherical Au nanoparticles deposited on the Si surface [62]; a middle-wave IR photodetector, comprised of a metallic grating filled with HgCdTe, was proposed to improve the signal-to-noise ratio by plasmonic resonance [63]; an optical antenna was utilized as a metal electrode for a Si Schottky diode to boost photo-detection [64]. Optical antennas were embedded in these photodetectors, acting as part of the photodetectors. In our design, the bowtie antenna performs as a plasmonic lens, which can be easily integrated into all types of high performance 1D photodetectors [20, 23, 65]. In particular, the bowtie antenna perfectly matches with the CNT photodetector due to the compatibility of the diameter of CNT and gap distance of the bowtie antenna, because the electric field (E-field) enhancement exponentially increases with decreasing gap distance [66].

The properties of free-standing optical bowtie antennas have been studied extensively [67], and our group has demonstrated that dipole antenna can boost photo-response of 1D IR detectors [68]. However, the design of bowtie antennas for 1D photodetectors was not systematically studied. In this chapter we will present the design of bowtie antennas that can be integrated with CNT photodetectors to highly improve the detection of IR signal with wavelength of 830 nm. E-field enhancement with bowtie antennas was calculated to seek the optimized tip angle and insulator thickness. Experimental results showed that the photocurrent enhancement was 12.67 times by adding a bowtie antenna with precise alignment and dimension control in fabrication. Calculation of relative energy difference on the CNT photodetector at absence and presence of the bowtie antenna quantitatively

explained the photocurrent enhancement.

5.2 Design of Bowtie Antennas

The bowtie antenna consists of two tip-to-tip nano-triangles that can confine strong electromagnetic field between two triangles at resonance frequency. Light illuminating on the bowtie antennas will generate instantaneous current, which oscillates at the frequency along the polarization of the incident light. The instantaneous current is maximum near the center of the nano-triangle, and decreases toward the edges of the antenna. This leads to a high density of surface charge at the tip of the nano-triangles. Displacement current flows into the small air gap of the bowtie antennas, reradiating the absorbed energy. The strong coupling of these two opposing tip-to-tip triangles brings the center of the reradiating source to the center of the gap [69]. The maximum intensity enhancement can be obtained at resonance frequency, which is mainly determined by the dimension and materials of antennas.

One thing should be noted is that the depletion region of the CNT photodetector may extend into the whole tube of the CNT, since the charge distribution of the 1D systems has a long-range tail, extending over the entire CNT [15]. In other words, the entire CNT can be considered as depletion region. Therefore, the optical antennas can not only be located on the contacts, but they also can be placed on top of the CNT body. The relative position of the CNT photodetector and bowtie antenna is shown in Figure 5.1. A thin insulator (Si_3N_4) is sandwiched between the bowtie antenna and the photodetector (Figure 5.1(c)), with the gap of bowtie antenna aligning to the center of CNT channel. The geometrical parameters are also denoted in Figure 5.1: where d is the gap distance, w is the apex width, L is the length of the bowtie antenna, θ is the tip angle, and t is the thickness of the insulator

between antenna and CNT.

This CNT photodetector is designed for detecting IR signal at 830 nm, thus the bowtie antenna should resonate at or close to this wavelength. Resonance wavelength is very sensitive to the dimensions of bowtie antennas, but several parameters are fixed in simulation considering the fabrication constraints, and some parameters have been extensively studied [70]: the gap distance d is set to be 30 nm for easier alignment of the bowtie antenna to the photodetector; apex width is 30 nm to leave some tolerance for EBL; antenna length L is 400 nm because it is close to half-wavelength of the IR signal; the bowtie antenna is made of 3 nm Ti and 20 nm Au. The width of both Au and Ti electrodes is 400 nm, and the gap between two electrodes is 1000 nm. The following simulation was based on the geometry including both electrodes and bowtie antennas, as shown in Figure 5.1.

The E-field enhancement spectra of bowtie antennas will be simulated with varying insulator thickness t and tip angle θ , not only since these two parameters can be easily tuned in real device fabrication, but they also have significant impacts to the E-field intensity enhancement.

Figure 5.1(a) also shows the direction of incident light polarization and the coordinate system for all numerical simulations using ANSYS HFSS: a plane wave is normally incident on the structure from the top with the electric field being polarized along the x axis, which is parallel to the axis between two triangles, with electric field component amplitudes of E_x =1 V/m, E_y = E_z =0.

5.2.1 Insulator Thickness Dependent E-field Enhancement

The plasmonic resonance of the bowtie antennas was first investigated by varying the insulator thickness t between the antenna to the CNT photodetector. This is a critical parameter,

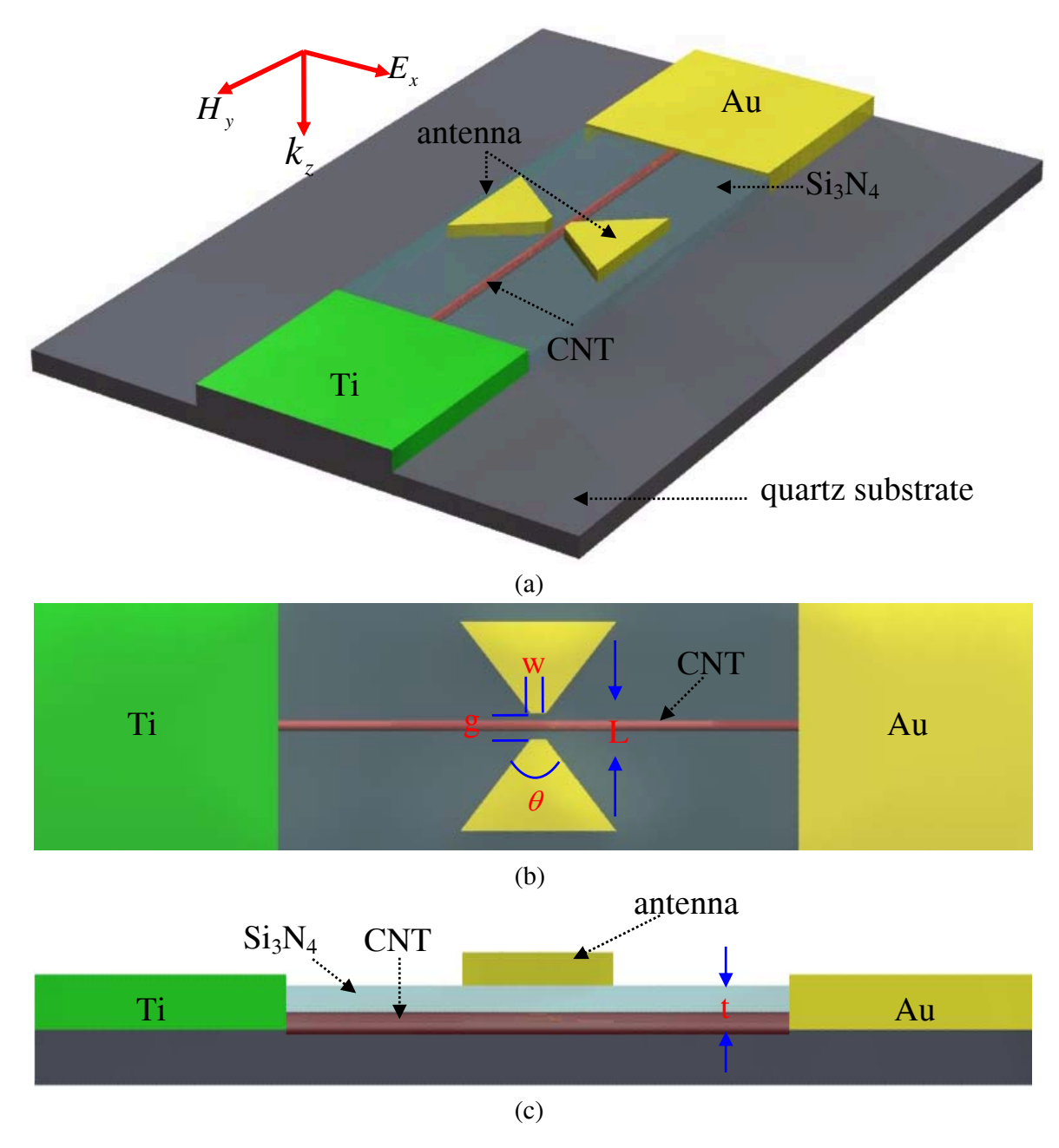


Figure 5.1: (a) A 3D geometry shows the relative position between the CNT based photodetector and the bowtie antenna. The incident light with electric field polarized in the x direction propagates in the z direction. (b) Top view of the device, and parameters of the bowtie antenna: L=400 nm is the length of the antenna, g=30 nm is the gap of two pieces of the antenna, w=30 nm is the apex width, and is the tip angle. (c) Side view of the device, showing the CNT based photodetector and bowtie antenna sandwiching the Si_3N_4 layer that has a thickness of t.

since the photodetector needs to be placed in close proximity to the optical antennas in order to fully take advantage of near fields [71]. The insulator thickness dependent E-field distribution at the substrate plane (the plane between Si_3N_4 and quartz substrate), where CNT located, was calculated based on equilateral Au triangles (θ =60 degrees) with d=30 nm, w=30 nm, L= 400 nm. The CNT photodetector and optical antenna are on the top of a quartz substrate, with a plane-wave light polarized in the x direction normally illuminating the device from the top.

The resonance wavelength for this antenna is at 845 nm with t=10 nm. Figure 5.2(a) shows the E-field distribution between two electrodes at the substrate plane for the device with t = 10 nm at its resonance wavelength. The E-field is confined into the gap of the bowtie antenna with the maximum amplitude located at the center of the gap due to the strong coupling between two nano-triangles. The E-field distribution is in the shape of a horizontal bowtie, and the amplitude of the E-field decreases as the distance to the center of the gap increases in the horizontal direction. The illuminating light had E=1 V/m, while the peak amplitude at substrate plane became E=14.608 V/m at resonance after adding the bowtie antenna, with an enhancement of 14.608 fold.

The peak E-field intensity enhancement $Max(|E|^2)$ as a function of insulator thickness at resonance wavelength was shown in Figure 5.2(b). The E-field distributions with thickness of Si_3N_4 ranging from 10 nm to 50 nm were investigated. The blue curve shows the peak intensity enhancement at the substrate plane: the enhancement decreased from 213.1 to 26.7 when the thickness of the Si_3N_4 increased from 10 nm to 50 nm. The red curve in Figure 5.2(b) is the exponential fit of the data, which matches very well with the blue curve. The resonance wavelength of the antenna redshifted from 845 nm to 1034 nm with the thickness increasing of Si_3N_4 layer from t=10 nm to t=50 nm [72]. The inset of Figure 5.2(b)

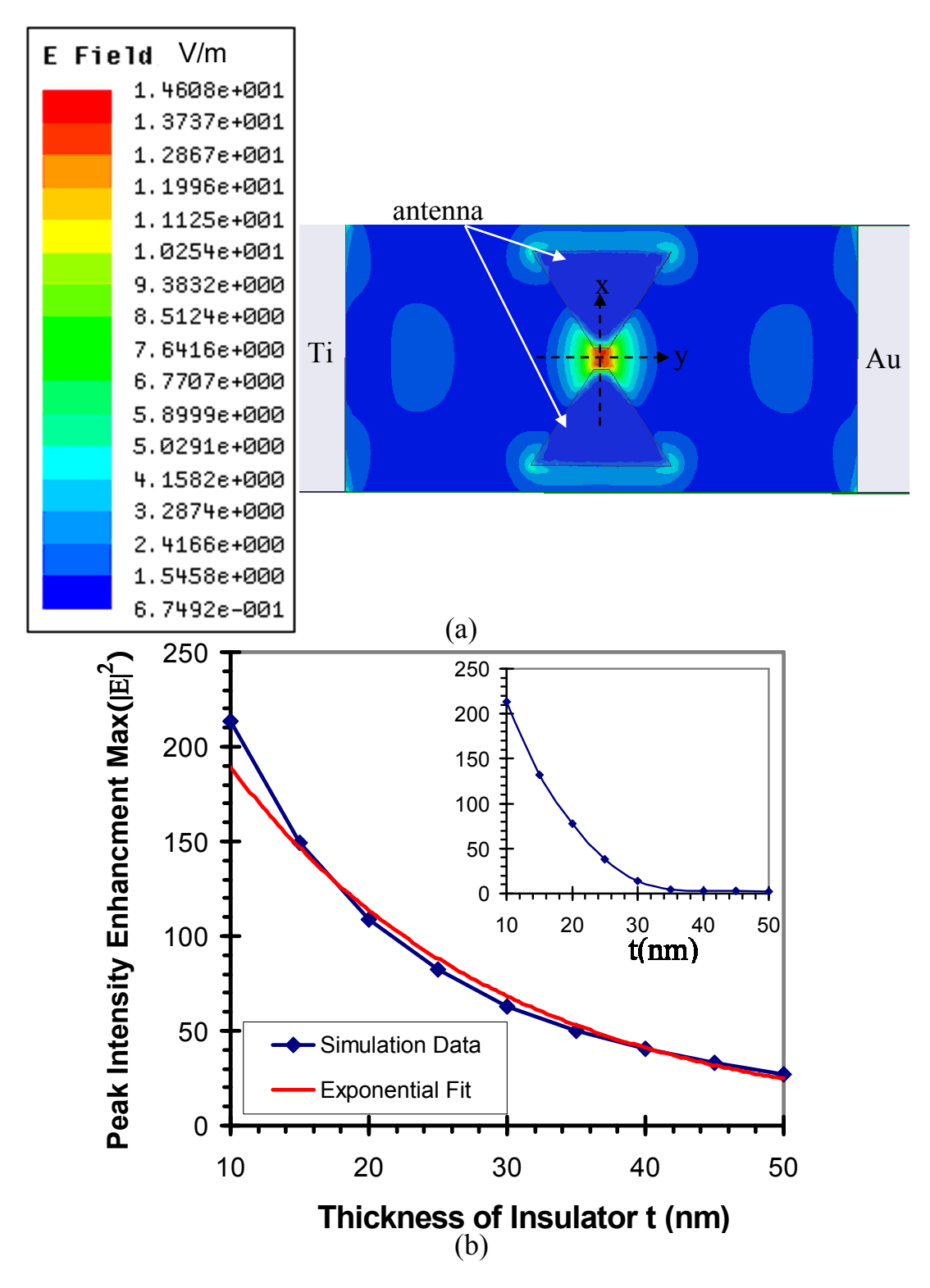


Figure 5.2: (a) The E-field distribution of the resonance frequency (845 nm) of the bowtie antenna with θ =60 degrees, and t=10 nm. The x-y axis show the coordinate for simulation. (b) The t dependent peak field intensity Max($\mid E\mid^2$), blue curve is the simulation values, and red curve is the exponential fit. The inset shows field intensity enhancement $\mid E\mid^2$ at wavelength of 830 nm.

shows that the E-field enhancement at wavelength of 830 nm, which corresponds to the wavelength of our laser source, decreases dramatically by increasing the insulator thickness. The simulation results indicate that the field intensity enhancement decreases significantly with the increasing thickness of the insulator, because evanescent waves decay exponentially from the antenna. Therefore, in order to fully use the power of the antenna, the photodetector needs to be fabricated close to the bowtie antenna.

5.2.2 Tip Angle Dependent E-field Enhancement Spectra

Not only is the tip angle of the bowtie antennas easily modified in real device fabrication, but it also has critical impact on both resonance wavelength and E-field intensity enhancement. The E-field spectra as a function of the tip angle were calculated with d=30 nm, w=30 nm, L= 400 nm, and t=10 nm. Figure 5.3 shows the E-field spectra of bowtie antenna with tip angles of 0 degrees (dipole antenna), 30 degrees, 60 degrees, 90 degrees, and 120 degrees.

The spectra vary significantly with different tip angles. It is shown that bowtie antennas cover wider spectrum with larger tip angles. Bowtie antennas can be considered as a two-dimensional analogue of biconical antenna, therefore wider tip angles are expected to possess broader bandwidth. The bowtie antenna with tip angle of 120 degrees shows field intensity enhancement in a broadest spectrum. What is more, two resonance wavelengths was found with a fundamental resonance wavelength at 1.13 μm and a high-order resonance at 0.77 μm . High-order resonance is easier to be excited for large angle Bowtie antennas, since larger angle bowtie antennas are prone to overcome the symmetry limitation of octupolar resonance, while octupolar resonance is forbidden in the 0 degree bowtie antenna under normal incidence [73].

The peak E-field intensity enhancement increases with wider tip angles when the tip angle

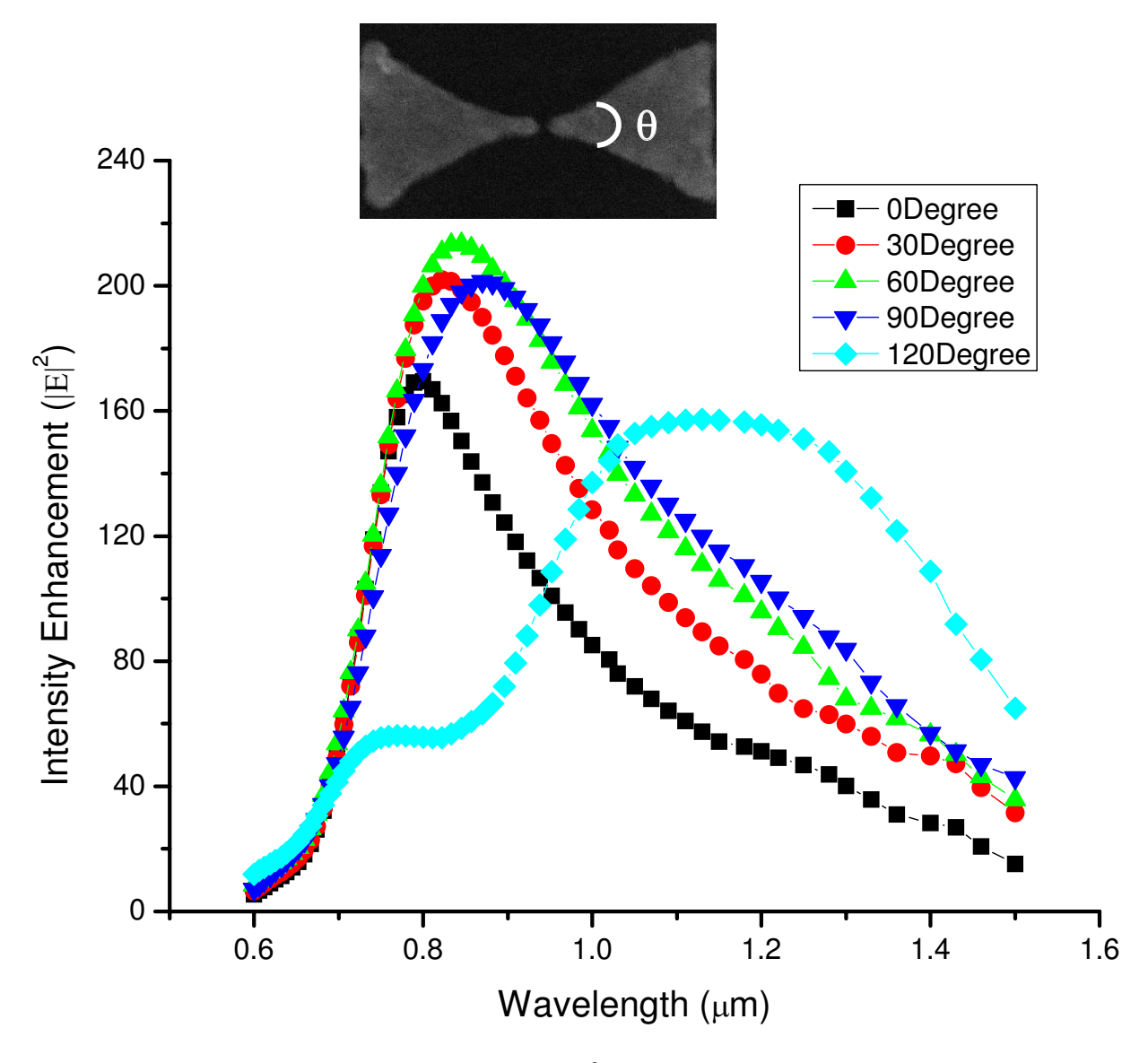


Figure 5.3: E-field intensity enhancement $|E|^2$ spectra of bowtie antennas with tip angles ranging from 0 degrees to 120 degrees. The inset shows a scanning electron microscopy (SEM) image of a bowtie antenna, denoting the tip angle θ .

is smaller than 60 degrees, while it reduces when the tip angle is larger than 90 degrees. In addition, the resonance wavelengths, where the peak intensity enhancements are obtained, redshift with increasing tip angles. Resonance wavelength is proportional to the length of the triangle edges of bowtie antennas, and thus resonance wavelength redshifts as tip angle increases [74]. This can be explained as follows: the two opposite Au/air interfaces in one cross section vertical to the antenna axis are far away from each other in the y direction, thus the local surface plasmon polariton is confined at one Au/air interface and not affected by the opposite one, especially when the cross section is close to the extremity edges. As a result, the bowtie antennas are dominated by isolated surface plasmon polaritons that propagate along the triangle edges; consequently, a standing wave along the triangle edges is generated, with resonance wavelength scales with the length of the triangle edges, therefore redshifts as the tip angle increases [73]. The length of triangle edges of the bowties increase from 185 nm to 272 nm when the tip angle is widened from 0 degrees to 90 degrees, with an increment of only 87 nm. As a result, the cross section along y axis from the tip to extremity edges changes gradually, and thus resonance wavelength differs slightly. The length of triangle edge increases to 383 nm when the tip angle becomes 120 degrees. This major length change causes a rapid change of local cross section, resulting in a major shift of the resonance wavelength.

The simulation results show that larger angle bowtie antennas can cover broader spectrum together with multiple resonances, which are suitable for photodetectors with wide spectrum detection. In our experiment, we were detecting IR signals with single wavelength of 830 nm. Bowtie antennas with a 60 degree tip angle were fabricated to verify the field intensity enhancement of the antennas, since the highest peak field intensity enhancement is obtained at this tip angle, and whose resonance wavelength is close to 830 nm.

5.3 Fabrication and Experimental Results

In order to investigate the performance of bowtie antennas, Au bowties were fabricated on top of a CNT photodetector as depicted in Figure 5.1(a). Photocurrent of CNT photodetector with absence and presence of bowtie antennas was compared so as to examine the field intensity enhancement of the antennas.

5.3.1 Fabrication Process

The fabrication process starts with EBL an Au electrode on top of a quartz substrate. Prior to EBL, the quartz substrate was cleaned in acetone and bombarded with oxygen plasma for 5 minutes to remove residues. A 360 nm-thick layer of poly-methyl-methacrylate copolymer resist (PMMA/MMA) (9% in Ethyl Lactate, from MicroChem Corp.) was spun at 4000 rpm on the substrate, and the sample was baked in a hot plate at $175^{\circ}C$ for 5 minutes to harden the resist and remove solvent. It was followed by spinning a layer of poly-methylmethacrylate (PMMA) (29% in Chlorobenzene, from MicroChem Corp.) at 4000 rpm with a thickness of 130 nm to form a bilayer resist. After that, the sample was baked in a hot plate at 175°C for 30 minutes to remove solvent residue. A thin layer of Au with thickness of 10 nm was deposited on top of the resist to avoid charging effect on the sample during EBL writing. The resist was exposed with the patterned of an Au electrode with width of 400 nm and some alignment mark at an acceleration voltage of 30 kV and an area dose of 290 $\mu C/cm^2$. After exposure, the thin Au layer on the resist was stripped using gold etching for 10 seconds, and then the resist was developed using a 1:3 methyl-iso-butyl-ketone (MIBK) in isopropyl alcohol (IPA) solution for 29 seconds. Following development, the sample was rinsed with DI water, and bombarded by oxygen plasma for 90 seconds to remove residual resist. A 3 nmthick Ti adhesion layer and 40 nm-thick Au layer were deposited using a thermal evaporator. The Au electrode and alignment mark were transferred to the substrate via a lift-off process using acetone (Figure 5.4(a)). Following the same processes with precise alignment, another electrode made by Ti was fabricated on the quartz substrate, with a gap of 1 μm to the Au electrode (Figure 5.4(b)). A droplet of CNT suspension in ethanol alcohol was dispersed at the vicinity to the gap of electrodes, and an AC voltage of 1 Vpp and 10 kHz frequency was applied between the electrodes through the DEP deposition system. With the assistance of an atomic force microscope (AFM) manipulation system, an individual single wall CNT (SWCNT), with diameter of 1-2 nm, was assembled between the electrodes, as shown in the inset of Figure 5.4(c), which is the AFM image of the CNT based photodetector. A detailed deposition process was introduced in [32]. After that, a layer of Si_3N_4 with thickness of 10 nm was deposited on top of the device using plasma-enhanced chemical vapor deposition (PECVD). The PECVD is a uniform deposition process, but Figure 5.4(d) shows the Si_3N_4 only in the region between two electrodes for making the schematic clearer. Eventually, a bowtie antenna with two tip-to-tip equilateral Au triangles was fabricated on top of the Si_3N_4 layer by aligning the gap of bowtie antenna to the SWCNT between two electrodes. The fabrication of the bowtie antenna started with spinning a 100 nm-thick layer of PMMA at 6000 rpm on the device, and the sample was baked on a hot plate at $175^{\circ}C$ for 30 minutes. After that, an Au layer of 10 nm was deposited on top of the device to prevent charging effect. In order to precisely align the antenna to the detector, AFM was used to record the position of the SWCNT for designing antenna layout. The bowtie antenna was layout using single pass lines to reduce proximity effects in order to increase resolution. During EBL, the resist was exposed with a line dose of 0.75 nC/cm to form the pattern of bowtie antenna. After EBL, the thin Au layer was stripped, and the resist was developed using a 1:3 MIBK

in IPA solution for 29 seconds. Following development, a 2 nm-thick Ti adhesion layer and 20 nm Au layer were then deposited using a thermal evaporator. The antenna pattern was transferred to the substrate via a lift-off process Figure 5.4(e).

Figure 5.4(f) shows a 3D AFM image of one of the devices integrating bowtie antenna to a CNT based photodetector. The SWCNT was not located at the center of the axis of two electrodes, thus the position of bowtie antenna was adjusted according to the position of the CNT. AFM images cannot show accurate dimensions in x-y plane due to the image broadening, which is caused by the large radius of curvature of the apex of AFM tips, therefore two triangles of the bowties in the AFM image seems connecting. SEM was utilized to measure the real dimensions of the bowtie antennas. The gap of bowtie antennas (g) was 30 ± 10 nm, the apex width (w) of the triangles was 30 ± 10 nm, length of the bowtie antenna (L) was 400 ± 30 nm.

5.3.2 Experimental Results

Photocurrent measurements were carried out on CNT photodetectors with absence and presence of bowtie antennas so as to investigate the field enhancement of the antennas. An IR laser, which had 830 nm wavelength and polarization in x direction (the axis of bowtie antenna), illuminated on the CNT photodetector that was housed in a testing chamber, and electrical signals were measured using Agilent semiconductor analyzer 4156C.

Photo-response of the CNT photodetector without bowtie antenna was firstly recorded at room temperature by switching the IR laser on and off at 0.2 Hz for several cycles (blue curve of Figure 5.5). Photo-response of the CNT photodetector was measured again after the fabrication of the bowtie antenna (red curve of Figure 5.5). The comparison of photo-responses was based on the amplitude change of photocurrent. Figure 5.5 shows that the

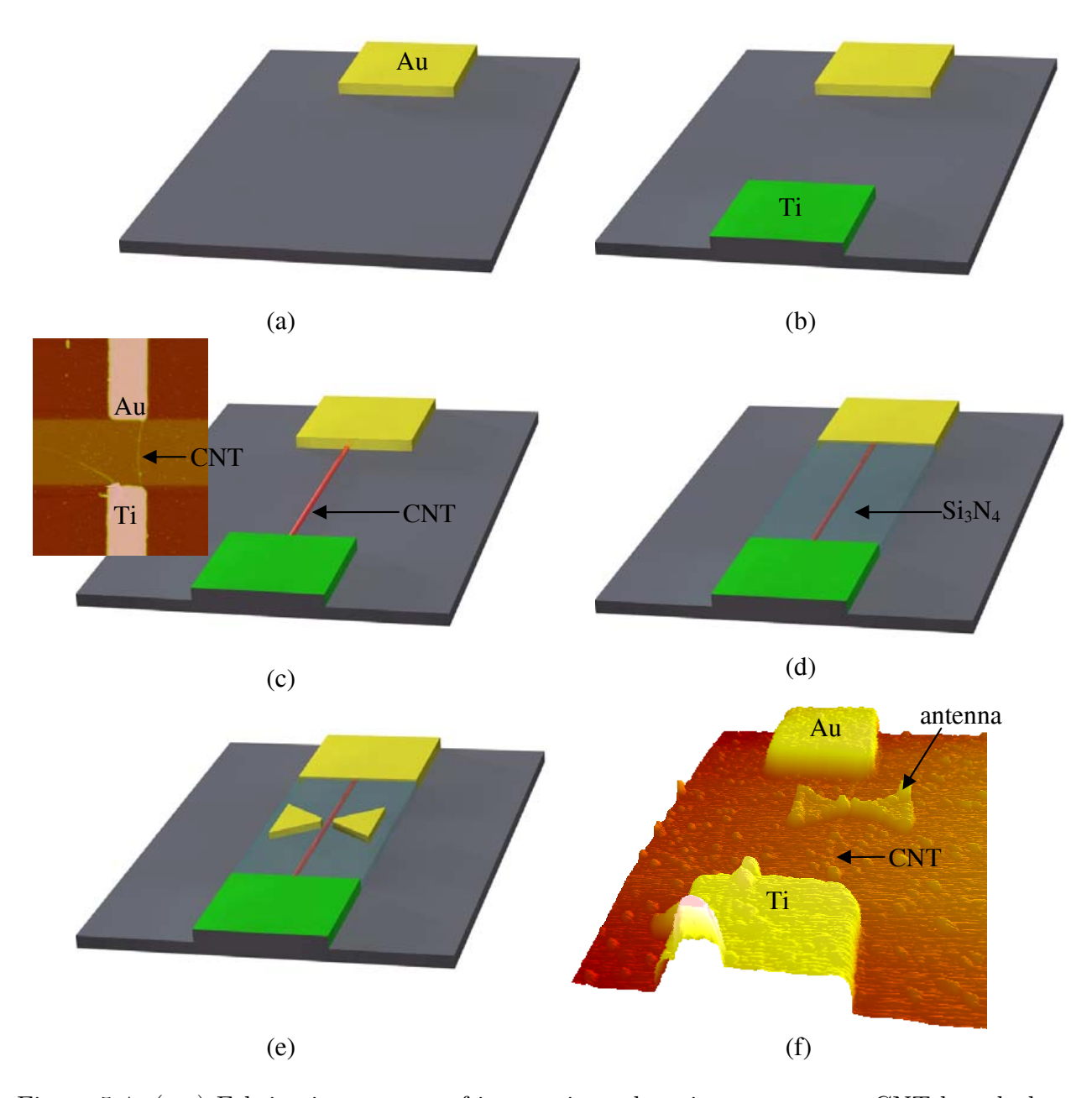


Figure 5.4: (a-e) Fabrication process of integrating a bowtie antenna to a CNT based photodetector. The inset of (c) is an AFM image of a SWCNT bridging a Ti and an Au electrode. (f) A 3D AFM image of the device.

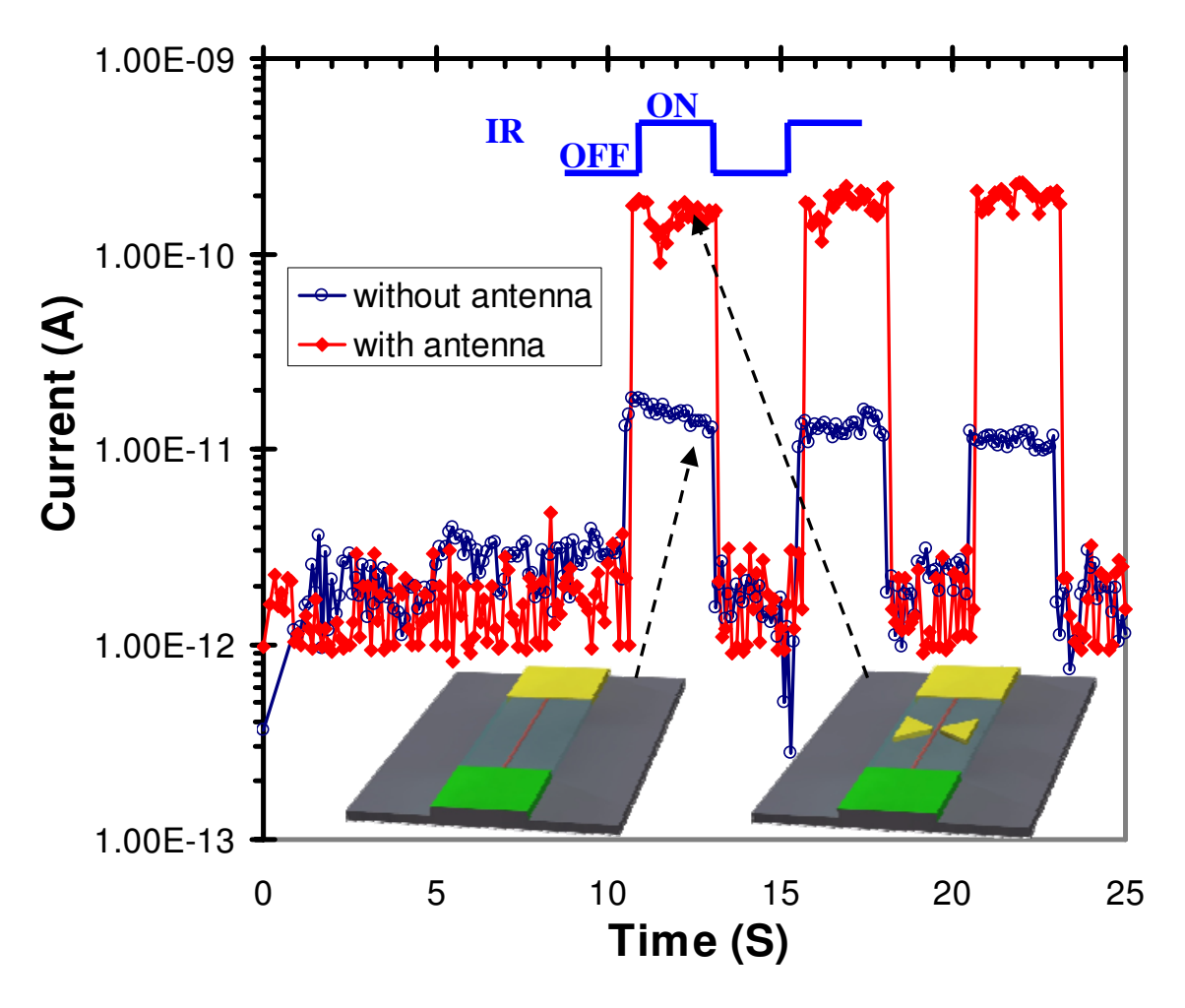


Figure 5.5: Photo-responses of the CNT based photodetector without and with bowtie antenna by switching IR laser on and off at 0.2 Hz.

dark current was 2×10^{-12} A at the absence of IR illumination, and the current was increased significantly upon light illumination because of the photons generated electron and hole pairs within the CNT, which were separated in the Schottky barrier to produce photocurrent. The current dropped to the dark current when the IR laser was turned off. The reproducibility of the photo-response was excellent. The photocurrent for CNT photodetector without antenna was 1.5×10^{-11} A, and it was increased to 1.9×10^{-10} A after the fabrication of the bowtie antenna, with a photocurrent enhancement of 12.67 times.

The bowtie antenna functions as a plasmonic lens to funnel light into the CNT, which

has a size much smaller than the gap of bowtie antenna. Hence, the area of detector material (physical cross section) and absorption probability did not change with the absence or presence of the antenna. With the presence of bowtie antenna, the photon energy density on the detector material was enhanced due to sub-wavelength near field confinement. It has been defined that the absorption cross section of the detector is the total light power absorbed by detector material normalized by the incident photon flux [63]. Therefore, calculation of relative energy intensity difference on the CNT body at absence and presence of antenna will directly reflect the photocurrent enhancement.

The field intensity increment on the CNT can be calculated by integrating the E-field intensity along the CNT by $I = \int |E(y)|^2 dy$ (Figure 5.2(a)), since the depletion region of the asymmetric CNT photodetector extended to the whole CNT. In other words, the photocurrent enhancement was caused by the E-field intensity increment on the CNT. Without the nano-antenna, the total field intensity on the CNT equal to 10^{-6} V because Ex(y)=1 V/m and $y=1 \mu m$. The field intensity distribution with the antenna was calculated by using the parameters that were the same as fabricated device and experimental setup (d=30 nm, w=30 nm, L= 400 nm, t=10 nm, θ =60 degrees, and radiation wavelength=830 nm). By integrating the field intensity along the y axis between two electrodes (where the CNT located in Figure 5.2(a)), the field intensity was enhanced to 1.48×10^{-5} V, with a field enhancement of 14.87 fold. Therefore, the photocurrent enhancement is in good agreement with the simulation. Differences are attributed to geometry differences between the actual antennas and the simulation model, and some loss were occurred in the antennas due to edge and surface roughness.

In order to validate that the photocurrent enhancement was caused by the light confinement of the nano-antenna, rather than the contact condition change during fabrication, I-V

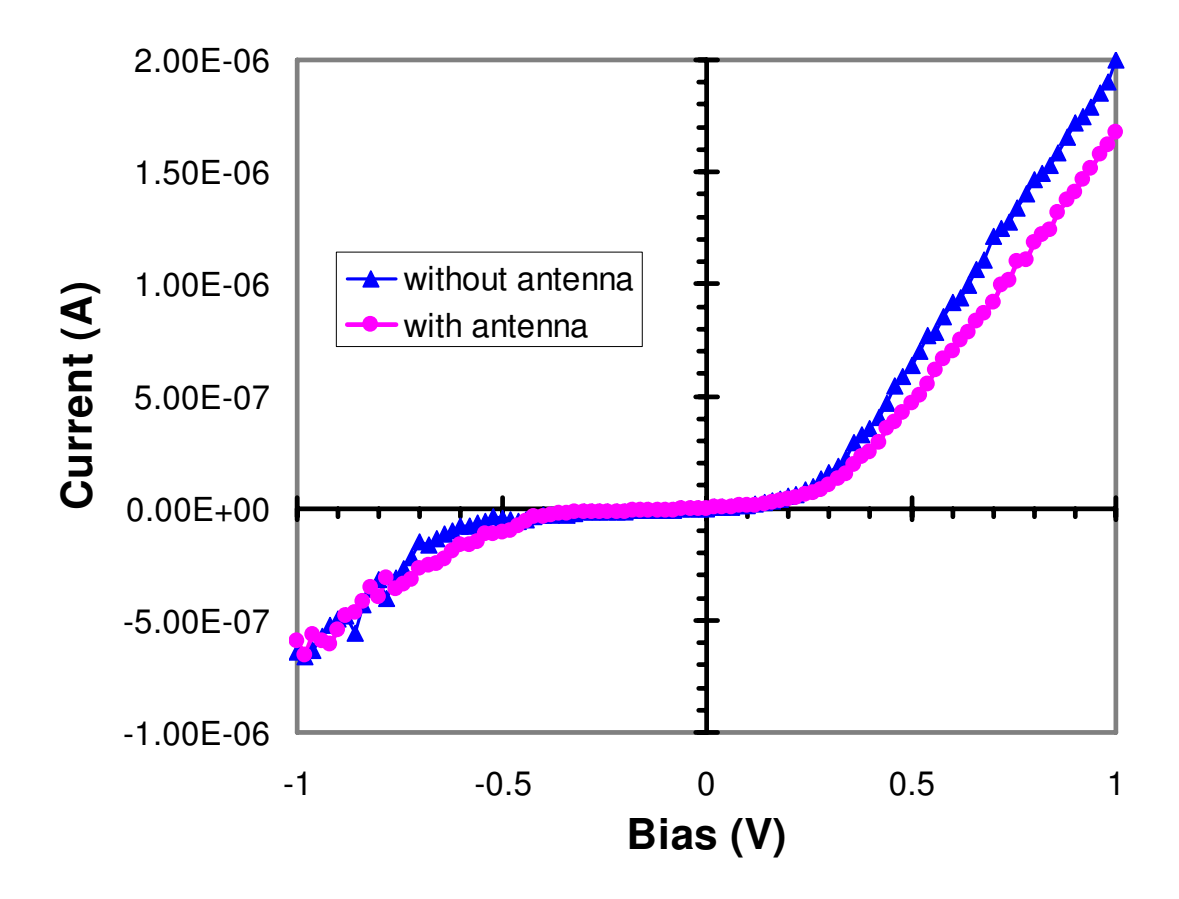


Figure 5.6: I-V characteristics of the CNT photodetector without and with the bowtie antenna.

characteristics of the photodetector without and with antenna were measured and shown in Figure 5.6. The I-V characteristics showed current rectifying at low voltage, implying the existence of Schottky barriers. In addition, the bias-dependent current of the CNT photodetector with absence and presence of nano-antenna were almost identical, which indicated that the contact condition did not change with the fabrication of the nano-antenna, since electrical signal was extremely sensitive to contact condition. This verifies that the photocurrent increment was caused by field intensity enhancement from the bowtie antenna.

5.4 Chapter Summary

The bowtie antenna functioned as a plasmonic lens that funnel confined light onto a CNT based photodetector. The design of bowtie antennas integrating to the CNT based photodetectors was studied. The E-field intensity enhancement of bowtie antennas with a small gap located on top of the asymmetric CNT based photodetector was calculated. It was shown that the peak field intensity of the antenna was exponentially decreased with the distance between the antenna to the CNT based photodetector. The resonance wavelength of the bowtie antenna redshifts with increasing tip angles. A fabrication process was developed to integrate the bowtie antenna with the CNT detector. It should be noted that the 1D CNT detector is perfectly matched with the bowtie antenna, since the diameter of CNTs is in the same scale as the gap of the bowtie antenna. The experimental results agreed well with the simulation by measuring photocurrent enhancement. The nano-antenna will become an important component to the nano-scale photodetectors to overcome the diffraction limit.

Chapter 6

Photonic Crystal Cavity

It has been demonstrated that optical antenna can confine light into sub-wavelength volume to improve the fill factor of CNT based photodetectors. However, the fill factor of antenna/CNT photodetector is still small, limited by the small absorption area of optical antennas. In order to address this problem, a photonic crystal cavity, using photonic crystal with a point defect made of HfO₂, was fabricated on top of the CNT photodetectors in order to enhance the local photon density. By drilling holes, with size of the scale of light wavelengths, in the parylene slab, the periodic change of reflective index forms photonic crystal. Replacing one of the holes with HfO₂ as a point defect, most of the light will be trapped in this defect. A photonic crystal was designed to concentrate the infrared light with 1064 nm wavelength, and 91 % of the light can be confined into the HfO₂ defect. The fabrication process of this photonic crystal cavity is introduced, and photocurrents of a CNT based photodetector are compared under the circumstance of without and with photonic crystal. It is found that the photocurrent is enhanced about 5 times after the fabrication of photonic crystal cavity.

6.1 Introduction of Photonic Crystal Cavity

The outstanding performance of CNT photodetectors, inherited from the nano-scale size of CNTs, which, however, cause low absorption due to the small absorption area of the CNT

photodetectors, since diameters of CNTs (including SWCNTs and MWCNTs) are normally less than 100 nm. In other words, the CNT detectors have low fill factor. In order to increase the fill factor, light needs to focused into a small region that has size comparable to the detectors. Traditional lens is difficult to focus light into this miniature size due to light diffraction and lens imperfection. Motivated by this challenge, a parylene photonic crystal slab with a point defect made of HfO₂ was designed to integrate with a CNT photodetector.

Photonic crystals are artificial optical materials with periodically structured dielectrics of alternative reflective indexes to control the propagation of light. Photonic crystals has periodic structure that is analog to solid state crystals, but with dimensions of the order of optical wavelengthes. As a result, photonic crystal can guide light with frequency bands and frequency bandgap, in the same fashion as atomic lattices conducting electrons with energy bands and bandgap. If the optical frequency falls in frequency bands, a photonic crystal becomes a perfect optical conductor, which can be employed to guide the light propagation. On the other hand, when the photon frequency falls in a photonic bandgap, a photonic crystal acts like an optical insulator, which can be used to build micro-scale optical mirrors, resonant cavities, and waveguides [75].

When the symmetric arrangement of the photonic crystal was broken, it operates in defect modes. Two most basic defects are point defects [76], which remove a single hole of the photonic crystal, and line defects [77], which remove a row of dielectric holes in the symmetric structure. Photonic crystal with a point defect, which was termed photonic crystal cavity, can confine light in the defect region, functioning like a lens [78]. Fill factor of CNT photodetector can be highly improved if the defect of photonic crystal cavity aligned to the absorption area of the CNT photodetectors.

6.2 Design and Fabrication

An AFM image of a photonic crystal cavity integrating with a CNT photodetector is shown in Figure 6.1. A 2D photonic crystal slab made by parylene/air resides on top of a CNT photodetector with a HfO_2 defect located on one of the contacts between CNT and electrode. The photonic crystal cavity we used is photonic crystal based quantum resonance cavity. When the resonance wavelength of the photonic crystal is close to the wavelength of light, light will be trapped into the defect, as shown in Figure 6.1(c).

3D photonic crystals have periodic structures in three coordinate axis, similar to the real solid state crystal structures [79]. However, the fabrication of 3D photonic crystal involves complicated fabrication processes, in particular, to integrate with CNT photodetectors.

2D photonic cavity can accomplish same function as a micro-lens to confine light in the point defect, while with simpler structure and fabrication process. The 2D photonic crystal cavity consists of a parylene slab with air holes for total internal reflection of the light in the vertical direction, and a 2D photonic crystal is to provide lateral localization within the point defect. Traditional optical cavity is created by removing an air hole (point defect) in the photonic crystal, while a HfO₂ was utilized as point defect in this design. The refractive index of HfO₂ (1.90 [80]) is higher than parylene (1.62 [81]), which is higher than air (1.00), thereby total internal reflection will be more likely to occur between the HfO₂ and parylene, resulting in more light confining in the defect region.

As mentioned above, the photonic crystal acts as optical insulator when optical frequency falls in the bandgap frequency. If the optical frequency is within the bandgap frequency of the 2D photonic cavity, light illuminating on the photonic crystal has nowhere to go except the point defect, functioning as confining all the light into a small region. Therefore, proper

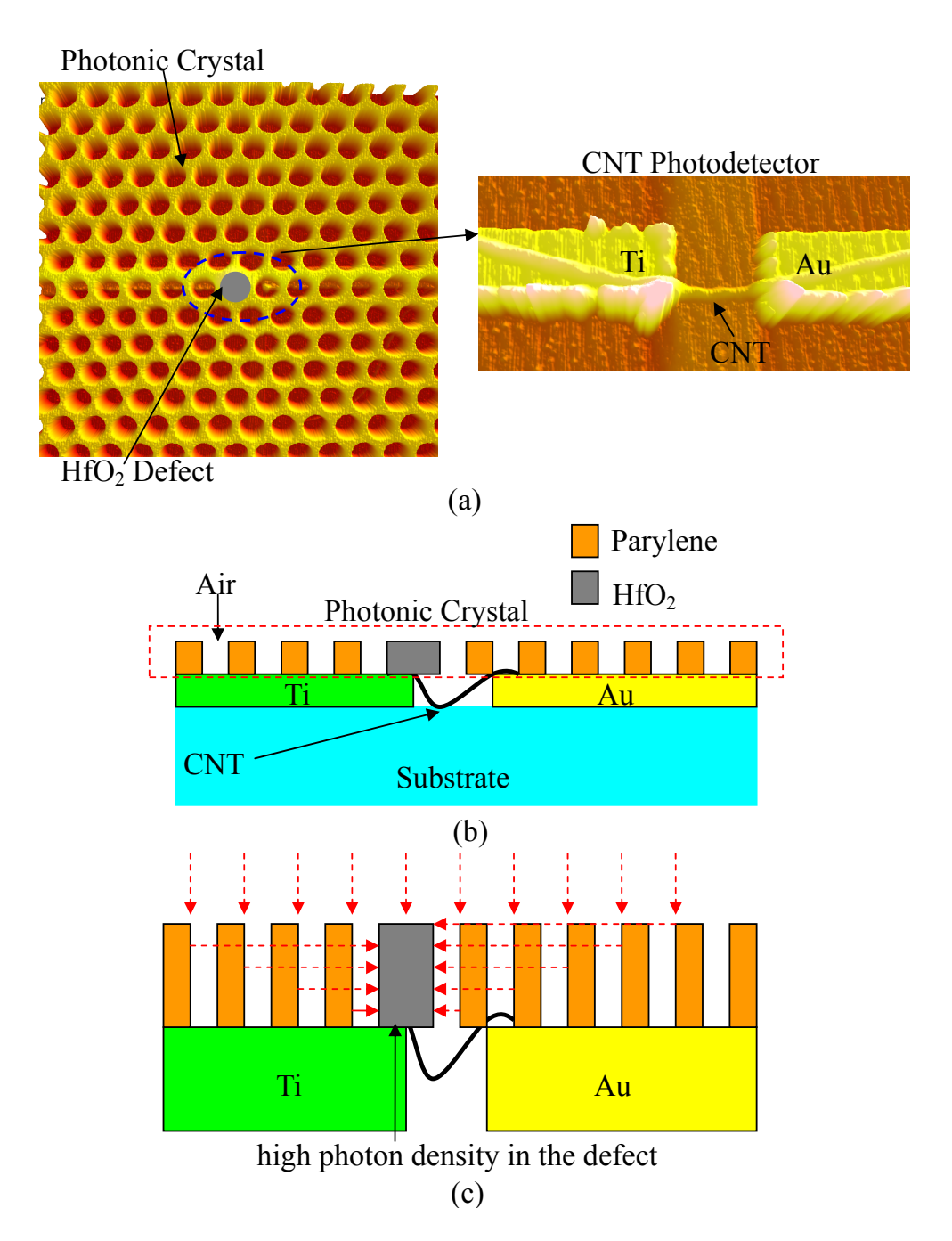


Figure 6.1: (a) AFM image of a parylene photonic crystal with a HfO₂ defect on the top of a CNT detector. (b) Cross section of the device. (c) The working principle of the photonic cyrstal cavity by confining the light radiating on photonic crystal into the defect.

dimensions of the photonic crystal need to be found in order to direct light into the defect.

A laser with 1064 nm wavelength, corresponding to 282 THz, was used to test the CNT photodetectors. By simulating the dispersion relationship of the photonic crystal, it was found that the middle of bandgap frequency equal to 282 THz when the lattice constant (the distance between air holes) a= 509 nm, and diameter of air hole d= 407 nm.

The electric field distribution of the photonic crystal cavity with 9×9 air holes was simulated. When the defect material of photonic crystal cavity is parylene, 31 % light focuses into the defect. The energy inside the defect increase to 91 % when the defect became HfO_2 . Figure 6.2(b) shows the electric field distribution of the photonic crystal cavity with a HfO_2 defect: most of the electric field concentrates in the defect area.

The fabrication process began with fabricating Ti and Au electrodes with a insulating gap of $0.5 \ \mu m$ on top of a quartz substrate by EBL, thermal evaporation, and lift-off. After that, a single MWCNT was deposited between the electrodes using the dielectrophoresis (DEP) deposition system assisted by the AFM manipulation system [27]. A single MWCNT connecting to two electrodes is shown in Figure 6.3(a). It is followed by fabricating an HfO₂ cylinder with $0.5 \ \mu m$ -diameter on top of a contact between Ti and CNT by EBL, e-beam evaporation, and lift-off, as shown in Figure 6.3(b). A layer of parylene will be deposited on the device, and air holes will be drilled by plasma etching after EBL to define the dimensions of the air holes, as shown in Figure 6.3(c).

6.3 Experimental Results

The testing system consists of a chamber that houses the CNT photodetector, an IR laser of 1064 nm wavelength, and Agilent 4156C semiconductor analyzer. The photo-response in

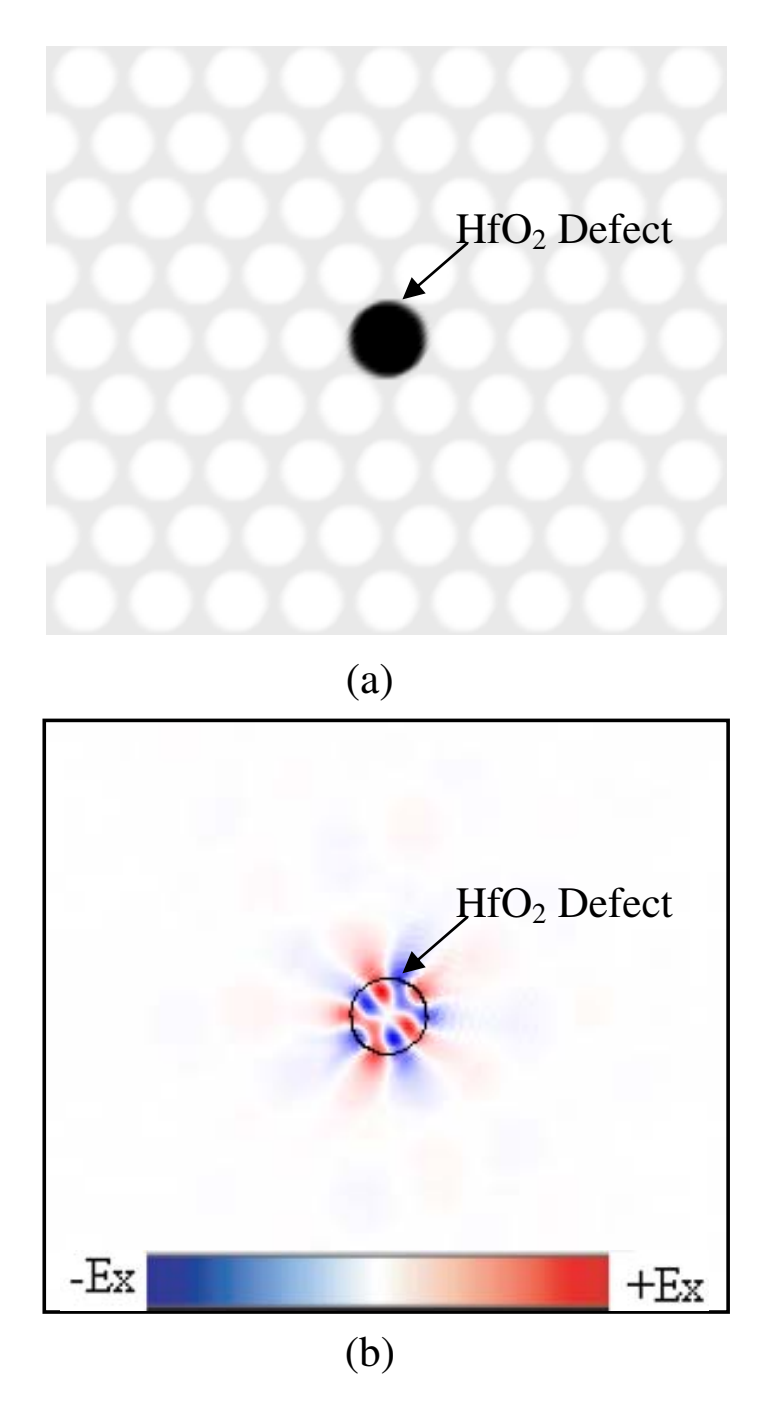


Figure 6.2: (a) The simulation geometry of the photonic cavity with parylene slab and a HfO_2 defect. (b) Electric field distribution of a 1064 nm IR light in the photonic cavity, most of the electric field is confined within the point defect.

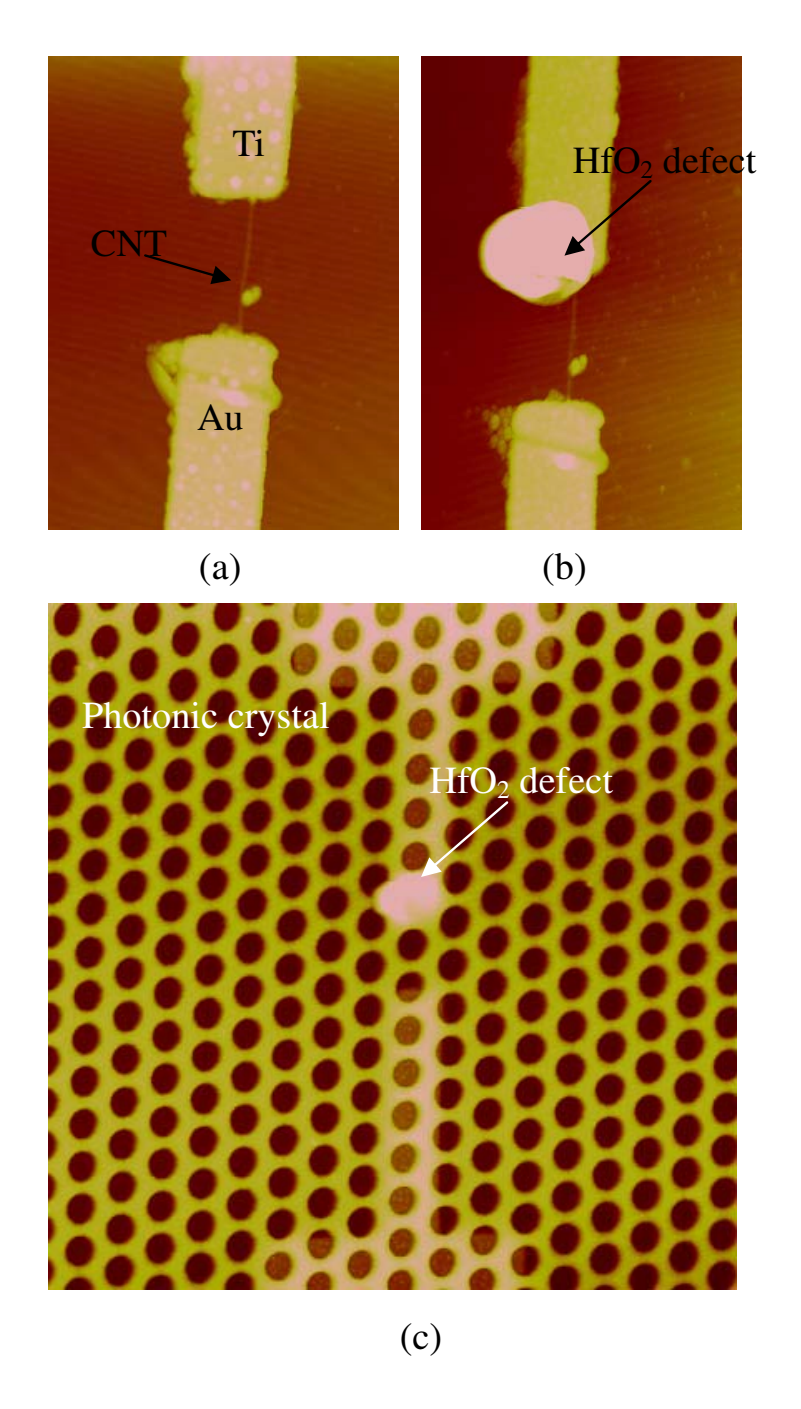


Figure 6.3: Fabrication process of the testing device (a) CNT Schottky photodiode, (b) CNT photodetector with a HfO_2 defect,(c) Photodetector with photonic crystal and a HfO_2 defect.

terms of photocurrent with absence of photonic crystal was firstly measured using the semiconductor analyzer by focusing the IR laser on the CNT photodetector. Temporal photoresponses of CNT detector with absence and presence of photonic crystal cavity were measured, showing the photocurrent enhancement of about 5 times after adding photonic crystal cavity. However, the photocurrent enhancement may caused by the misalignment between laser and CNT photodetector in two measurements, since the size of laser spot used in our experiments is larger than the CNT detector, and photocurrents were recorded when highest photocurrent was obtained after aligning laser spot with CNT detector. In order to have a better understanding of the photonic crystal cavity as a micro-lens, scanning photocurrent images of the CNT detector with and without photonic crystal cavity were studied.

Figure 6.4 illustrates the setup to obtain scanning photocurrent images. Laser spot scans around the CNT photodetector along the scanning path as shown in Figure 6.4. The scanning photocurrent image of a CNT photodetector was firstly obtained without a photonic crystal cavity. After that, a photonic cryatal cavity made from parylene slab with a HfO₂ defect was fabricated by aligning the point defect on top of the detector. The photocurrent distribution of the CNT detector with photonic cavity was recorded by scanning the laser around the detector.

A 3D mapping of position dependent photocurrent was obtained, as shown in Figure 6.5. Photocurrent was less than 1 nA without the photonic crystal cavity in a $20\times20~\mu m^2$ area. After the fabrication of the photonic crystal cavity, photocurrent was enhanced to around 5 nA in the same area, indicating that the photonic crystal cavity increases the light intensity approximately 5 times within the area of the detector. This result shows that photonic cavity functioned as an effective micro-lens to increase the interacting of CNT photodetector and light.

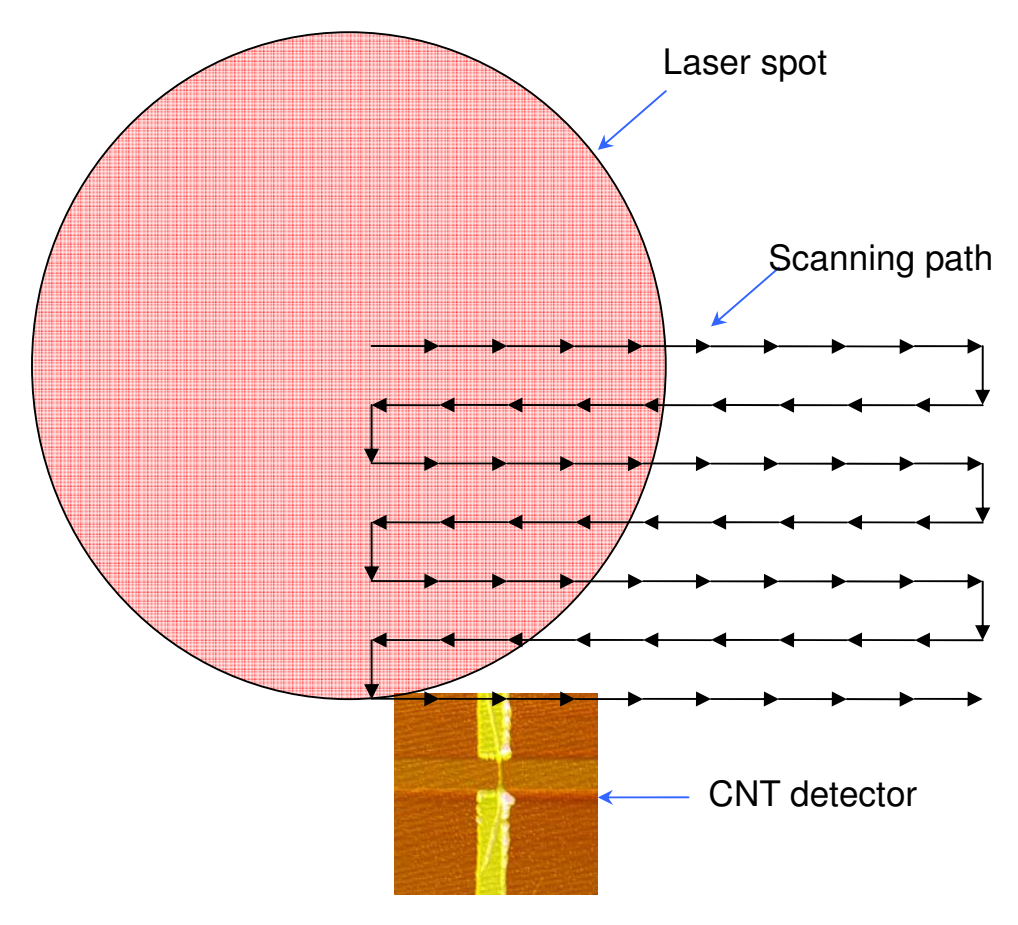


Figure 6.4: Experimental setup to obtain scanning photocurrent images.

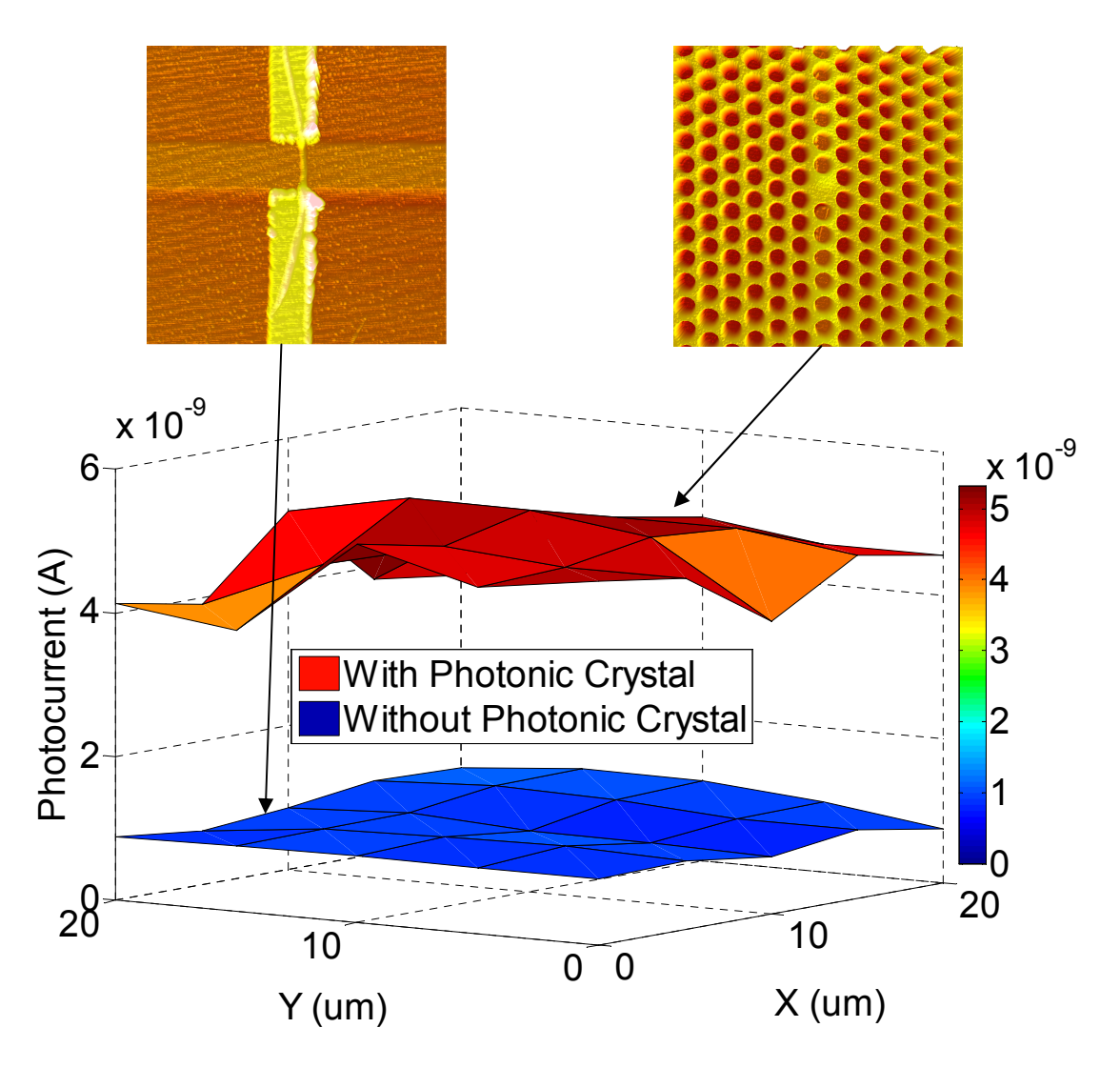


Figure 6.5: Scanning photocurrent images of the CNT photodetectors without and with photonic crystal cavity. The insets are the AFM images of detectors without and with photonic crystal cavity.

6.4 Chapter Summary

In summary, a photonic crystal cavity with a HfO_2 defect was demonstrated to improve the performance of the CNT photodetectors. Optical antenna has demonstrated as a plasmonic lens to focus light into a sub-wavelength volume, resulting in improved fill factor. However, the absorption area of antennas is limited. In order to further improve the fill factor, a photonic crystal cavity was utilized as a micro-lens to focus light into CNT photodetector. The photonic crystal cavity comprise of a parylene slab with air holes and a HfO_2 point defect, which is placed on top of a CNT photodetectors. The simulation results show that about 91 % of light in a area of 9×9 air holes can be confined into the defect, and as a result, photocurrent was increased 5 folds with the presence of the photonic crystal cavity.

Chapter 7

Infrared Sensing Systems Using a

Single Nano-photodetector

We have demonstrated a 3×3 array of CNT photodetectors. However, it is difficult to manufacture a megapixel count focal plane array as in conventional camera structure, because IR detectors were assembled by bottom-up approaches.

In this chapter, we will introduce a novel IR sensing system, which enables utilizing the promising performance of 1D-photodetectors, and overcoming the difficulties to obtain high resolution and efficient IR images. The sensing system is constructed based on an emerging compression theory: compressive sensing. A given image can be compressed if the image is sparse or can be sparsely represented in another basis, for example piecewise smooth images are sparse in wavelet basis. Traditional compression algorithms perform compression after sampling, while compressive sensing allows image compression during sampling so as to reduce the number of measurements and data storage capacity [82] [83].

Our sensing system mainly consisted of a digital micromirror device (DMD), a CNT photodetector, a high speed readout system, and an image reconstruction computer. Instead of projecting IR images onto the focal plane array of image sensors, IR images were projected onto a DMD, which generates measurement matrices according to compressive sensing algorithms [84]. The images are compressively sampled using a single CNT photodetector via

recording the linear projection of IR images onto the measurement matrix. IR images are recovered through a compressive sensing reconstruction algorithm based on the measurement results. The experimental results show that the new imaging system can achieve the superb performance enabled by CNT based IR detectors, and, at the same time, overcame its difficulties to obtain high resolution and efficient imaging.

7.1 Compressive Sensing Theory

The core of our IR sensing system is compressive sensing theory. In this section, the basics of compressive sensing will be briefly reviewed. A recent complete introduction of this topic can be found in [85]. Compressive sensing is a new paradigm for signal sampling, which has found a wide spectrum of applications in imaging [86], control and robotics [87] [88], geophysical data analysis [89], communication [90], and etc. Traditional sampling approaches require the sampling rate to be at least twice the maximum frequency of the signals according to the Nyquist-Shannon sampling theorem. Nevertheless, compressive sensing shows that the sampling rate can be significantly reduced if the signal satisfies general sparse conditions. Specifically, this new sensing paradigm directly samples the signal in compressed form, and then recovers the original signals by advanced optimization or greedy algorithms [91].

The general compressive sensing theory can be summarized as follows. Assume an unknown high dimensional signal $x \in \mathbb{R}^n$ is projected to lower dimensional measurements $y \in \mathbb{R}^m$:

$$y = \Phi x \tag{7.1}$$

with $\Phi \in \mathbb{R}^{m \times n}$ (m < n) being the measurement matrix. Then the unknown x can be recovered from y, if x and Φ satisfy certain conditions. In what follows, the conditions of both x and Φ for successful recovery will be briefly described.

One condition for recovery is that the original signal is sparse (or approximately sparse) or has a sparse representation in some basis. A vector $x \in \mathbb{R}^n$ is S-sparse if the support, i.e., the number of nonzero elements, of x is at most S. Denote the set of all the S-sparse vectors by Ω_S . Formally,

$$\Omega_S = \{ x \in \mathbb{R}^n : ||x||_0 \le S \}$$

where $||x||_0$ denotes the support of x.

In some cases, $x \in \mathbb{R}^n$ may not be sparse in its original form but sparse in some orthonormal basis. Let Ψ be such a basis. In this case, x can be expanded in Ψ as: $x = \Psi \tilde{x}$ with $\tilde{x} \in \Omega_S$. The compressive sensing can be rewritten as:

$$y = \Phi x = A\tilde{x} \tag{7.2}$$

with $A = \Phi \Psi$ being the new measurement matrix. Without loss of generality, we will assume the original signal is sparse (or approximately sparse) and use x to represent it in the following discussion.

In general, the exact S-sparse cannot be achieved in real-world signals, but they can be well approximated by an S-sparse signal. The best S-sparse approximation for a vector $x \in \mathbb{R}^n$ is a vector $x_S \in \mathbb{R}^n$ by retaining the largest S elements in x and setting the other elements to zero.

Another condition for recovery is that the measurement matrix needs to satisfy the restricted isometry property (RIP), which is defined as follows:

Definition 1. A matrix $A \in \mathbb{R}^{m \times n}$ with m < n satisfies the RIP of order S if there exists a constant $\sigma_S \in (0,1)$ such that for any $x \in \Omega_S$, we have

$$(1 - \sigma_S)||x||_2^2 \le ||Ax||_2^2 \le (1 + \sigma_S)||x||_2^2 \tag{7.3}$$

Note that measurement matrix can follow other conditions, such as spark [92], null space property [93], or coherence [92], but the RIP is the most powerful one because it can deal with the case when the measurements are corrupted by noise.

With the above two conditions, we can discuss the original signal recovery. To find the sparsest solution, the recovery problem can be stated as:

$$\min ||\hat{x}||_0 \quad \text{subject to} \quad A\hat{x} = y \tag{7.4}$$

 \hat{x} is the recovered signal. The above problem, however, is NP-hard. As an alternative, the l_1 minimization can be used:

$$\min ||\hat{x}||_1 \quad \text{subject to} \quad A\hat{x} = y \tag{7.5}$$

Using the l_1 minimization, the recoverability is guaranteed by the following theorem:

Theorem 1 (Candés [94]). Suppose the matrix A satisfies the RIP of order 2S with constant $\sigma_{2S} < \sqrt{2} - 1$, then the solution to Eq. (7.5) satisfies:

$$||\hat{x} - x||_2 \le C||x - x_S||_1/\sqrt{S} \tag{7.6}$$

with C a constant related to σ_{2S} .

The theorem suggests that the error between the recovered signal and the original signal is bounded by the error between the original signal and the best S-sparse approximation. Note that the noise measurement can also be handled under the RIP condition [95], which will not be discussed here.

With the above theorem for recoverability, the next question is how to design the measurement matrix satisfying the RIP condition. The goal is to recover the original signal with the least measurements. In other words, we need to design the measurement matrix $A \in \mathbb{R}^{m \times n}$ such that m is smallest for fixed n. Although it was difficult to design deterministic matrix for RIP, various random matrices were shown to satisfy the RIP with high probability. If the entries in the matrices are chosen according to Gaussian [96], Bernoulli [95], or sub Gaussian

distribution [97], then the matrices satisfy the RIP with very high probability if:

$$m \ge D \cdot S \log(n/S) \tag{7.7}$$

where D is also a constant [97]. Note that the random matrices discussed above follows the so-called universality. In fact, if a random matrix Φ satisfies the RIP, then the matrix $\Phi\Psi$ will also satisfy the RIP with high probability. In other words, we can design the random measurement matrices Φ without considering the sparsity of the original signal [95].

The final piece of compressive sensing is the recovery algorithm, i.e., the algorithm to solve Eq. (7.5). There are many algorithms to solve the problem, which can be classified into convex optimization, greedy algorithm, or combinatorial algorithms. A detailed summary of those algorithms can be found in [98].

7.2 Sensing System Architecture

Prior to the discussion of the sensing system, I will give a brief introduction of the DMD. DMD in our system is one of the most important components to accomplish compressive sensing algorithm. Traditional DMD is the essential component of digital light processing (DLP) projection technology, controlling light propagation by a large array of electrostatically actuated micromirrors. Figure 7.1(a) shows a scanning electron microscopy (SEM) image of nine micromirrors in a DMD. Each micromirror is square in shape, and stands closely to adjoining micromirrors with a small gap, implying a high fill factor.

In our imaging system, DMD from Texas Instruments (TI) was used to generate a measurement matrix according to compressive sensing. Each individual micromirror can be

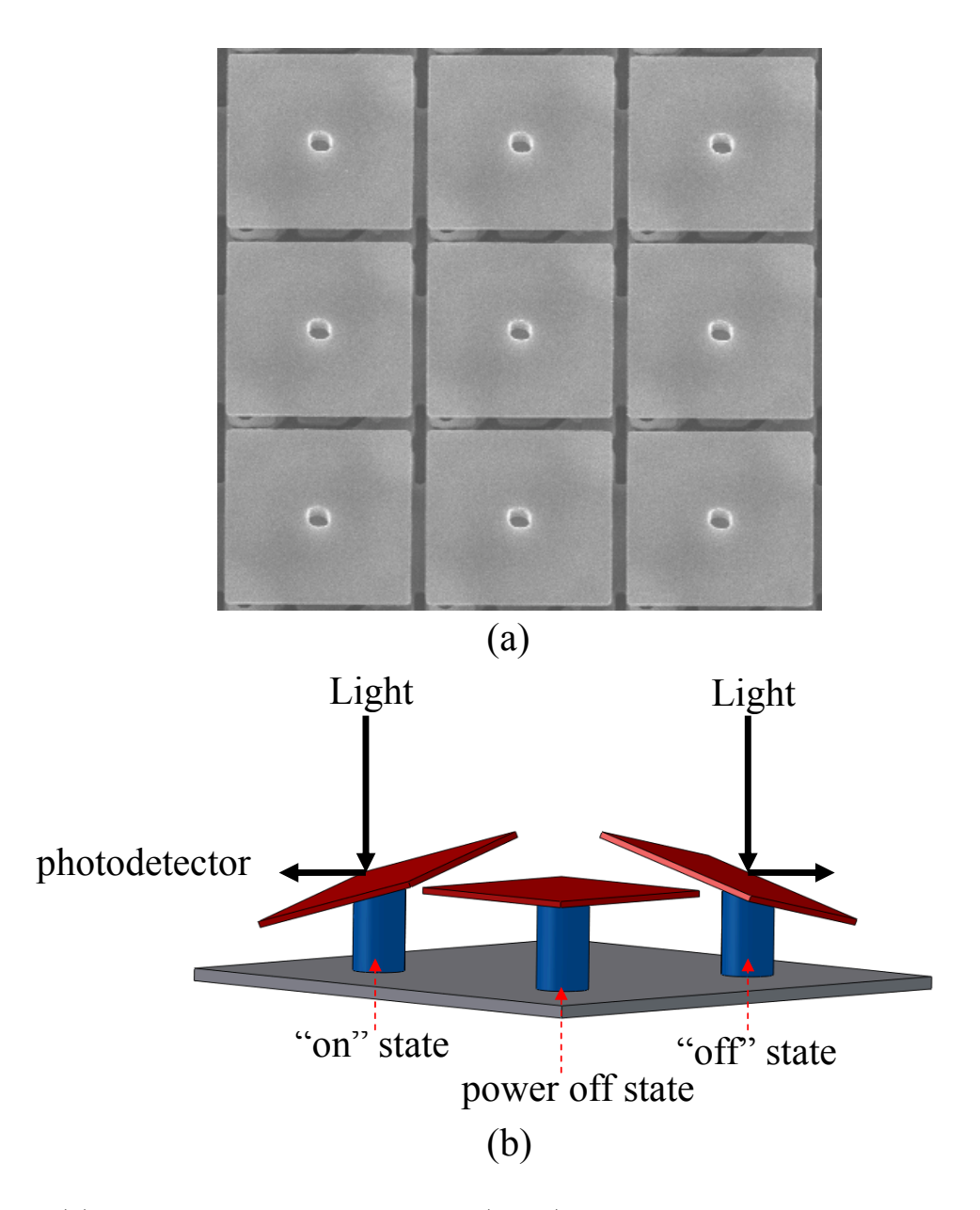


Figure 7.1: (a) Scanning electron microcopy (SEM) image of an array of micromirros in the DMD. (b) Three status of the micro-mirrors: "on", "off", and power-off states.

poised into two different angles (-10 degree and +10 degree), which define the "on" and "off" states of the micromirrors. In the "on" state, light irradiated on a micromirror is oriented to the CNT photodetector (the left mirror of Figure 7.1(b)). In the "off" state, the light that fell onto a micromirror is reflected elsewhere (the right mirror of Figure 7.1(b)). When the power for DMD is off, the micromirror stays horizontal without a rotation (the middle mirror of Figure 7.1(b)). By controlling the states of each micromirror, the DMD forms a specific measurement matrix.

The structure of the IR sensing system is built upon the compressive sensing theory introduced in the previous section. Figure 7.2 depicts the system setup using a single pixel CNT photodetector as its image sensor.

IR images were directed onto a DMD through a set of lenses. The IR images on the DMD represents the original signal x in Eq. (7.1) $(x \in \mathbb{R}^n, n)$ is the number of image pixels). The DMD generated patterns according to a measurement matrix Φ ($(\Phi \in \mathbb{R}^{m \times n})$) so as to compress the IR images. Each pattern on the DMD comprised n pixels, thus m different patterns were generated to construct the measurement matrix Φ . The compressed IR images were reflected to another lens, which focused all the light to a CNT photodetector. The IR signal arrived at the CNT photodetector represents the linear projection of the images onto the measurement matrix, which can be considered as the inner product of IR images x and each row vector in the measurement matrix Φ . The photocurrent generated in the photodetector was recorded by a fast readout system integrating with a charge integrator, an analog-to-digital converter (ADC), and a data acquisition (DAQ) card [99] [100]. The amplitudes of photocurrent represent the values of y in Eq. (7.1) ($y \in \mathbb{R}^m$, m is the number of measurements). The IR images were recovered by a personal computer. It should be noted that compressive sensing makes m < n; therefore, the IR images x were compressively

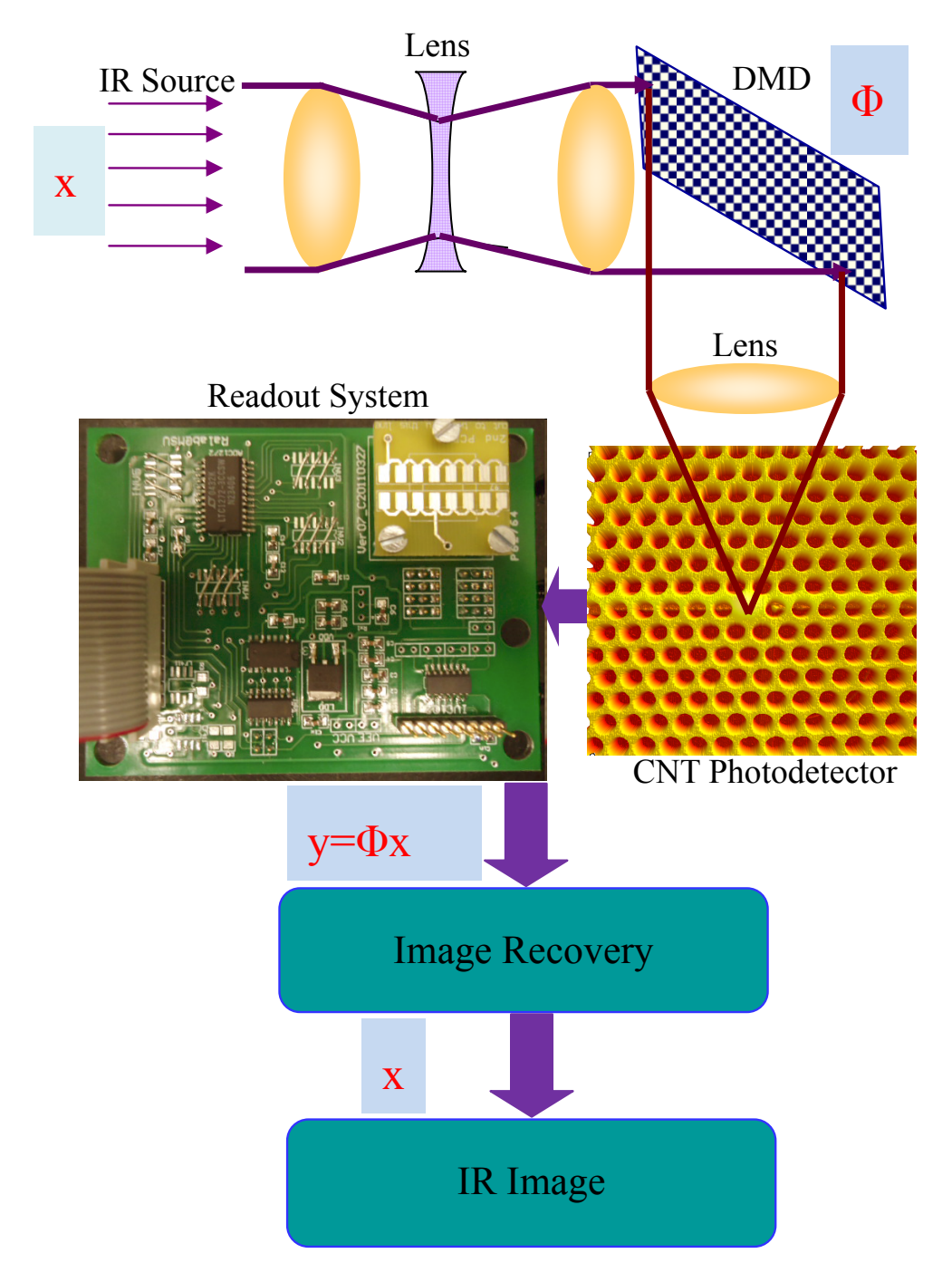


Figure 7.2: The setup of compressive sensing based imaging system using a CNT detector with photonic cavity and DMD.

sampled into the y. Based on the measurement results y and the designed measurement matrix Φ , the original signal x can be recovered using an image reconstruction algorithm.

7.3 Experimental Results

For the imaging experiment, the laser source was projected onto the DMD to form an IR image x. DMD generated a measurement matrix Φ according to random Bernoulli distribution, which had high probability of satisfying the RIP condition [95]. Each random pattern is a row of the measurement matrix, and m Bernoulli random patterns were used to capture an IR image. As a result, each measurement result from the CNT photodetector obtains the inner product between an IR image and a row of the measurement matrix. After m times of measurements, one image x is compressively sampled into the measurement results y. The image was recovered via minimizing the total variation norm (TV-norm). Minimizing such a norm can make the intensity difference between neighboring pixels sparse, thus smoothing the images. Formally, let x_{ij} be the pixel intensity in the i-th row and j-th column in the image x. The intensity differences in the horizontal and vertical directions (D_{ij}^h) and D_{ij}^v

can be defined respectively as follows:

$$D_{ij}^{h} = x_{i+1,j} - x_{ij}, \quad D_{ij}^{v} = x_{i,j+1} - x_{ij}$$
 (7.8)

The total variation for the image x is then defined as

$$TV(x) = \sum_{i,j} \sqrt{D_{ij}^{h^2} + D_{ij}^{v^2}}$$
 (7.9)

Therefore, the image recovery problem can be defined as:

$$\min ||TV(\hat{x})||_1 \quad \text{subject to} \quad A\hat{x} = y \tag{7.10}$$

Note that for consistence, the above \hat{x} can be considered as the vector form of the image matrix x.

The DMD has 1064×768 micromirrors. Each micromirror is square in shape with a dimension of $12~\mu m \times 12~\mu m$. We first obtained IR images with a low resolution of 30×30 pixels to adjust the alignment and focus of the system. Traditional cameras require 900 measurements in order to obtain a 30×30 image, while our imaging system can recover the image with only 500 measurements [84]. Images of 30×30 pixels correspond to 1064×768 micromirrors, thus each pixel contains 908 micromirrors. Note that the DMD is not square in shape, thus each pixel in the image is a rectangular shape.

The imaging system was used to capture a higher resolution image of a rectangular IR

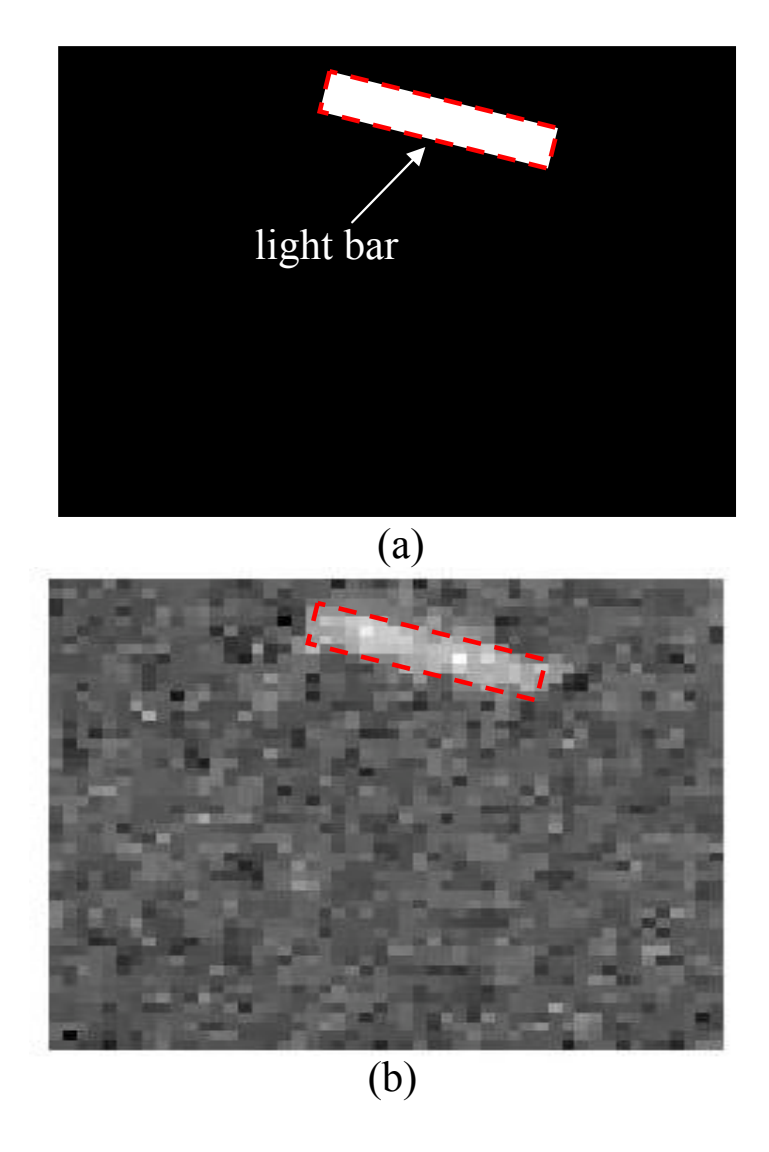


Figure 7.3: (a) The position and orientation of the rectangular light bar on the DMD. (b) The image of 50×50 pixels recovered by our imaging system, highlighted by a red rectangle.

light bar. The position, orientation, and geometry of the light bar on the DMD are shown in Figure 7.3(a). The recovered image is shown in Figure 7.3(b). The location and orientation of the recovered rectangular light bar, highlighted by a red rectangle, are similar to that shown in Figure 7.3(a). The image has a resolution of 50×50 pixels. This image was recovered by only 800 measurements, which is less than 35% of the total pixel numbers (2500).

7.3.1 Dynamic Observation

The imaging system was utilized to observe the dynamic movement of a laser spot. The laser spot was initially located at the lower left of the DMD, as shown in Figure 7.4(a). We designed a trajectory of the laser spot movement: it was first moved downwards, and then moved upwards when the laser approached the bottom edge of the DMD. Six frames of the IR images captured by the imaging system were shown in Figure 7.4. The resolution of these images is 50×50 pixels, and 800 measurements were performed to recover the images using minimization TV-norm reconstruction algorithm. The images clearly show the movement of the laser spot following the designed path: the laser spot moved towards the bottom of the DMD in the first five frames (Figure 7.4(a-e)), and it bounced upwards in the last frame (Figure 7.4(f)).

However, it is difficult to identify the actual size and geometry of the laser spot from these images due to their low resolution. Figure 7.4(b) shows the laser spot covered one pixel, while it covered three pixels in Figure 7.4(c) and Figure 7.4(e), and the rest of frames show the laser spot occupied two pixels. The spot size variation may be caused by the difference of the location of the laser spot: the laser spot covers one pixel if the spot resides at the center of a pixel, while it covers more than one pixel if the laser spot located at the boundary of a few pixels; the difference, however, may possibly stem from the measurement noise. In order to identify the actual size of the laser spot, we can increase the image resolution. However, this approach will reduce the speed of the sensing system due to the increase of sampling and recovery time. In next section, we will introduce the zooming technique to investigate the laser spot by keeping the same image resolution.

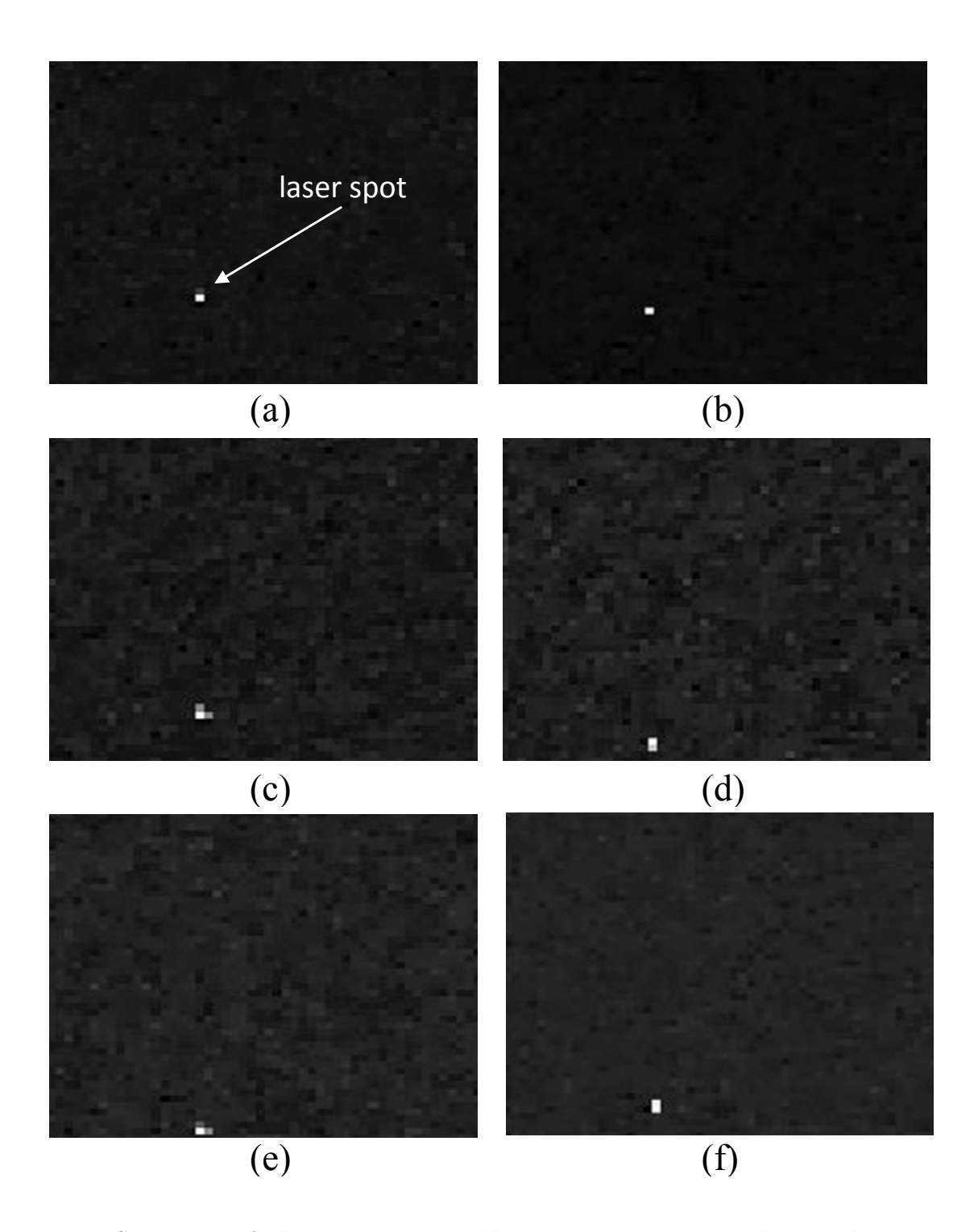


Figure 7.4: Six images of a laser spot captured by our imaging system, showing the movement of the spot.(a) The infrared image shows the initial position of the laser spot. (b)-(e) The laser spot moved downwards towards the bottom of the image. (f) The laser spot moved upwards after it approached the bottom of the DMD.

7.3.2 Zooming

In previous experiments, all 1024×768 micromirrors in the DMD were used to capture the IR images with a resolution of 50×50 pixels. In such a setup, 315 micromirrors in unison represent one pixel, corresponding to an area of 0.045 mm² on the DMD ($144~\mu m^2$ per micromirror). Therefore this setup is difficult to identify the features of an object with similar or smaller size than that area. We developed a zooming technique to investigate the details of small objects without degrading the performance of the system.

The imaging system can perform zooming in and out by varying the number of micromirrors for each pixel. When the imaging system worked in zooming-in mode, only a portion of the DMD was used as the measurement matrix generator. As a result, each pixel included fewer micromirrors. This mode is supported by the DMD because each individual micromirror can be controlled independently.

In order to verify the zooming concept, we designed an experiment to study the geometry and size of the IR laser spot shown in Figure 7.4. In the zooming experiment, each IR image (50×50 pixels) was recovered using the same measurement matrix, number of measurements, and recovery algorithm as previous experiments. The only difference is the number of micromirrors for each pixel.

We first recovered an image (×1 magnification image in Figure 7.5) by using the whole DMD, which shows the laser spot covering two pixels, corresponding to 0.090 mm² in area on the DMD. The intensity of each pixel for images in Figure 7.5 is represented by 8 bits grey-scale: each pixel has a brightness from 0 to 255, where 0 is black and 255 is white. A typical OTSU method [101] is used to convert gray-scale images into binary images in order to identify the actual area of the laser spot. When we used 521×384 micromirrors

(highlighted by the blue rectangle in ×1 magnification image) to generate the measurement matrix, a ×2 magnification image was obtained. It is termed ×2 magnification because the micromirrors only cover half of the length and width of the DMD, while the recovered image had same pixel number as the ×1 magnification image. The ×2 magnification image shows that a laser spot covered six pixels, reducing to 0.068 mm² in area. We further sectioned the measurement matrix into 130×96 micromirrors. The recovered ×8 magnification image shows that the laser spot covered forty one pixels, corresponding to 0.029 mm² in area. A ×12 magnification image was obtained when we used 85×64 micromirrors to generate the measurement matrix. A clear outline of the laser spot was exhibited in elliptical shape, which is similar to the laser spot geometry captured by a CMOS camera. The laser spot area was reduced to 0.028 mm² in the ×12 magnification image. The experimental results showed that the shape and area of the laser spot are progressively refined to its actual geometry by zooming in with our sensing system. It was also observed that images with larger magnification associated with lower image quality, since each pixel contained fewer micromirrors, which reflected less light to the photodetector.

This sensing system is universal and adaptable. It is universal because we can use the same measurement matrix for all experiments [95]. The system is adaptable because the resolution of images and sections of DMD used for zooming can be adaptively adjusted depending on the features of objects.

7.4 Chapter Summary

A novel sensing system using CNT based IR detector as core component was demonstrated.

A compressive sensing algorithm based IR sensing system was developed by generating mea-

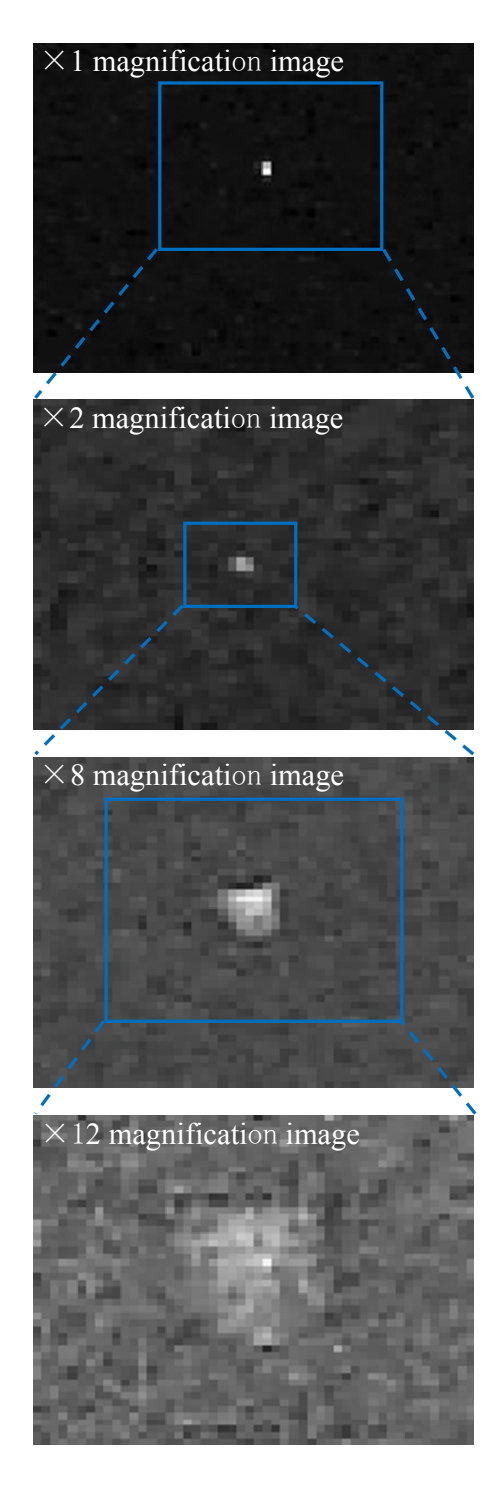


Figure 7.5: $\times 1$, $\times 2$, $\times 8$, $\times 12$ magnification IR images captured by our imaging system, and their corresponding sections of DMD used to capture the images were highlighted by blue rectangles.

surement matrices using DMD, which compressed the original images. The experimental results showed that this imaging system can recover original images by decoding the electrical signals, with measurement times much less than original dimension. This camera architecture provide an novel platform to effectively capture high resolution IR images.

Chapter 8

Conclusions and Future Work

8.1 Conclusion

IR sensing systems have versatile applications, but their performance was limited by the their core component, photodetectors. The low performance of conventional photodetectors stems from the optical and physical properties of bulk semiconductors. With the development of nanotechnology, these problems may be addressed by developing nano-materials based photodetectors. In particular, CNTs have promising optoelectronic and optical properties arose from its perfect 1D hollow-cylinder geometry. In this research, an IR sensing system was built using a CNT based photodetector.

Based on the results and discussion presented in previous chapters, the following conclusion can be made:

• The CNT based Schottky photodiodes have been thoroughly studied for IR detection.

The role of CNT-metal contacts in determining the performance of IR detection was systematically investigated. The performance of CNT photodetectors with different metals, symmetric and asymmetric metal structures, and at different temperatures was studied. This study improved our understanding of the underlying physics of the photo-detection, and photo-response of CNT based Schottky photodiodes was highly enhanced by using asymmetric metal structure.

- The importance of electrostatic doping in determining IR detection of the CNT photodetectors was demonstrated using CNTFET based photodetectors. The built-in potential between metals and a CNT in a CNTFET was responsible for the separation of photo-excited electron and hole pair generation, thus electrostatic doping can control the built-in potential so as to improve photon detection. It was found that asymmetric metal structure and electrostatic doping can reduce dark current, improve photocurrent, and enhance open circuit voltage. In addition, experimental results of a multi-gate CNTFET revealed an unconventional charge distribution in the CNT, which can naturally enlarge the absorption area of CNT photodetectors.
- A 3×3 focal plane array of CNTFET based photodetectors was fabricated. This small focal plane array demonstrated the feasibility of imaging using CNT based photodetectors. Meanwhile, it showed the difficulties of manufacturing megapixel count pixels using nano-materials.
- A breakdown process was developed to engineer the bandgap energy of MWCNT.

 MWCNT based photodetectors were demonstrated to detect MWIR at room temperature by tuning the bandgap energy. Comparing with the spectral responses of SWCNT based photodetectors, MWCNT based photodetectors exhibited wide spectral responses due to the stacking of layers with different bandgap energies.
- A bowtie antenna was developed to improve the fill factor of CNT based photodetectors by confining electromagnetic wave into a sub-wavelength volume. Wavelength of IR is much larger than the size of CNT, resulting in small fill factor. Optical antenna functioned as a plasmonic lens to compress light onto CNT in order to improve photocurrent generation.

- Photonic crystal cavity was fabricate to further improve the fill factor of CNT based photodetectors. Introducing a defect in a photonic crystal with a periodic dielectric/air structure, most of light was trapped into the defect region. By aligning the defect onto the CNT photodetector, a photocurrent enhancement was demonstrated.
- A compressive sensing based sensing system was developed using a single pixel CNT photodetector. In order to fully use the outstanding performance of CNT photodetectors and overcome the difficulties of manufacturing large detector array, an IR sensing system was developed using compressive sensing algorithm. This camera system requires only a single photodetector. Experimental results showed that the number of measurement using this camera system was much less than the size of the original images.

8.2 Future Research

Future research will focus on the following three directions:

- Both the optical antenna and photonic crystal cavity have demonstrated to improve the fill factor of CNT photodetectors, but the design of these devices was not optimized.

 These unconventional light confinement devices are worthy to further develop in order to improve the photo-responses of the detectors.
- Further studies are needed to improve the performance of the sensing system. We have demonstrated the feasibility of using compressive sensing algorithm to construct a sensing system. However, the speed of the system is still low compared to commercial IR cameras.

• This sensing system architecture can be applied to other types of photodetectors.

A CNT photodetector is just one example of nano-material based photodetectors.

Graphene, nanowires, quantum dots, and quantum wells are also promising optoelectronic materials. This imaging system may accelerate the development of IR cameras that utilize other high performance nano-photodetectors.

BIBLIOGRAPHY

BIBLIOGRAPHY

- [1] Antoni Rogalski. Infrared detectors: an overview. Infrared Physics and Technology, 43(3-5):187-210, 2002.
- [2] R. Agarwal and C.M. Lieber. Semiconductor nanowires: optics and optoelectronics. *Applied Physics A: Materials Science and Processing*, 85:209–215, 2006.
- [3] Zhiyong Fan, Rehan Kapadia, Paul W. Leu, Xiaobo Zhang, Yu-Lun Chueh, Kuniharu Takei, Kyoungsik Yu, Arash Jamshidi, Asghar A. Rathore, Daniel J. Ruebusch, Ming Wu, and Ali Javey. Ordered arrays of dual-diameter nanopillars for maximized optical absorption. *Nano Letters*, 10(10):3823–3827, 2010.
- [4] L. E. Brus. Electron-electron and electron-hole interactions in small semiconductor crystallites: The size dependence of the lowest excited electronic state. *The Journal of Chemical Physics*, 80(9):4403–4409, 1984.
- [5] R and Reisfeld. Nanosized semiconductor particles in glasses prepared by the solcgel method: their optical properties and potential uses. *Journal of Alloys and Compounds*, 341(1-2):56 61, 2002.
- [6] J. W. Mintmire, B. I. Dunlap, and C. T. White. Are fullerene tubules metallic? *Phys. Rev. Lett.*, 68:631 634, 1992.
- [7] M. S. Dresselhaus, G. Dresselhaus, and Riichiro Saito. Carbon fibers based on c60 and their symmetry. *Phys. Rev. B*, 45:6234 6242, 1992.
- [8] M. Dresselhaus, G. Dresselhaus, and Phaedon Avouris (Eds.). Carbon Nanotubes: Synthesis, Structure, Properties and Application. Springer, Berlin, 2001.
- [9] Phaedon Avouris. Carbon nanotube electronics. Chemical Physics, 281:429C445, 202.
- [10] King Wai Chiu Lai, Ning Xi, Carmen Kar Man Fung, Hongzhi Chen, and Tzyh-Jong Tarn. Engineering the band gap of carbon nanotube for infrared sensors. *Applied Physics Letters*, 95(22):221107, 2009.

- [11] M. Wolf, R. Brendel, J. H. Werner, and H. J. Queisser. Solar cell efficiency and carrier multiplication in si[sub 1 x]ge[sub x] alloys. *Journal of Applied Physics*, 83(8):4213–4221, 1998.
- [12] Nathaniel M. Gabor, Zhaohui Zhong, Ken Bosnick, Jiwoong Park, and Paul L. McEuen. Extremely Efficient Multiple Electron-Hole Pair Generation in Carbon Nanotube Photodiodes. *Science*, 325(5946):1367–1371, 2009.
- [13] Ali Javey, Jing Guo, Qian Wang, Mark Lundstrom, and Hongjie Dai. Ballistic carbon nanotube field-effect transistors. *Nature*, 424:654–657, 2003.
- [14] Brendan M. Kayes, Harry A. Atwater, and Nathan S. Lewis. Comparison of the device physics principles of planar and radial p-n junction nanorod solar cells. *Journal of Applied Physics*, 97(11):114302, 2005.
- [15] Fran çois Léonard and J. Tersoff. Novel length scales in nanotube devices. *Phys. Rev. Lett.*, 83(24):5174–5177, 1999.
- [16] I. A. Levitsky and W. B. Euler. Photoconductivity of single-wall carbon nanotubes under continuous-wave near-infrared illumination. *Appl. Phys. Lett.*, 83:1857–1859, 2003.
- [17] Basudev Pradhan, Kristina Setyowati, Haiying Liu, David H. Waldeck, and Jian Chen. Carbon nanotube?polymer nanocomposite infrared sensor. *Nano Letters*, 8(4):1142–1146, 2008.
- [18] William B. Euler Pang-Leen Ong and Igor A. Levitsky. Carbon nanotube-si diode as a detector of mid-infrared illumination. *Applied Physics Letters*, 96(3):033106, 2010.
- [19] Marian B. Tzolov, Teng-Fang Kuo, Daniel A. Straus, Aijun Yin, and Xu. Carbon nanotube?silicon heterojunction arrays and infrared photocurrent responses. *The Journal of Physical Chemistry C*, 111(15):5800–5804, 2007.
- [20] Ji Ung Lee. Photovoltaic effect in ideal carbon nanotube diodes. *Appl. Phys. Lett.*, 87:073101, 2005.
- [21] R. Martel, T. Schmidt, H. R. Shea, T. Hertel, and Ph. Avouris. Single- and multi-wall carbon nanotube field-effect transistors. *Applied Physics Letters*, 73(17):2447–2449, 1998.
- [22] S. Heinze, J. Tersoff, R. Martel, V. Derycke, J. Appenzeller, and Ph. Avouris. Carbon nanotubes as schottky barrier transistors. *Phys. Rev. Lett.*, 89(10):106801, 2002.

- [23] Jiangbo Zhang, Ning Xi, Hongzhi Chen, King W. C. Lai, Guangyong Li, and Uchechukwu Wejinya. Photovoltaic effect in single carbon nanotube-based schottky diodes. *International Journal of Nanoparticles*, 1(2):108–118, 2008.
- [24] Philip G. Collins, Michael S. Arnold, and Phaedon Avouris. Engineering Carbon Nanotubes and Nanotube Circuits Using Electrical Breakdown. Science, 292(5517):706–709, 2001.
- [25] Jijun Zhao, Jie Han, and Jian Ping Lu. Work functions of pristine and alkali-metal intercalated carbon nanotubes and bundles. *Phys. Rev. B*, 65(19):193401, 2002.
- [26] XD Cui, M Freitag, R Martel, L Brus, and P Avouris. Controlling energy-level alignments at carbon nanotube/Au contacts. *Nano Letters*, 3(6):783–787, 2003.
- [27] King W. C. Lai, Ning Xi, and Uchechukwu C. Wejinya. Automated process for selection of carbon nanotube by electronic property using dielectrophoretic manipulation. *Journal of Micro - Nano Mechatronics*, 4(1-2):37–48, 2008.
- [28] G. Y. Li, N. Xi, and M. Yu. Development of augmented reality system for afm based nanomanipulation. *IEEE/ASME Trans. on Mechatronics*, 9:358–365, 2004.
- [29] J. Zhang, N. Xi, G. Li, H. Y. Chan, and U. C. Weijinya. Adaptable end effector for atomic force microscopy based nanomanipulation. *IEEE Trans. on Nanotechnology*, 5:628–642, 2006.
- [30] Jiangbo Zhang, Ning Xi, Lianqing Liu, Hongzhi Chen, King Lai, and Guangyong Li. Atomic force yields a master nanomanipulator. *Nanotechnology Magazine*, *IEEE*, 2(2):13 –17, june 2008.
- [31] Jiangbo Zhang, Ning Xi, Hongzhi Chen, King Lai, Guangyong Li, and U.C. Wejinya. Design, manufacturing, and testing of single-carbon-nanotube-based infrared sensors. *Nanotechnology, IEEE Transactions on*, 8(2):245–251, 2009.
- [32] King Wai Chui Lai, Ning Xi, Carmen Kar Man Fung, Jiangbo Zhang, Hongzhi Chen, Yilun Luo, and Uchechukwu C. Wejinya. Automated Nanomanufacturing System to Assemble Carbon Nanotube Based Devices. *International Journal of Robotics Research*, 28(4):523–536, 2009.
- [33] J. Appenzeller, M. Radosavljević, J. Knoch, and Ph. Avouris. Tunneling versus thermionic emission in one-dimensional semiconductors. *Phys. Rev. Lett.*, 92(4):048301, Jan 2004.

- [34] J. Zhang, N. Xi, H. Chan, and G. Li. Single carbon nanotube based infrared sensor. Electro-Optical and Infrared Systems: Technology and Applications III, SPIE Proc., 6395:63950A, 2006.
- [35] M. H. Yang, K. B. K. Teo, and W. I. Milne. Carbon nanotube schottky diode and directionally dependent field-effect transistor using asymmetrical contacts. *Appl. Phys. Lett.*, 87:253116, 2005.
- [36] Hongjie Dai. Carbon nanotubes: Synthesis, integration, and properties. Accounts of Chemical Research, 35:1035–1044, 2002.
- [37] SJ Tans, ARM Verschueren, and C Dekker. Room-temperature transistor based on a single carbon nanotube. *NATURE*, 393(6680):49–52, 1998.
- [38] MS Fuhrer, J Nygard, L Shih, M Forero, YG Yoon, MSC Mazzoni, HJ Choi, J Ihm, SG Louie, A Zettl, and PL McEuen. Crossed nanotube junctions. *SCIENCE*, 288(5465):494–497, 2000.
- [39] S. J. Wind, J. Appenzeller, R. Martel, V. Derycke, and Ph. Avouris. Vertical scaling of carbon nanotube field-effect transistors using top gate electrodes. *Applied Physics Letters*, 80:3817 3819, 2002.
- [40] A. Javey, J. Guo, D.B. Farmer, Q. Wang, D. Wang, R.G. Gordon, M. Lundstrom, and H. Dai. Carbon nanotube field-effect transistors with integrated ohmic contacts and high-k gate dielectrics. *Nano Letters*, 4(3):447–450, 2004.
- [41] M. Freitag, Y. Martin, J. A. Misewich, R. Martel, and Ph. Avouris. Photoconductivity of single carbon nanotubes. *Nano Letters*, 3:1067–1071, 2003.
- [42] Xiaohui Qiu, Marcus Freitag, Vasili Perebeinos, and Phaedon Avouris. Photoconductivity spectra of single-carbon nanotubes: Implications on the nature of their excited states. *Nano Letters*, 5:749–752, 2005.
- [43] Masashi Shiraishi and Masafumi Ata. Work function of carbon nanotubes. *Carbon*, 39(12):1913 1917, 2001.
- [44] J. Appenzeller, M. Radosavljević, J. Knoch, and Ph. Avouris. Tunneling versus thermionic emission in one-dimensional semiconductors. *Phys. Rev. Lett.*, 92(4):048301, 2004.

- [45] Donghun Kang, Noejung Park, Ju hye Ko, Eunju Bae, and Wanjun Park. Oxygeninduced p-type doping of a long individual single-walled carbon nanotube. *Nanotechnology*, 16(8):1048–1052, 2005.
- [46] Changxin Chen, Wei Zhang, Eric Siu-Wai Kong, and Yafei Zhang. Carbon nanotube photovoltaic device with asymmetrical contacts. *Applied Physics Letters*, 94(26):263501, 2009.
- [47] Fran çois Léonard and J. Tersoff. Role of fermi-level pinning in nanotube schottky diodes. *Phys. Rev. Lett.*, 84(20):4693–4696, 2000.
- [48] M Chelvayohan and C H B Mee. Work function measurements on (110), (100) and (111) surfaces of silver. *Journal of Physics C: Solid State Physics*, 15(10):2305–2312, 1982.
- [49] Woong Kim, Ali Javey, Ophir Vermesh, Qian Wang, Yiming Li, and Hongjie Dai. Hysteresis caused by water molecules in carbon nanotube field-effect transistors. *Nano Lett.*, 3:193–198, 2003.
- [50] A. Phaedon. Carbon nanotube electronics. Chem. Phys., 281:429–445, 2002.
- [51] H. Kataura, Y. Kamazava, Y. Maniwa, I. Umezu, S. Suzuki, Y. Ohtsuka, and Y. Achiba. Optical properties of single-wall carbon nanotubes. *Synth. Met.*, 103:2555–2558, 1999.
- [52] Stephen W. Kennerly Samuel C. H. Wang Mani Sundaram Parvez N. Uppal Michael L. Winn Gregory L. Milne Arnold C. Goldberg, Theodore Fischer and Mark A. Stevens. Dual-band qwip mwir/lwir focal plane array test results. In *Proc. SPIE*, volume 4028, page 276, 2000.
- [53] J. Caufleld. Simultaneous integrating staring two color irfpa. In *Proc. the 1997 IRIS-Detector Specialty Group Meeting on Detectors*, page 351, 1998.
- [54] M. Sundaram. Advances in qwip fpa (2-color and 1-color) technology. In *Proc. the* 1998 IRIS Specialty Group Meeting on Detectors, page 219, 1999.
- [55] P. Warren M. Satyshur M. Kruer D. Scribner, J. Schuler. Dual-band qwip mwir/lwir focal plane array test results. In *Proc. SPIE*, volume 3379, page 2, 1998.
- [56] E.R. Fossum. Cmos image sensors: electronic camera-on-a-chip. *Electron Devices*, *IEEE Transactions on*, 44(10):1689 –1698, oct 1997.

- [57] W. A. Murray and W. L. Barnes. Plasmonic materials. *Advanced Materials*, 19(22):3771–3782, 2007.
- [58] Jon. A. Schuller, Edward S. Barnard, Wenshan Cai, Young Chul Jun, Justin S. White, and Mark L. Brongersma. Plasmonics for extreme light concentration and manipulation (vol 9, pg 193, 2010). *NATURE MATERIALS*, 9(4), 2010.
- [59] Palash Bharadwaj, Bradley Deutsch, and Lukas Novotny. Optical antennas. *Adv. Opt. Photon.*, 1(3):438–483, Nov 2009.
- [60] Harry A. Atwater and Albert Polman. Plasmonics for improved photovoltaic devices. *Nature Materials*, 9(10):865, 2010.
- [61] Zhiyong Fan, Daniel Ruebusch, Asghar Rathore, Rehan Kapadia, Onur Ergen, Paul Leu, and Ali Javey. Challenges and prospects of nanopillar-based solar cells. *Nano Research*, 2:829–843, 2009.
- [62] D. M. Schaadt, B. Feng, and E. T. Yu. Enhanced semiconductor optical absorption via surface plasmon excitation in metal nanoparticles. *Applied Physics Letters*, 86(6):063106, 2005.
- [63] Zongfu Yu, Georgios Veronis, Shanhui Fan, and Mark L. Brongersma. Design of midinfrared photodetectors enhanced by surface plasmons on grating structures. *Applied Physics Letters*, 89(15):151116, 2006.
- [64] Mark W. Knight, Heidar Sobhani, Peter Nordlander, and Naomi J. Halas. Photodetection with Active Optical Antennas. *SCIENCE*, 332(6030):702–704, MAY 6 2011.
- [65] Hongzhi Chen, Ning Xi, K.W.C. Lai, C.K.M. Fung, and Ruiguo Yang. Development of infrared detectors using single carbon-nanotube-based field-effect transistors. *Nanotechnology*, *IEEE Transactions on*, 9(5):582–589, 2010.
- [66] P. J. Schuck, D. P. Fromm, A. Sundaramurthy, G. S. Kino, and W. E. Moerner. Improving the mismatch between light and nanoscale objects with gold bowtie nanoantennas. *Phys. Rev. Lett.*, 94:017402, Jan 2005.
- [67] DP Fromm, A Sundaramurthy, PJ Schuck, G Kino, and WE Moerner. Gap-dependent optical coupling of single Bowtie nanoantennas resonant in the visible. *Nano Letters*, 4(5):957–961, 2004.

- [68] Carmen Kar Man Fung, Ning Xi, Balasubramaniam Shanker, and King Wai Chiu Lai. Nanoresonant signal boosters for carbon nanotube based infrared detectors. *Nanotechnology*, 20(18), 2009.
- [69] A Sundaramurthy, KB Crozier, GS Kino, DP Fromm, PJ Schuck, and WE Moerner. Field enhancement and gap-dependent resonance in a system of two opposing tip-to-tip Au nanotriangles. *Physical Review B*, 72(16), OCT 2005.
- [70] KB Crozier, A Sundaramurthy, GS Kino, and CF Quate. Optical antennas: Resonators for local field enhancement. *Journal of Applied Physics*, 94(12):7950, 2003.
- [71] E Betzig, JK Trautman, TD Harris, JS Weiner, and RL Kostelak. Breaking the diffraction barrier- optical microscopy on a nanometric scale. *Science*, 251(5000):1468– 1470, MAR 22 1991.
- [72] Ragip A. Pala, Justin White, Edward Barnard, John Liu, and Mark L. Brongersma. Design of Plasmonic Thin-Film Solar Cells with Broadband Absorption Enhancements. ADVANCED MATERIALS, 21(34):3504+, SEP 11 2009.
- [73] Wei Ding, Renaud Bachelot, Sergei Kostcheev, Pascal Royer, and Roch Espiau de Lamaestre. Surface plasmon resonances in silver bowtie nanoantennas with varied bow angles. 108(12):124314, 2010.
- [74] Kevin L. Shuford, Mark A. Ratner, and George C. Schatz. Multipolar excitation in triangular nanoprisms. 123(11):114713, 2005.
- [75] Tomoyuki Yoshie, Jelena Vuckovic, Axel Scherer, Hao Chen, and Dennis Deppe. High quality two-dimensional photonic crystal slab cavities. *Applied Physics Letters*, 79(26):4289–4291, 2001.
- [76] Toshihiko Baba, Daisuke Sano, Kengo Nozaki, Kyoji Inoshita, Yusuke Kuroki, and Fumio Koyama. Observation of fast spontaneous emission decay in gainasp photonic crystal point defect nanocavity at room temperature. *Applied Physics Letters*, 85(18):3989–3991, 2004.
- [77] M. Notomi, K. Yamada, A. Shinya, J. Takahashi, C. Takahashi, and I. Yokohama. Extremely large group-velocity dispersion of line-defect waveguides in photonic crystal slabs. *Phys. Rev. Lett.*, 87(25):253902, 2001.
- [78] Yoshihiro Akahane, Takashi Asano, Bong-Shik Song, and Susumu Noda. High-q photonic nanocavity in a two-dimensional photonic crystal. *Nature*, 425(6961):944–947, 2003.

- [79] Mehmet Bayindir and E. Ozbay. Heavy photons at coupled-cavity waveguide band edges in a three-dimensional photonic crystal. *Phys. Rev. B*, 62(4):R2247–R2250, 2000.
- [80] M Jerman, ZH Qiao, and D Mergel. Refractive index of thin films of SiO2, ZrO2, and HfO2 as a function of the films' mass density. *APPLIED OPTICS*, 44(15):3006–3012, 2005.
- [81] H. W. Hubers, J. Schubert, A. Krabbe, M. Birk, G. Wagner, A. Semenov, and G. Goltsman. Parylene anti-reflection coating of a quasi-optical hot-electron-bolometric mixer at terahertz frequencies. *Infrared Physics and Technology*, 42(1):41 47, 2001.
- [82] J. Haupt and R. Nowak. Compressive sampling vs. conventional imaging. In *Image Processing*, 2006 IEEE International Conference on, pages 1269 –1272, oct. 2006.
- [83] M. F. Duarte, M. A. Davenport, D. Takhar, J. N. Laska, T. Sun, K. F. Kelly, and R. G. Baraniuk. Single-pixel imaging via compressive sampling. *IEEE Signal Processing Magazine*, 25(2):83–91, 2008.
- [84] Hongzhi Chen, Ning Xi, Bo Song, LiangLiang Chen, and K.W.C. Lai. Single pixel infrared camera using a carbon nanotube photodetector. In *Sensors*, 2011 IEEE, pages 1362 –1366, oct. 2011.
- [85] M. A. Davenport, M. F. Duarte, Y.C. Eldar, and G. Kutyniok. *Introduction to Compressed Sensing*, chapter One. Cambridge University Press, 2012.
- [86] Michael Lustig, David Donoho, and John M. Pauly. Sparse mri: The application of compressed sensing for rapid mr imaging. *Magnetic Resonance in Medicine*, 58(6), 2007.
- [87] Jianguo Zhao, Bo Song, Ning Xi, King Wai Chiu Lai, Hongzhi Chen, and Chengeng Qu. Compressive feedback based non-vector space control. In *American Control Conference* (ACC), 2012, pages 4090 –4095, june 2012.
- [88] Bo Song, Jianguo Zhao, Ning Xi, King Wai Chiu Lai, Ruiguo Yang, Hongzhi Chen, and Chengeng Qu. Non-vector space control for nanomanipulations based on compressive feedbacks. In *Robotics and Automation (ICRA)*, 2012 IEEE International Conference on, pages 2767 –2772, may 2012.
- [89] Tim T. Y. Lin and Felix J. Herrmann. Compressed wavefield extrapolation. *Geophysics*, 72(5):SM77–SM93, 2007.

- [90] S.F. Cotter and B.D. Rao. Sparse channel estimation via matching pursuit with application to equalization. *Communications, IEEE Transactions on*, 50(3):374 –377, mar 2002.
- [91] E. Candès and M. Wakin. An introduction to compressive sampling. *IEEE Signal Processing Magazine*, 25(2):21–30, 2008.
- [92] David L. Donoho and Michael Elad. Optimally sparse representation in general (nonorthogonal) dictionaries via l_1 minimization. Proceedings of the National Academy of Sciences, 100(5):2197–2202, 2003.
- [93] Albert Cohen, Wolfgang Dahmen, and Ronald Devore. Compressed sensing and best k-term approximation. *Journal of the American Mathematical Society*, 22(1):211–231, 2009.
- [94] E. Candès. The restricted isometry property and its implications for compressed sensing. Comptes Rendus Mathematique, 346(9-10):589–592, 2008.
- [95] E. J. Candes and T. Tao. Near optimal signal recovery from random projections: universal encoding strategies? *IEEE Transactions on Information Theory*, 52(12):5406–5425, 2006.
- [96] E.J. Candes and T. Tao. Decoding by linear programming. *IEEE Transactions on Information Theory*, 51(12):4203–4215, 2005.
- [97] Richard Baraniuk, Mark Davenport, Ronald Devore, and Michael Wakin. A simple proof of the restricted isometry property for random matrices. *Constructive Approximation*, 28(3):253–263, 2008.
- [98] Joel A. Tropp and Stephen J. Wright. Computational methods for sparse solution of linear inverse problems. *Proceedings of the IEEE*, 98(6):948–958, 2010.
- [99] Liangliang Chen, Ning Xi, Hongzhi Chen, and K.W.C. Lai. Development of readout system for carbon nanotube based infrared detector. In *Nanotechnology Materials and Devices Conference (NMDC)*, 2010 IEEE, pages 230–234, 2010.
- [100] Liangliang Chen, Ning Xi, Hongzhi Chen, and King Wai Chiu Lai. High gain current readout method for mwcnt infrared sensor. In *Nanotechnology (IEEE-NANO)*, 2012 12th IEEE Conference on, pages 1–4, 2012.
- [101] Nobuyuki Otsu. A threshold selection method from gray-level histograms. Systems, Man and Cybernetics, IEEE Transactions on, 9(1):62 –66, jan. 1979.